A Monte Carlo simulation framework for performance evaluation of a proton imaging system without front trackers

Jarle Rambo Sølie

Thesis for the degree of Philosophiae Doctor (PhD)
University of Bergen, Norway
2020

UNIVERSITY OF BERGEN

A Monte Carlo simulation framework for performance evaluation of a proton imaging system without front trackers

Jarle Rambo Sølie

Thesis for the degree of Philosophiae Doctor (PhD)
at the University of Bergen

Date of defense: 18.12.2020

© Copyright Jarle Rambo Sølie

The material in this publication is covered by the provisions of the Copyright Act.

Year: 2020

Title: A Monte Carlo simulation framework for performance evaluation of a proton imaging system without front trackers

Name: Jarle Rambo Sølie

Print: Skipnes Kommunikasjon / University of Bergen

Acknowledgements

As I am reflecting on my time as a doctoral student for the past four years, I recognize that I have been extremely privileged to have been working with so many talented individuals, and for getting to be a part of the forefront of proton imaging in the reigns of the Bergen proton CT collaboration. It has been exceptionally stimulating and educational to dive into the underlying physics principles, development of a prototype detector design, and image reconstruction in proton imaging. Particularly because proton imaging offers a myriad of unsolved challenges and obstacles concerning the underlying physics of charged particles and the potential clinical implementation of proton imaging. It has also been an absolute pleasure getting to travel more than halfway around the world in both westward and eastward direction to complete my student course work and present my work at conferences abroad.

I have been fortunate to have had multiple supervisors that I could turn to for guidance when questions and dilemmas arose during my doctoral thesis work, and I would not have been able to undertake or produce so much if not for their help and advice. Especially Ilker Meric as my main supervisor for always having an open door to discuss matters both big and small concerning every aspect of my thesis and guiding me through the entire PhD-student program. Two co-supervisors from my Master thesis also followed me into this PhD program, Odd Harald Odland, who introduced and recommend me this project, without him I might never have had the pleasure of working towards a doctorate degree in the first place. Dieter Röhrich, for sharing his formidable experience and insight into scientific work, and his scientific connections abroad also served me tremendously well by giving me the chance to spend ten weeks at the German Cancer Research Center (DKFZ) in Heidelberg to work with some of the most talented people I have ever had the pleasure of working with.

I want to show enormous gratitude towards the DKFZ group who welcomed me with open arms and gave me the most scientifically stimulating and productive ten weeks I have ever experienced. Especially Lennart Volz, whose patience, incredible understanding and sharp intellect taught me more about scattering, path estimation, and image reconstruction than I could ever have hoped for, and whom single-handily expanded my

initial thesis goals to include said topics. His continued connection and co-operation beyond my research stay also proved to be extremely valuable and productive, were we not both PhD-candidates one could easily consider him my third co-supervisor. His friendship is also something I will treasure and I hope to bump into him at many professional gatherings and conferences in the future.

The Bergen proton CT collaboration consists of several talented people involved in many different research disciplines. I would like to thank Ola Grøttvik for discussing and answering many of my questions concerning the prototype detector and its properties, Pierluigi Piersimoni for helping out with the proton CT reconstructions, and Helge E.S. Pettersen whose scientific groundwork, insight, and support helped me get started in my first year and stayed a valuable discussion partner and friend all throughout my four years. Not to mention my other fellow PhD students over the years, Tordis, Lars Fredrik, Eivind, Viljar, Lucas, Håkon and Fatemeh. I would also like to acknowledge the financial support from the Trond Mohn Foundation (Grant no. TMS2015PAR03).

The emotional support from my family and friends has been a great source of comfort and motivation during the last four years. My parents and two younger brothers brought me stories from my hometown to keep me up to date on life back home. My best friend Truls for providing much fun and games the times I was home on vacations. Alina, Silja, and Ingrid for their company, conversations and friendship that kept me sane and grounded these past four years. Nil, without her, the covid-19 lockdown in the last six months of my thesis writing would have been so much harder and emotionally exhausting.

I am looking forward to meeting you all again at various times and settings in the future. I am forever grateful to all of you.

Jarle Rambo Sølie
Bergen, September 2020

Scientific environment

The work done in this thesis was performed at the Department of Computer Science, Electrical Engineering and Mathematical Sciences at the Western Norway University of Applied Science, and at the Department of Physics and Technology at the University of Bergen. There has also been a close collaboration with physicists at the Division Biomedical Physics in Radiation Oncology at the German Cancer Research Center (DKFZ), Heidelberg, Germany.

Ten weeks in the period 07.05.2018 to 15.07.2018 were spent at DKFZ in Heidelberg, Germany as a visiting researcher working closely with researchers and experts in the Biomedical Physics in Radiation Oncology division focusing on particle therapy and particle imaging applying protons and helium.

The studies and work found in this thesis is a part of the Bergen Proton Computed Tomography (Bergen pCT) collaboration and is motivated in part by the planned proton therapy facility at Haukeland University Hospital (HUH) expected to be operational in 2024.

Abstract

Today, radiotherapy is one of the main methods for cancer treatment and it is used to irradiate a tumour with a prescribed dose according to a dose plan designed to irradiate the tumour cells while sparing surrounding healthy tissue and organs at risk as much as possible. As radiotherapy has improved and increased the survival rates for several types of cancer over the years, a reduction of long and short term side-effects has become an important focus in modern radiotherapy. One of the most severe side-effect is secondary cancer that can occur decades after treatment.

Particle therapy has a potential to reduce the risk of long and short term side-effects in radiotherapy by reducing the irradiated volume and enable more sparing of healthy tissue surrounding the tumor. This can be achieved due to the physics of charged particles stopping in matter and depositing an increased dose at the end of their range. To ensure accurate treatment with particles it is imperative to have the particles stop inside the tumour volume. Today, particle therapy dose plans are based on X-ray computed tomography (CT) images of the patient that are converted to Relative Stopping Power (RSP) to calculate how the particle will deposit dose inside the patient. This conversion, due to the calibration and difference between photon and charged particle interactions in matter, is associated with uncertainties, up to 3.5% in some cases, this can result in misplacement of the distal dose of several mm and necessitate the inclusion of treatment margins around the tumour volume.

Proton CT is an imaging method circumventing this conversion step by applying protons as the imaging particle and directly calculate the RSP for dose planning purposes, proton CT can potentially make treatment with particle therapy even more accurate. Proton CT uses a high energy proton beam with sufficient initial energy to pass through the patient and enter a detector that measures the proton residual energy. The energy-loss of each proton is thus used to reconstruct a volumetric stopping power map over the patient to be used for dose planning. Due to the physics of charged particle interactions, protons will scatter in matter and this necessitates path estimations, i.e. most likely path, of the individual protons as they traverse the patient to achieve more accurate distribution of the energy-loss locations. This typically requires two sets of position

sensitive detector systems (tracker planes), one upstream (front) and one downstream (rear) of the patient to measure the proton entrance and exit position for Most Likely Path (MLP) estimations.

Since proton imaging does not exist in the clinics today, an idea to adapt a proton CT detector assembly to use in proton therapy treatment rooms and bringing proton imaging a step closer to a clinical implementation is to remove the front trackers and instead rely on pencil beam scanning and rear trackers (single-sided imaging setup) for path estimations. A GEANT4/GATE based Monte Carlo (MC) simulation environment was designed to create the necessary MC framework for investigating proton imaging setups both with and without front trackers. The MC calculated proton positions on position sensitive tracker planes is used to reconstruct proton radiographs and proton CT images. The MC simulation environment is based on pencil beam scanning irradiating standardized Catphan® phantoms for spatial resolution and RSP accuracy investigations, including a clinically relevant paediatric head phantom. The pencil beam spot-size and spot-spacing parameters were varied in the single-sided setup to identify and study their effect on MLP and image quality, while a conventional proton imaging setup consisting of both front and rear trackers (double-sided) was used as a gold standard in comparisons. The reconstructed proton radiography and proton CT image quality in terms of spatial resolution and RSP accuracy was quantified to evaluate the proton imaging setups being investigated. The impact on most likely path estimations and image quality in radiographs were also investigated when modifying the pencil beam spot size, e.g. 7 mm and 3 mm full width at half maximum (FWHM), and spot-spacing (spot spacing of 0.5, 1, and 2 times the FWHM) when performing pencil beam scanning.

The practical use of the MC simulation framework was exemplified by modelling the proton CT Digital Tracking Calorimeter (DTC) prototype that is designed and under construction by the Bergen proton CT collaboration. The DTC is a single-sided imaging setup consisting of multiple layers of ALPIDE pixels sensors and aluminium energy absorbers and was modelled in the MC simulation framework with accurate material budgets. The DTC was investigated in terms of the resulting MLP accuracy and image quality using the expected tracker position resolution and RSP resolution of the DTC.

Simulations of the radiation environment using the FLUKA MC code was performed to investigate the radiation environment the detector assembly is expected to be exposed

to during irradiation of the patient. Potential radiation damage and effects such as single event upsets in the radiation sensitive FPGA readout electronics of the DTC were estimated based on FLUKA calculated particle fluence and dose deposited in the FPGAs. When the sensitive FPGAs were placed at a distance of 100 cm or more perpendicular from the DTC it was found to be radiation hard enough to be operational for over 30 years without considerable radiation effects during operation. The ALPIDE in terms of its documented design limitations were also found to be radiation hard enough to survive in the radiation environment for over 30 years.

Image quality analysis in the form of spatial resolution and RSP accuracy revealed that the single-sided proton imaging setup, such as the Bergen DTC, has the potential to be used for dose planning purposes. The spatial resolution results larger than 3 line pairs per cm from the Catphan® CTP528 phantom module, and the less than 0.5% RSP deviation from reference RSP values of materials involved in the Catphan® CTP404 phantom module showed this. However, investigation into the proton CT reconstructed image of a paediatric head phantom revealed that more studies focused on dose plans based on proton CT images should be performed in the future to better evaluate the impact of using a single-sided proton imaging setup.

The MC simulation framework for proton imaging and image analysis is expected to be usable in future proton imaging studies by modifying the proton imaging setups and evaluating resulting proton radiographs and proton CT image qualities.

Contents

1. Introduction

1.1 Proton therapy

Continuous developments in modern medicine, accelerator technology, and beam delivery systems, combined with understanding of how energetic particles interact with matter, have made radiation therapy with charged particles a viable cancer treatment modality. Compared to conventional radiation therapy with photons, charged particle therapy offers improved tumour control, less irradiated healthy tissue and thus lower probability of side effects. This is made possible due to the narrow peak in dose deposition that occur just prior to the stopping position of the charged particles in matter, i.e. at the end of their range, forming a depth-dose characteristic known as the Bragg-peak. This characteristic Bragg-peak phenomena makes it possible to deliver a dose to a Target Volume (TV) with relatively high precision while sparing healthy tissue in the vicinity of the TV, especially beyond the distal edge of the Bragg peak dose distribution in the treatment beam direction.

By the end of year 2019 over 200 000 patients had been treated using charged particle therapy worldwide [1] and in May 2020 there were 104 particle therapy facilities in clinical operation around the world, with another 39 under construction, and several more in planning [2]. The ongoing development and worldwide expansion of charged particle treatment is motivated by its advantages over conventional photon therapy, advantages that include:

(i) **Lower dose to healthy tissue**, effectively reducing unwanted side-effects in both the short term (in treatment and immediate recovery) and long term (in decades post-treatment), offering an expected improvement of the patients mortality and quality of life in the years after completed treatment [3, 4].

(ii) **Improved tumor control**, via increased dose deposition inside the Bragg-peak to be positioned inside the tumour volume. Protons (and especially heavier particles such as helium and carbon) have an enhanced biological effect compared to photons, effectively doing more damage to the tumour inside the TV for a given

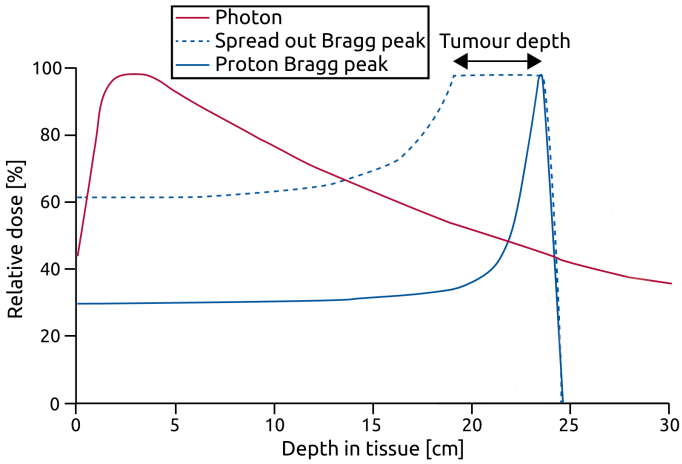

Figure 1.1: The Bragg-peak allows for focusing the dose to a tumor volume and prevent exit dose. Figure re-drawn from Leeman et al. [4].

physical dose [5].

(iii) **Precise dose delivery**, radiation delivery systems in particle therapy will normally mean the application of pencil beam scanning where scanning magnets steer the particle beam in the directions orthogonal to the beam direction, and magnetic fields focus and control individual pencil beams allowing for swift irradiation of the TV slice by slice at respective energy-depths and through lateral raster scanning over the intended TV [6]. Often suited to complex tumour anatomies and yielding more precise dose delivery compared to photon therapy.

The overall advantage of proton therapy over photon therapy is depicted in Figure 1.1 showing the relative depth dose curves for photon and proton beams, illustrating the reduced dose and accuracy of proton therapy compared to photon therapy. Albeit, this figure does not represent an accurate description of photon therapy as the dose is not typically delivered via a single field. Nonetheless, it is this photon attenuation effect and the resulting low dose region distal to the TV that is the cause of dose-baths in healthy tissue outside the TV during photon therapy.

The potential of charged particle therapy lie within the finite range of charged particles and the characteristic Bragg-peak dose distribution, this makes determination of the particle range inside the patient tissue for effective treatment. However, the range

of protons inside a patient is sensitive to variations in material properties that the particle traverses (described in section 1.2). This emphasizes the need for robust dose plans that take the effect of such variations into account and compensate for possible dose distortions, typically done by introducing safety margins around the Gross Tumour Volume (GTV). Such margins can amount to 2.5%–3.5% of the depth of the Bragg Peak to account for range uncertainties, in addition to a fixed 1–3 mm margin accounting for systematic uncertainties in beam delivery system and patient setup [7]. To compute the range of protons in current clinical practices, X-ray Computed Tomography (CT) Hounsfield Units (HU) are converted to the Relative Stopping Power (RSP). RSP is the fundamental tissue characteristic that determines the range of charged particles, and determining the patient RSP via conversion of HU to RSP is associated with uncertainties potentially introducing a range error of up to 3.5% in the worst case [8, 9]. This uncertainty is present due to the fundamental difference between physical interaction processes occurring when photons interact with matter and when charged particles interact with matter.

An ideal way of directly determining the RSP distribution inside a patient, and subsequently reduce uncertainties and treatment margins, is provided by the application of proton imaging; proton radiography (pRad) and proton Computed Tomography (pCT). Proton imaging, where individual protons (their positions and total energy-loss) are detected one-by-one by an imaging detector assembly, has gained increasing interest over the recent years as a promising candidate for improving range prediction accuracy in particle therapy treatment planning [10–12]. The main advantage and goal of proton imaging over conventional X-ray imaging is a more accurate determination of the patient RSP from either pCT [11, 12] or by combining a small number of pRads with a treatment planning X-ray CT [13–15], circumventing the need for X-ray CT obtained HU to RSP conversion [16].

Another alternative to the conventional Single Energy photon CT (SECT) when determining tissue RSP, is Dual Energy CT (DECT) and this imaging modality has been proved to achieve RSP accuracies comparable to obtained with pCT [12, 17]. The patient dose received through DECT is however many times larger than in Proton CT (e.g. 35.7 mGy for DECT and 1.5mGy for pCT of a commercial CTP404 phantom module [12]) and can prove critical in keeping the dose to the patient As Low As Reasonably

Table 1.1: List of some research groups building and having built a prototype proton imaging system, their tracker technologies, position resolution, material budgets, and proton detection rate capabilities.

Prototypes				
Group	Tracker tech.	Pos.Res.[μm]	Mat.Budget[%][1]	Rate
TERA [25]	Triple-GEM	235	0.7	1 MHz
PRIMA [26]	SSD	136	0.43	10 kHz
PRaVDA [20]	SSD	61	0.32	2.5 MHz
LLU/UCSC [27]	SSD	155	0.43	1.2 MHz
Bergen pCT [19]	CMOS MAPS	5	0.45	10 MHz

Achievable (ALARA-principle) when frequent re-planning of the treatment is necessary. Proton CT is also not susceptible to metal artifacts/implants in the same way as SECT/DECT is via beam hardening and photon starvation, and so pCT may become a preferred solution if proved to be clinically viable.

No routinely clinical application of proton CT exists today, but there are several prototypes in the works based on various tracker and detector technologies [18], including one designed and to be built by the Bergen pCT collaboration [19]. Some of these prototype pCT systems along with the tracker technology, position resolution, material budget, and expected detection rates are listed in Table 1.1. Due to their accurate position resolution and potentially high detection rate necessary to keep scan times at reasonable duration, Silicon Strip Detectors (SSD), Gas Electron Multiplier (GEM), and Complementary Metal Oxide Semiconductor(CMOS) Monolithic Active Pixel Sensor (MAPS) are the dominant tracking technologies in proton imaging systems. All existing proton CT prototypes have in general been showing results of RSP with an accuracy better than 1% obtained both in MC simulations and experimental setups [20–23].

1.2 Proton interactions with matter

For charged particles in matter there are various physical processes affecting the properties of the particle (energy, range, and position), this includes ionization (energy-transfer/loss), nuclear interactions, and Multiple Coulomb Scattering (MCS). A brief introduction and description of the processes involved in charged particle interactions

[1] Material budget is given as the material thickness divided by the radiation length of the material (x/X_0), same as defined in [24].

with matter is presented here, a more extensive review can be found in Section 33 of the particle data groups latest review of particle physics [28].

1.2.1 Energy-loss by ionization

The proton energies applied in proton therapy is dictated by the clinical particle range required, i.e. the depth needed to be able to treat a patient, normally this energy range is from 60–70 MeV up to 220–240 MeV and this makes electronic interactions with obstructing electrons and nuclei the dominating process of energy-loss for charged particles. These interactions usually result in a small transfer of energy leading to ionization, atomic or collective excitation. The maximum energy transferable in a single interaction/collision is given as

$$W_{max} = \frac{2m_e c^2 \beta^2 \gamma^2}{1 + 2\gamma m_e/M + (m_e/M)^2} \,. \tag{1.1}$$

Here M is the incoming particle's mass [MeV/c^2], $m_e c^2$ is the electrons mass times the speed of light [MeV], $\beta = v/c$ is the ratio of the particle velocity and speed of light, and $\gamma = 1/\sqrt{1-\beta^2}$.

The mean energy-loss dE/dx of particles in the energy range $0.1 \leq \beta\gamma \leq 1000$ is accurately described by the Bethe equation [28],

$$-\left\langle \frac{dE}{dx} \right\rangle = Kz^2 \frac{Z}{A} \frac{1}{\beta^2} \left[\frac{1}{2} \ln \left(\frac{2m_e c^2 \beta^2 \gamma^2 W_{max}}{I^2} \right) - \beta^2 + \frac{\delta(\beta\gamma)}{2} \frac{C}{Z} \right] . \tag{1.2}$$

Where $K = 4\pi N_A r_e^2 m_e c^2 [\text{MeVmol}^{-1}\text{cm}^2]$ is a constant containing Avogadro's constant N_A, electron radius r_e, electron mass and speed of light, c. In Bethe equation, z denotes the incoming particle charge number, Z and A are the atomic and mass number of the material traversed and I [eV] is its ionization potential. W_{max} [MeV], β, and γ are defined as above. $\delta(\beta\gamma)$ is a correction effect for the density-effect relevant at high energies, and the additional term C/Z account for shell correction from contributions of atomic binding at low energies. For therapeutic energies (i.e. $\beta\gamma \approx 0.7$) the $1/\beta^2$ dependence in Equation 1.2 dominates the energy-loss and leads to an increase in transferred energy as the particle slows down at increasing depths, this leads to a peak in energy transfer towards the end of the particle range, know as the Bragg-peak. This effect can be seen

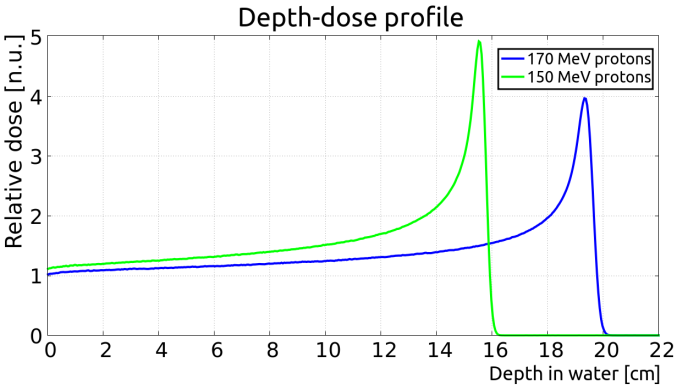

Figure 1.2: Depth-dose profile of 150 MeV and 170 MeV protons depositing energy inside a homogeneous water phantom simulated using the Monte Carlo toolkit, FLUKA [30–32].

in depth-dose profiles of a proton beam, e.g. in Figure 1.2. What can also be seen in this figure is that the broadness of the Bragg-peak (its full width at half maximum) can reach up to a few centimeters. This is due to the stochastic nature of the energy-loss that occur in each interaction, including the number of interactions, giving rise to what is called *energy straggling*. Because of energy straggling, individual particles with identical initial energies will effectively come to a stop at different depths, a beam of particles is therefore never mono-energetic after traversing some matter and results in widening of the Bragg-peak [29].

1.2.2 Proton range

To calculate the range of an incoming particle (position of the distal part of the Bragg-peak), the Continuous Slowing Down Approximation (CSDA) where the particle is assumed to lose its energy at a mean rate, is used. The particle range is thus defined as

$$R = \int_{E_{in}}^{0} \frac{1}{-\langle dE/dx \rangle} dE \,, \tag{1.3}$$

where E_{in} is the initial energy and $-\langle dE/dx \rangle$ is the mean energy-loss as defined in Equation 1.2. The range of the particle is then understood as the depth when the kinetic energy of the particle reaches 0. To accurately compute the range of the particle, the stopping power of the material has to be known. This depends on the accuracy of the material dependent quantities from Equation 1.2 (ρ, I and Z) and these are not easily

measured without considerable uncertainties.

For simpler handling of the stopping power, Hanson et al. [33] tomographically reconstructed the proton energy-loss relative to that in water and this gave rise to the concept of Relative Stopping Power (RSP). RSP is the stopping power of a material divided by the stopping power of water,

$$\mathrm{RSP} = \frac{-\langle \mathrm{dE/dx} \rangle}{-\langle \mathrm{dE/dx} \rangle_{\mathrm{water}}} \,, \tag{1.4}$$

and combines the material dependent quantities of the stopping power into one factor. In proton imaging reconstruction, the measured energy-loss or residual range of protons are converted to an integral of the RSP along the full length of the proton path, L, through the patient, this integral is generally called the Water Equivalent Path Length (WEPL). WEPL is calculated from Equation 1.3 and the stopping power of water [34, 35],

$$\mathrm{WEPL} := \int_{E_{in}}^{0} \frac{1}{-\langle \mathrm{dE/dx} \rangle_{\mathrm{water}}} \mathrm{dE} \approx \int_{L} \frac{-\langle \mathrm{dE/dx} \rangle}{-\langle \mathrm{dE/dx} \rangle_{\mathrm{water}}} \mathrm{dL} \,. \tag{1.5}$$

RSP is observed to be approximately constant with less than 0.7% variation in the energy range 70 MeV to 300 MeV relevant for proton imaging and proton therapy, making the equality in Equation 1.5 to be accurate [34]. The WEPL also allows for an easier comparison of reconstructed images from different proton imaging setups.

The WEPL can further be approximated by a simple range-energy conversion known as the Bragg-Kleemann rule [29, 36],

$$R_{\mathrm{water}} = \mathrm{WEPL} \approx a E_{in}^{b} \,, \tag{1.6}$$

where a and b are constants obtained from fitting to experimental range curves.

Another convenient representation is the water equivalent thickness (WET) of the target material crossed, represented by the length a particle would travel in water before losing the same amount of energy [37].

$$\mathrm{WET} = \int_{E_{in}}^{E_{out}} \frac{1}{-\langle \mathrm{dE/dx} \rangle_{\mathrm{water}}} \mathrm{dE} \,. \tag{1.7}$$

E_{in} and E_{out} is the particle energy before and after having traversed the target material. The ionization potential of water (I_{water}) plays an important role in determining the

stopping power, and the values reported by literature range from 75–80 eV resulting in 0.8–1.2% difference in stopping power in the therapeutic energy range and effecting the calculated proton range [38]. The recommended I_{water} value of 78 eV by Kumazaki et al. [38] will be applied in this thesis.

Proton range uncertainties

Accurate insight into the position of the Bragg-peak in particle therapy is critical in ensuring effective tumor irradiation. Because the highest dose-gradient is located inside the Bragg peak at the end of the particle range (Figure 1.1), a small misplacement of the peak can result in severe over-dosage and damage to healthy tissue, and/or under-dosage of the tumor resulting in decreased or loss of tumor control. The most substantial systematic cause of uncertainty in treatment planning is the determination and accuracy of the patient tissue RSP in the path of the particles. For a more detailed investigation of the different systematic and stochastic causes for range uncertainties in proton therapy, see Paganetti [7].

The normal process during treatment planning is to retrieve the patient RSP from a calibration curve connecting the X-ray CT obtained HU with RSP. However, as no physical principle directly and uniquely connects RSP and HU of a material, thus introducing uncertainties in the RSP and with this introduce clinical safety margins (e.g. 3.5% + 3 mm from the Loma Linda medical center [7]) to account for the range uncertainties, resulting in a deliberate dose-deposition into healthy tissue to ensure full dose coverage. This is also a part of the reasoning for not aiming the treatment beam directly at an Organ At Risk (OAR) despite potentially representing the greatest advantage of particle radiotherapy.

1.2.3 Multiple Coulomb scattering

A charged particle traversing matter will interact with obstructing atomic electrons and nuclei by experiencing numerous interactions and undergo potential deflections from its original direction. These interactions lead to scattering, known as Multiple Coulomb Scattering (MCS) and a lateral spread of the particles. Figure 1.3 show a thin pencil beam of 150 MeV protons coming to a stop inside a homogeneous water block simulated using the GATE simulation toolkit [39, 40].

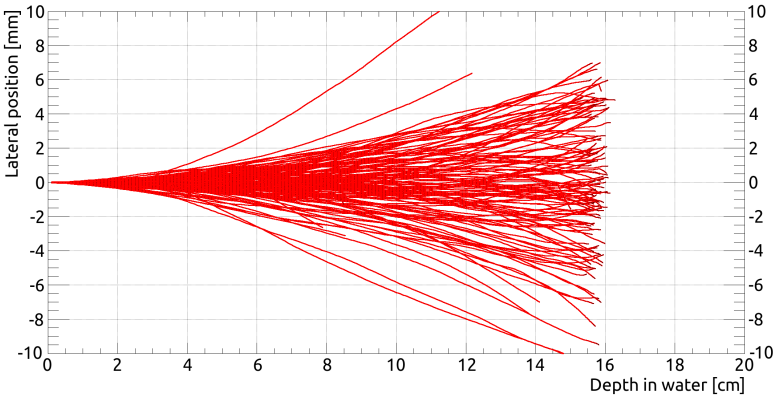

Figure 1.3: The spread of a thin pencil beam consisting of 150 protons with initial energy of 150 MeV. The protons are traversing and coming to a full stop inside a homogeneous water phantom simulated using the GATE Monte Carlo simulation toolkit.

Molière's theory

The exact position and angle of an individual particle at a distinct depth can not be precisely determined due to the stochastic nature of scattering. However, the particle's angular deflection does follow a probability distribution that can be calculated using Molière's transport theory [41, 42]. The angular distribution given by Molière behaves Gaussian in the central small angle region (resulting from multiple small angle deflections) out to about 2.5σ [43]. However, Molière's theory only deals with finite slabs and is not particularly suited for transport calculations that require the instantaneous rate of a particle's angular change of a particle(for example for use in MC simulations).

Fermi-Eyges theory

Fermi introduced a Gaussian approximation to MCS by considering a joint probability of position and angle for a single charged particle in a homogeneous medium [44], this theory was later revised by Eyges to include the energy-loss of the particle [45]. The general Fermi-Eyges theory and a brief overview of the applied concepts are given here.

The goal of Fermi-Eyges theory is to identify the particle's lateral position and angular deflection at some depth position. Since scattering in both the lateral (x) and vertical direction (y) are independent from one another, the two directions can be investigated separately and in turn. Only scattering in the y-direction (vertical) is considered here as

the scattering in x-direction is described equivalently. The probability of finding a particle at a depth position z > 0 with y in dy and θ in dθ can be approximated by a joint Gaussian probability:

$$P(y,\theta)dyd\theta = \frac{1}{2\pi\sqrt{B}}\exp\left(-\frac{1}{2}\frac{A_0(z)y^2 - 2A_1(z)y\theta + A_2(z)\theta^2}{B}\right)dyd\theta \ . \tag{1.8}$$

Where the *scattering moments* $A_n(n \in \{0,1,2\})$ are given as,

$$A_n(z) = \int_0^z (z-z')^n T(z')dz' \ , \tag{1.9}$$

and $B = A_0A_2 - A_1^2$. It can be shown that A_0 represent the variance in θ, A_1 the co-variance of y and θ, and A_2 the variance in y [43]. T represents the *scattering power*. Scattering power is an important concept in Fermi-Eyges theory and represents the rate of angular variance change with depth z in the material:

$$T(z) = \frac{d\langle\theta^2\rangle}{dz} \ . \tag{1.10}$$

T must be defined so that when integrated over, it will accurately reproduce the generally accepted angle calculated with Molière theory. Several approaches to best describe the scattering power exist and a more complete review of the existing definitions can be found in Gottschalk [46]. The most commonly used scattering power formula in Fermi-Eyges theory is the differential Highland (dH) based on the fully generalized Highland scattering formula and proposed by Kanematsu [47].

$$T_{dH}(z) = f_{dH}(l)\left(\frac{15.0}{pv(z)}\right)^2\frac{1}{X_0} \ . \tag{1.11}$$

The factor f_{dH} accommodates for the single scattering effect and depends on the length (l) crossed in the material,

$$f_{dH}(l) = 0.97\left(1+\frac{\ln(l)}{20.7}\right)\left(1+\frac{\ln(l)}{22.7}\right) \ . \tag{1.12}$$

This agrees well with the central part of Molière's theory (up to a few percent) [46], and is relatively easy to use.

1.2.4 Nuclear interaction and secondary particle production

Nuclear interactions in proton radiotherapy and proton imaging are important for several reasons, most critically in this context is the production of secondary particles (secondary protons, neutrons, and photons) depositing dose outside the patient, and loss of primary protons via inelastic nuclear interactions. Approximately 1% of the traversing protons undergo inelastic collisions with nuclei for each centimetre of WET traversed [48]. In this process the primary proton is fully absorbed and, in the context of proton imaging employing an energy detector, will cause a loss of imaging protons decreasing the efficiency of the detector. An overview of relevant nuclear reactions and the secondary particles produced can be found in Paganetti [48].

1.3 Monte Carlo simulations

One of the most reliable and robust methods in computational physics to evaluate and simulate particle transport in matter is the Monte Carlo (MC) simulation method. By having probability distributions containing all physical processes and interactions that occur at the atomic level, it becomes possible to follow and keep a history of an individual particle's energy and path through matter. These probability distributions are obtained from experimental measurements and from validated models of particle interactions that aim to mimic the fundamental interaction processes in nature. For each step the particle takes, a new energy, direction or path length value will be obtained and stored until the particle gets absorbed, leaves the region of interest, or its energy falls below a user defined threshold. In essence, the MC method creates a solution to a macroscopic system by simulating the system's microscopic interactions [49].

As experimental proton imaging data is relatively difficult to obtain due to limited access to the few working prototypes in existence, simulations become very important when investigating new approaches to imaging systems, evaluating detector constructions, or aiding in development and design of new imaging systems [50]. Not the least in reducing development costs and identifying design weaknesses or performance impacts before detector construction.

Several general purpose MC tool-kits are available for particle transportation and radiation physics, the most common of these are GEANT4 (GEometry ANd Tracking) [51, 52] often in combination with GATE (GEANT4 Application for Emission Tomography) [39, 40], and the MC code FLUKA (FLUktuierende KAskade) [31, 53] in combination with the graphical user interface flair [32]. For MC simulations to accurately mimic the real-life system it is simulating, one needs to accurately define the geometry and the material properties in this geometry, enable the relevant physics models to sample interactions from, and use appropriate particle step-sizes and production thresholds. The MC simulation designs and settings made in this thesis using both the GATE and FLUKA MC tool-kits will be explained in chapter 3.

1.4 Thesis objectives and contributions

Several research groups have designed prototype proton CT systems (Table 1.1), but there is no clear consensus on the optimal clinical design and most of the existing designs are based on a imaging system with position sensitive tracker pairs both in front and behind the patient to be imaged (for proton path estimation purposes due to scattering). This type of imaging setup can be used with passively scattered proton beams, but often puts a limit on the rate of incoming protons due to the necessity of correlating hits in the front tracker pair with hits in the rear tracker pair, thus increasing scan times. A proton imaging setup with no front tracker pair will potentially simplify both the physical impact in a treatment room and allow for increased proton rates that in turn reduce scan times, bringing pCT closer to a clinical reality. However, by removing the front tracker pair a deterioration of the path estimation leading to reduced spatial resolution in the reconstructed image is expected.

The overall objective of this thesis is to create a framework based on MC simulations and pre-existing methods that are able to modify proton CT setups, produce data characteristic to the proton CT setup in question, and use this data for MLP estimates and pRad and pCT image reconstruction. The reconstructed images are then analysed in terms of spatial resolution and RSP accuracy.

This framework is then a set of procedures and programs applied in a set order to investigate the impact of removing the front tracker pair in a proton imaging setup in

terms of path estimation accuracy, spatial resolution, and RSP accuracy. As a practical example of applying the simulation framework, the Bergen pCT Digital Tracking Calorimeter (DTC) prototype, designed as a proton imaging system without front trackers, is implemented in simulations and its expected reconstruction proficiency, given by the DTC position resolution on proton hits and the residual energy reconstruction accuracy of traversed protons, is analysed via reconstructed pRad and pCT images.

The following contributions and investigations are defined for this thesis work:

(i) Design of a MC simulation framework usable for proton imaging studies. This includes: A proton pencil beam scanning source with controllable spot weights, spot positions, and spot-spacing. Position sensitive tracker planes of both ideal tracker pairs (no material budget and perfect proton position resolution) and realistic tracker pairs (with material budget and limited proton position resolution). Implementation of a clinically realistic paediatric head phantom, and also standardized reference phantoms designed to characterize the spatial resolution and RSP accuracy of reconstructed images.

(ii) Implementation and application of a pRad and a pCT image reconstruction algorithm to use the MC calculated and scored proton data (proton hits on the imaging setup trackers) from the simulation framework.

(iii) The MC simulation framework is used to simulate proton imaging setups both with and without a front tracker pair to compare the impact on most likely path estimation and the reconstructed image quality when removing the front tracker pair.

(iv) The effect of a reduced pencil beam spot size and spot-spacing are investigated in the imaging setup without front trackers in terms of the effect on the path estimation quality and spatial resolution of reconstructed pRads.

(v) Realistic trackers and energy detector modelled after the Bergen DTC prototype pCT imaging design are implemented in the simulation framework. The image quality based on proton position and WEPL reconstruction proficiency from this DTC is evaluated through an analysis of the resulting most likely path estimation and reconstructed image quality. The realistic DTC setup is compared to the ideal setups to gauge the effect of the trackers and WEPL reconstruction of the DTC.

(vi) The MC simulation framework and image reconstructions are expected to aid in building a strong foundation for future studies, e.g. optimization of imaging dose in terms of image quality, or dose-plan comparisons based on reconstructed proton CT images.

(vii) Included in these MC simulations are investigations and evaluations of the induced radiation environment during both proton therapy and proton imaging when considering the radiation hardness and lifetime of sensitive electronic equipment involved in data read-out from the Bergen DTC.

A flow chart describing the simulation framework steps designed to fulfill the research goals of this thesis are presented in Figure 1.4. Step 1 in the flow-chart consists of the design of the MC simulations, detailing the phantoms, pencil beam source and sensitive tracker planes, including the MC simulation framework settings. Step 2 is preparing the output from the MC simulations (correct format and structure) and doing the data analysis including filtering, path estimation for image reconstruction, WEPL estimation from residual proton energy, and finally image analysis of the reconstructed images. A detailed description of the tools and proton imaging technique is presented in chapter 2. All the main results and investigations presented within this doctoral work are all based exclusively on MC simulations. This means that the simulations have to be reliable and capable of accurately reflecting the characteristics of the real-life system it is simulating, the MC simulation environment built for this thesis is described in chapter 3.

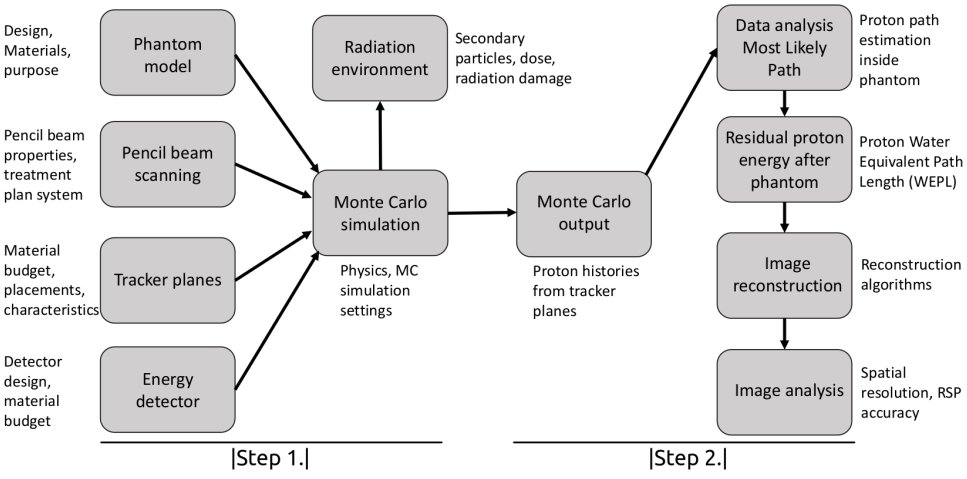

Figure 1.4: Flow chart illustrating the MC simulation framework and analysis steps.

2. Proton imaging

The first pCT imaging modality system idea dates back to 1963, when Cormack [54] proposed using protons for CT scans. Over the past 20 years several pCT prototypes have been proposed and developed attempting to bridge the gap between this first pCT idea and clinical application [10, 18]. While pCT is functionally similar to conventional X-ray CT, the proton interactions with matter will cause the imaging protons to scatter in the patient and make tomographic reconstruction of the proton energy-loss challenging. By introducing position sensitive tracker pairs, both in front and behind the patient to be imaged and measuring the entrance and exit positions of the protons, MLP estimates of the individual proton paths through the patient can be performed and this will improve the spatial resolution of the reconstructed images [55].

Immediately following the rear tracker pair in a proton imaging setup is an energy detector with purpose of accurately recording the residual energy, or WEPL, of the protons exiting the patient, this type of imaging setup is illustrated in Figure 2.1. In order to achieve clinically applicable pCT images, a proton imaging system is expected to meet the following requirements:

(i) **High detection rate**, since a large number of protons is needed to image a patient (in the order of 10^9 protons for a CT of the head) the imaging system must be able to detect and track multiple protons in a single read-out cycle to keep scan times at a reasonable length (preferably < 5 min).

(ii) **High detection efficiency**, to keep the dose to the patient As Low As Reasonably Achievable (ALARA-principle) and also to reduce scan times.

(iii) **High position resolution and low material budget**, accurate and detailed position and direction measurements of the entering and exiting imaging protons are necessary for accurate MLP estimations and thus high resolution images. A low material budget (ratio of detector material thickness and material radiation length) will reduce scattering inside the trackers and reduce deterioration of directional measurements that negatively impact performance and MLP estimates.

(iv) **High RSP resolution**, the energy detector in the imaging system needs to measure

RSP with high precision (<1%) to achieve an image quality that is of clinical relevance in treatment planning.

This chapter details and summarises a proton imaging setup with both front and rear tracker pairs (section 2.1) and a proton imaging setup without a front tracker (section 2.2), the proton MLP implementations (section 2.3), and pRad (section 2.4) and pCT (section 2.5) image reconstruction algorithms applied and used in this thesis work.

2.1 Double-sided proton imaging setup

The conventional proton imaging setup with both front and rear trackers is dubbed *double-sided* in this thesis work and is considered the gold-standard in proton imaging. Substantial investigations of tracking system properties in a double-sided system have been performed by Bopp et al. [24], where the spatial resolution of the trackers, material budget, and distance between the tracker planes in a tracker pair were factored into the MLP accuracy. Their results and observations are: Overall, the position resolution (pixel pitch) and material budget of the trackers should be made as small as possible as not to contribute substantially to the proton position uncertainty, nor induce scattering events affecting the inferred proton direction. The impact of the distance between the two tracker planes when applying a tracker pair is negligible when the distance is more than 5 cm. Based on these results, all distances between the tracker planes (D_t) in each tracker pair in this work was fixed to 5 cm. The effect of the distance between the inner-most tracker planes and patient/phantom to be imaged (D_p) has been investigated by Krah et al. [56] (MLP accuracy as a function of D_p in the range 0–40 cm were investigated) and it was seen in their work that shorter distances are favorable for MLP estimations due to reduced drift (change in position) of the protons. The distance between the inner tracker plane and the object to be imaged is fixed to 15 cm in this thesis work to accommodate space for a potential patient table as the gantry and imaging system rotates around the patient lying on the table (also assuming an average distance of 15 cm from the ear to the tip of the shoulder).

A double-sided imaging setup with ideal trackers will be used as a gold standard and compared to both an ideal and realistic single-sided imaging setup in this work. An illustration of a double-sided setup with the mentioned distances (D_p and D_t) is found in

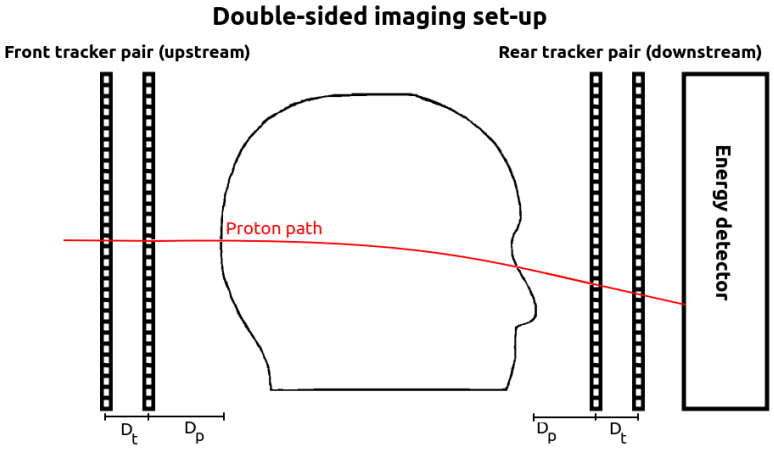

Figure 2.1: Illustration of a double-sided proton imaging setup. D_t is the distance between the position sensitive tracker planes in each tracker pair, and D_p is the distance between the inner tracking plane and the phantom to be imaged.

Figure 2.1.

2.2 Single-sided proton imaging setup

An alternative to the double-sided setup is the *single-sided* setup, where the front tracker pair is removed and the incoming proton positions and directions for use in MLP estimations instead rely on the active pencil beam scanning using the pencil beam spot position and pencil beam angle from the Treatment Planning System (TPS) translated to the Beam Control System (BCS). The single-sided setup is intended to reduce the complexity, cost, and physical impact (less occupied space) on the treatment room where pCT is performed. Also, a double-sided setup can be less practical for acquiring proton data at high particle rates, because: At synchrotron facilities where the beam is typically delivered in bunches lasting 20 to 50 ns spaced 100 to 200 ns apart [57], an increasing particle rate will increase the probability of more than one particle being delivered per bunch and hence, the effective particle rate impinging on the detector becomes much larger than the average rate set in the beam control. So the proton imaging setup would either have to be fast enough to assign a time stamp to every incident particle at the effective rate of the particles within each bunch, or measure a large number of particles simultaneously, as for example in the detector design proposed by the Bergen collabo-

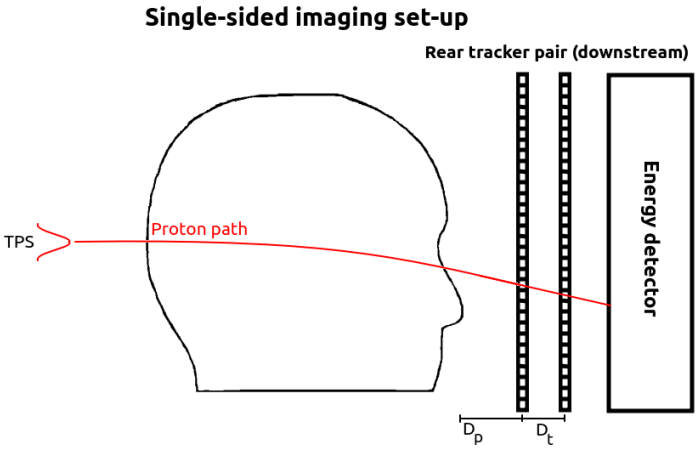

Figure 2.2: Illustration of a single-sided proton imaging system. The front tracker pair is removed and pencil beam information (beam spot-size, angle, and position) from the TPS is used instead. D_t is the distance between the position sensitive trackers in the tracker pair, and D_p is the distance between the inner tracking plane and phantom to be imaged.

ration [19]. However, measuring a large number of particles in the same read-out frame compromises the feasibility of including a front tracker to the imaging setup, as the MCS in the patient makes it difficult to accurately couple particle histories measured on the rear tracker with the measurements on the front tracker. Thus it is of interest to explore the possibility of using a single-sided setup to avoid this pairing of particle histories and instead allow for higher proton rates that will decrease the overall scan time. However, the removal of the front tracker comes at the cost of reduced MLP accuracy due to the inherent position uncertainty of the individual protons inside the pencil beam incident on the phantom, effectively reducing the entrance position accuracy of protons to be used in most likely path estimations [56].

A single-sided imaging setup is illustrated in Figure 2.2. Same as in the double-sided setup, the distance between the remaining sensitive tracker pairs (D_t) is fixed to 5 cm and the distance between the phantom and inner tracking plane (D_p) is 15 cm. This type of setup can be applied to other existing proton imaging prototypes that can safely modify their setup by removing the front tracker pair and apply the appropriate active pencil beam scanning.

2.3 Most Likely Path (MLP)

Initial historical attempts at using a Straight Line Path (SLP) approximation between the entrance and exit positions of protons having traversed an object resulted in low spatial resolution of reconstructed images due to inaccurate distribution of the proton energy-loss. Because of MCS, depending on the proton energy and the type and amount of matter traversed, the path of the protons will deviate from a straight line. A more accurate estimate of the trajectory of each particle will enable a more accurate distribution of the proton energy loss information and improve the spatial resolution of reconstructed pCT and pRad images [55]. Several path estimation methods have been developed over the years, of which the most widely used is the probabilistic MLP formalism that applies the Fermi-Eyges approximation of MCS [56, 58–62]. Based on prior information of the proton in the form of its position and direction at the object entrance and exit via the tracker pairs, finding the MLP of a proton can be formulated as a maximum likelihood problem applying a Bayesian framework. Schulte et al. [60] made a general and compact matrix notation formalism of the MLP that is used to this day, and this formalism computes the scattering moments $A_0, A_1, \text{and} A_2$ that are needed when applying the Fermi-Eyges theory. We use the same scattering moments from Eqs. 7–9 in the work by Schulte et al. [60] that are based on the generalized Highland scattering power. These are repeated for completeness in Equation 2.1, 2.2, and 2.3.

$$A_0(z_0,z) = \sigma_\theta^2(z_0,z) = \frac{E_0^2}{X_0}\left(1+0.038\ln\left(\frac{z-z_0}{X_0}\right)\right)^2 \int_{z_0}^{z} \frac{1}{(p(z)v(z))^2}\,dz, \tag{2.1}$$

$$A_1(z_0,z) = \sigma_{t\theta}^2(z_0,z) = \frac{E_0^2}{X_0}\left(1+0.038\ln\left(\frac{z-z_0}{X_0}\right)\right)^2 \int_{z_0}^{z} \frac{(z-z_0)}{(p(z)v(z))^2}\,dz. \tag{2.2}$$

$$A_2(z_0,z) = \sigma_t^2(z_0,z) = \frac{E_0^2}{X_0}\left(1+0.038\ln\left(\frac{z-z_0}{X_0}\right)\right)^2 \int_{z_0}^{z} \frac{(z-z_0)^2}{(p(z)v(z))^2}\,dz, \tag{2.3}$$

Here, $E_0 = 13.6\,\text{MeV/c}^2$ is a constant, X_0 is the radiation length of the material, $p(z)$ is the momentum, and $v(z)$ the velocity of the particles as function of depth between z_0 and z. $\sigma_t^2(z_0,z)$ describes the lateral variance, $\sigma_\theta^2(z_0,z)$ the angular variance, and $\sigma_{t\theta}^2(z_0,z)$ the spatial-angular co-variance at depth z for particles propagating from z_0 to z. It is straightforward to apply the same scattering moments to the exit parameter at depth

Table 2.1: The results from the polynomial fit

Coefficient	Value
a_0	5.77059 e-6
a_1	2.74001 e-7
a_2	-2.49026 e-8
a_3	4.63381 e-9
a_4	-2.65153 e-10
a_5	6.22291 e-12

z_1 by replacing z_0 with z, and z with z_1 in Equation 2.1, 2.2, and 2.3. As proposed by Williams [59], the integrals in these scattering matrix elements were computed analytically by using a parameterization of the $1/(p(z)v(z))^2$ function obtained as a fifth order polynomial fit (Equation 2.4) to the function based on MC simulated proton energy while traversing a homogeneous water phantom from 0 to 20 cm depth (z) in steps of 1 mm. The coefficients of the polynomial fitted to the $1/(p(z)v(z))^2$ function made with MC data using the MC settings and physics-list described later in section 3.1 are listed in Table 2.1.

$$\frac{1}{p^2(z)v^2(z)} = \frac{(E(z)+E_p)^2c^2}{(E(z)+E_p)^2E^2(z)} \approx a_0 + a_1z + a_2z^2 + a_3z^3 + a_4z^4 + a_5z^5 \,. \tag{2.4}$$

The full derivation of the matrix-based MLP formalism is not repeated in this thesis, but the reader is directed to the publication from Schulte et al. for the full details.

The MLP formalism by Schulte et al. [60] was recently extended by Krah et al. [56] to include experimental uncertainties in the form of Gaussian descriptions of the uncertainty involved in measuring the proton positions and directions via realistic tracker pairs. All detectors and tracker pairs have a finite material budget and position resolution that will affect the position and angle of protons on the trackers. Depending on the amount of scattering that occurs in the material and the position resolution of the trackers, the MLP accuracy will be reduced. Either by an erroneous assignment of the proton position on the contour of the phantom found along the proton trajectory determined by the tracker pair, or by applying the MLP estimations with an initial and final position or angle that fails to reflect the actual entrance and exit position and angle of the proton on the patient. As mentioned in the work by Krah et al. [56], the inclusion of experimental uncertainties from trackers in MLP estimations can potentially be ignored due to the inherent uncertainty of MCS becoming more dominant for larger phantoms

(i.e. 20 cm) and the typically low uncertainty of modern detection technologies. Nevertheless we will see that the experimental uncertainties concerning the pencil beam spot size and their inclusion via the extended-MLP formalism by Krah et al. [56] become very important for accurate MLP estimations in a single-sided setup.

An important assumption in MLP estimations is that homogeneous water is considered as the traversed material affecting the proton scattering, this is because no prior information about the traversed patient tissue is typically available, and the underlying MLP estimation methods from Schulte et al. [60] and Krah et al. [56] are based purely on water as the traversed media (represented by the radiation length of the material in the scattering moments Equation 2.1, 2.2, and 2.3). It has been observed in other studies that the homogeneous water assumption is an accurate and valid approximation for many patient geometries and materials, except if large amounts of bone or air is present in the proton path [63–65]. The study by Collins-Fekete et al. [64] observed that if a hull algorithm is used to recognizing the contour of a anthropomorphic head, lung, and abdomen phantom, and thus use the initial and exit proton positions placed directly on the phantom contour in MLP estimation, instead of the measured positions directly from the trackers, then the MLP estimations based on homogeneous water performed similarly as when prior knowledge about the phantom material was known and accounted for.

Hull algorithm

A hull algorithm [66] assuming protons travelling in straight lines in air (radiation length in air is 303 m [67] making this is a reasonable assumption) is applied to all image reconstructions in this thesis work and is performed before any MLP estimations are made. This hull-algorithm assumes that the phantom geometry and its placement is known in relation to the tracker pairs, this can be assumed with prior information from diagnostic CT-scans and treatment positioning of the patient. The proton positions on the trackers are propagated in straight lines along their inferred directions until reaching the contour of the phantom. This effectively improves the accuracy of the MLP and reconstruction as reported by Collins-Fekete et al. [64]. However, the accuracy of the proton position on the hull will be affected by the distance between the trackers and the phantom (D_p), and by the amount of scattering in the tracker planes affecting the proton

direction that is propagated along in the hull algorithm. This will potentially shift the expected entrance and exit positions on the hull away from their actual positions, as is observed in Krah et al. [56] and in section 5.1 of this thesis. If no contour is found (the proton has not entered the phantom) the proton positions on the trackers are used for the MLP.

2.3.1 Extended-MLP in a single-sided imaging setup

MLP estimation in a single-sided imaging setup employing pencil beam scanning differs from a double-sided setup due to the inherent position uncertainty of incoming protons inside the pencil beam spot size, this is the main limiting factor in MLP estimation accuracy in a single-sided setup [56]. To minimize the error in the proton path estimation associated with the absence of the front tracker, the *extended-MLP* formalism developed by Krah et al. [56] was employed in this work. In this formalism, the TPS parameters (mean beam position and beam direction) are used in the MLP estimation and the uncertainty of these parameters are accounted for by including the beam co-variance matrix following section 2.6 in their work. Before the extend-MLP was performed, the hull projection algorithm was applied to project the proton position from the rear trackers along its inferred direction and onto the back of the phantom contour before the most probable entrance position of the proton was estimated using the extended-MLP. This new estimated proton entrance position was thus propagated along its estimated angle until reaching the contour of the phantom, resulting in the most probable entrance and exit proton position and angle on the phantom surface, given the prior information from the TPS and rear tracker measurement. These new positions and angles were then used to perform the full MLP estimation for use in image reconstruction in a single-sided imaging system.

The extended-MLP formalism and its components are repeated here for completeness. The most likely parameter vector of the proton, $y_{MLP}(z)$ (position and angle) at some depth z, given as:

$$y_{MLP}(z) = C_2(C_1+C_2)^{-1}R_0S_{in}\cdot\tilde{y}_{in,d} + C_1(C_1+C_2)^{-1}R_1^{-1}S_{out}^{-1}\cdot\tilde{y}_{out,d} \tag{2.5}$$

With

$$C_1 = R_0 S_{in} \Sigma_{in} S_{in}^T R_0^T + \Sigma_1 \tag{2.6}$$

$$C2 = R_1^{-1} S_{out}^{-1} \Sigma_{out} (S_{out}^{-1})^T (R_1^{-1})^T + R_1^{-1} \Sigma_2 (R_1^{-1})^T. \tag{2.7}$$

Where the scattering matrices Σ_1 and Σ_2 contain the scattering moments from Equation 2.1,2.2, and 2.3 applied to the entrance and exit parameter vectors respectively. R_0 and R_1 are small angle rotation matrices projecting the proton from z_{in}, z_{out} to z.

$$\Sigma_1 = \begin{pmatrix} \sigma_{t_1}^2 & \sigma_{t_1\theta_1}^2 \\ \sigma_{t_1\theta_1}^2 & \sigma_{\theta_1}^2 \end{pmatrix}, \; \Sigma_2 = \begin{pmatrix} \sigma_{t_2}^2 & \sigma_{t_2\theta_2}^2 \\ \sigma_{t_2\theta_2}^2 & \sigma_{\theta_2}^2 \end{pmatrix}, \tag{2.8}$$

$$R_0 = \begin{pmatrix} 1 & z - z_{in} \\ 0 & 1 \end{pmatrix}, \; R_1 = \begin{pmatrix} 1 & z_{out} - z \\ 0 & 1 \end{pmatrix}. \tag{2.9}$$

S_{in} and S_{out} are the back-projection matrices, projecting the measured parameter vectors $\widetilde{y}_{in,d}$ and $\widetilde{y}_{out,d}$ along straight lines onto the surface of the phantom given the distance between the inner tracker pair and phantom surface, D_P. If a separate hull-algorithm is used, D_P is set to 0 and $\widetilde{y}_{in,d}$ and $\widetilde{y}_{out,d}$ are then the parameter vectors located on the entrance and exit on the contour of the phantom.

$$S_{in} = \begin{pmatrix} 1 & D_P \\ 0 & 1 \end{pmatrix}, \; S_{out} = \begin{pmatrix} 1 & D_P \\ 0 & 1 \end{pmatrix}, \; \widetilde{y}_{in,d} = (t_{in}, \theta_{in}), \; \widetilde{y}_{out,d} = (t_{out}, \theta_{out}). \tag{2.10}$$

The co-variance matrices Σ_{in} and Σ_{out} with respect to the front and rear tracker pair properties and their measurement uncertainties are,

$$\Sigma_{in} = \sigma_p^2 T_{in} \cdot T_{in}^T + \Sigma_{sc} \text{ and } \Sigma_{out} = \sigma_p^2 T_{out} \cdot T_{out}^T + \Sigma_{sc}. \tag{2.11}$$

σ_p is the inherent position resolution of the tracker, and the scattering σ_{sc} due to the material budget of the tracker (x/X_0) as obtained from equation 12 in Lynch and Dahl [68], is

$$\Sigma_{sc} = \begin{pmatrix} 0 & 0 \\ 0 & \sigma_{sc}^2 \end{pmatrix}, \text{ with } \sigma_{sc} = \frac{13.6\text{MeV}}{\beta(E)p(E)} \sqrt{\frac{x}{X_0}} \left[1 + 0.038 \ln\left(\frac{x}{X_0} \right) \right] \tag{2.12}$$

T_{in} and T_{out} help form the direction parameter based on the distance between trackers

D_t,

$$T_{in} = \begin{pmatrix} 0 & 1 \\ -\frac{1}{D_t} & \frac{1}{D_t} \end{pmatrix}, \; T_{out} = \begin{pmatrix} 1 & 0 \\ -\frac{1}{D_t} & \frac{1}{D_t} \end{pmatrix}. \tag{2.13}$$

In a single-sided imaging set-up employing pencil beam scanning without a front tracker pair the co-variance matrix Σ_{in} becomes,

$$\Sigma_{in} = \begin{pmatrix} 1 & 0 \\ \frac{1}{D_s} & 1 \end{pmatrix} \cdot \begin{pmatrix} \sigma^2_{t_{in}} & 0 \\ 0 & 0 \end{pmatrix} \cdot \begin{pmatrix} 1 & \frac{1}{D_s} \\ 0 & 1 \end{pmatrix} + \begin{pmatrix} 0 & 0 \\ 0 & \sigma_{\theta^2_{in}} \end{pmatrix} \tag{2.14}$$

The uncertainty parameter $\sigma_{t_{in}}$ represent the Gaussian beam size at the isocentre, $\sigma_{\theta_{in}}$ quantifies the angular confusion of the pencil beam. D_s is the distance of the beam point source (i.e. the scanning magnets) from the isocentre.

2.3.2 Cubic spline path

An alternative formalism to the probabilistic MLP estimation detailed above is the optimized Cubic Spline Path (CSP) from Collins-Fekete et al. [69]. The CSP formalism follows the recommendations from Hansen et al. [70] and Li et al. [55] to estimate the proton path using a curved proton trajectory between the known entrance and exit position of the proton. This formalism is implemented in the pCT reconstruction algorithm used in this thesis work to reduce computation time. The cubic spline equation is represented in Equation 2.15.

$$\mathbf{S}(t) = (2t^3 - 3t^2 + 1)\mathbf{X}_0 + (t^3 - 2t^2 + t)\mathbf{P}_0 + (-2t^3 + 3t^2)\mathbf{X}_1 + (t^3 - t^2)\mathbf{P}_1 \, . \tag{2.15}$$

Here the entrance and exit position vectors of the proton are $\mathbf{X}_0$ and $\mathbf{X}_1$, and its direction vectors $\mathbf{P}_0$ and $\mathbf{P}_1$ as obtained after finding the position and angle on the hull. $\mathbf{S}(t)$ represents the position vector at any given temporal variable t ($t \in [0,1]$, where t=0 is the start point and t=1 is the end point) between the entrance and exit position of the proton. This cubic spline was optimized via a phenomenological approach by Collins-Fekete et al. [69] and introduced two optimization factors in the direction vectors that minimize the Root Mean Square (RMS) difference between the CSP path and ground

truth path. The optimized direction vector magnitudes are

$$\mathbf{P}_0 = \mathbf{P}_0 \cdot \Lambda_0^{\text{opt}} \cdot |\mathbf{X}_1 - \mathbf{X}_0| \ , \ \mathbf{P}_1 = \mathbf{P}_1 \cdot \Lambda_1^{\text{opt}} \cdot |\mathbf{X}_1 - \mathbf{X}_0| \ . \tag{2.16}$$

Where the optimization factors as function of the measured and calculated WET/WEPL ratio of the material are,

$$\Lambda_{0,1}^{\text{opt}} = \text{A} + \text{B}(\text{WET}/\text{WEPL})^2, \tag{2.17}$$

with A=1.01 and B=0.43 for Λ_0^{opt}, and A=0.99 and B=-0.46 for Λ_1^{opt}. This optimized CSP closely follows the probabilistic MLP by Schulte et al. [60], but with the added benefit of reduced computational effort and time, as well as an easier implementation in path estimations.

2.4 Proton radiography reconstruction

Proton radiographies were reconstructed using the maximum likelihood image reconstruction method developed by Collins-Fekete et al. [71]. This algorithm offers a reconstructed pRad where each image pixel contain the proton WET calculated as a weighted mean over all protons crossing into a channel through the object, the estimated proton path from the extended-MLP dictates which channels are crossed. The channel correspond to the area of the image pixel and is connected to the full length of the object to be imaged. A schematic view exemplifying this pRad reconstruction is shown in Figure 2.3. The weighted WET inside channel k, WET_k, is given in Equation 2.18 as the measured WEPL of proton n, weighted by the the length l spent inside channel k divided by L_n, the total length of the channel given as the depth between the entrance and exit position obtained from the hull-algorithm used in the extended-MLP.

$$\text{WET}_\text{k} = \frac{\sum_\text{n}^\text{N} \frac{\text{l}_{\text{k,n}}^2}{\text{L}_\text{n}^2} \text{WEPL}_\text{n}}{\sum_\text{n}^\text{N} \frac{\text{l}_{\text{k,n}}^2}{\text{L}_\text{n}^2}} \ . \tag{2.18}$$

The pixel/channel size in pRad of water box based phantoms were set to $0.25 \times 0.25\,\text{mm}^2$, and for the anthropomorphic head phantom it was $0.75 \times 1.25\,\text{mm}^2$. These phantoms are described in section 3.3 of this thesis. A ground-truth pRad of the head phantom was

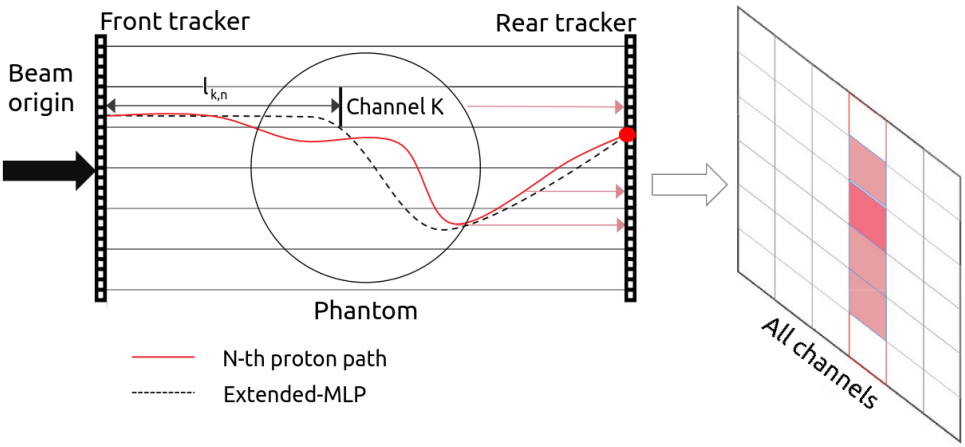

Figure 2.3: Schematic view of the pRad reconstruction method. The front and rear tracker with the phantom discretized into channels is shown. The red line represent the path of a single proton, the dotted line the proton's MLP path. On the right, the activated pixels are shown and weighted depending on the length l, crossed by proton n, in channel k. Figure is re-drawn from Collins-Fekete et al. [71].

reconstructed by integrating over the MC ground-truth RSP of every involved voxel of the reconstruction area covering the head phantom, this is used in evaluating pRad WEPL errors.

Before pRad reconstruction, a 2.5σ cut-off filter on the proton angles was applied to cut large angle scattering not described by the Fermi-Eyges theory underlying the MLP [43, 60]. A 2.5σ-filter on the WET of the protons was also applied to remove unusually large energy losses and nuclear interactions [72] and is sufficient to ensure high quality images [73].

2.5 Proton CT reconstruction

Similarly to conventional X-ray CT imaging, the goal of pCT is to solve a linear system of equations,

$$\mathbf{A}\mathbf{x} = \mathbf{b}\ . \tag{2.19}$$

Where $\mathbf{A}$ is an $n \times m$ system matrix with the elements a_{ij} corresponding to the intersection length of the path of the i-th proton with the j-th image voxel. $\mathbf{A} = a_{i,j} (i \in \{0, 1, ..., n\}$, $j \in \{0, 1, ..., m\})$, $\mathbf{x}$ is the unknown RSP m-dimensional vector, and $\mathbf{b}$ is the n-dimensional

vector containing the calculated WEPL from measurements.

Since protons will experience MCS, causing the protons to deviate from a straight line path, conventional fast X-ray CT reconstruction algorithms that solve Equation 2.19 will result in poor image quality when applied directly to proton imaging [55]. X-ray CT reconstruction algorithms therefore need to be modified with MLP estimation algorithms to produce accurate images. The often used Filtered Back Projection (FBP) reconstruction algorithms from X-ray CT have been adapted for pCT purposes [74, 75], but due to the uncertainty of the proton path estimation, the system of equations (Equation 2.19) will be inconsistent and difficult to solve via FBP. Also, as each proton only crosses a small percentage of the total voxels (m), the system matrix **A** will be large and sparse depending on the number of protons and require a large number of projections (e.g. 360 projections or more). Therefore, iterative reconstruction algorithms are most commonly used in proton CT to solve Equation 2.19. A review of available iterative reconstruction algorithms for pCT is available in [76].

For solving $\mathbf{Ax} = \mathbf{b}$ iteratively and reconstructing pCT images in this thesis work, the Diagonally-Relaxed Orthogonal row Projection (DROP) reconstruction algorithm with Total Variation Superiorization (TVS) [77] for producing accurate images with few projections was used. This algorithm is a feasibility seeking method with interlaced TVS that reduces the image noise without reducing the sharpness between boundaries of materials. Feasibility seeking algorithms in pCT tend to emphasize RSP variations due to increased WEPL uncertainty in regions between low and high density materials (high-gradient regions) and thus sharpens the edges in such high-gradient regions, but also amplifies the RSP fluctuations during iterative image reconstruction. By performing TVS between feasibility seeking iterations the growth of these RSP variations slows down and thus reduces noise while conserving the sharpness of high-gradient regions [78].

Prior to the iterative reconstruction, three-sigma cuts on WEPL, angle, and vertical and horizontal deviation filtered out protons that underwent large-angle scattering and/or energy-loss. An analytical Feldkamp-David-Kress (FDK) CT reconstruction, the cone beam version of FBP, based on rear tracker binning finds the contour of the phantom and produces the starting point for the DROP-TVS reconstruction algorithm. For computational efficiency, only the entrance and exit points of each protons were calcu-

lated from the extended-MLP formalism, and the optimized CSP [69] was interpolated in between. This approximates the performance of the full extended-MLP formalism, but retains the run-time benefit of the CSP algorithm.

The slice thickness was set to 1.25 mm for all phantoms, and 455×455 pixels (0.35 mm pixel size) per slice (32 slices in total) for the reconstruction of the CTP404 and CTP528 phantom, and 240×240 pixels (0.75 mm pixel size) per slice (112 slices in total) were set for the head phantom (detailed in section 3.3). Based on other studies and recommended settings from experienced users of the DROP-TVS algorithm for pCT reconstructions [21, 79], the proton histories were divided into 40 optimization blocks per iteration and the algorithm was stopped after 8 iterations, with the relaxation parameter set to 0.1.

2.6 Image measures

Modulation transfer function

The spatial resolution of pRad and pCT images acquired with single- and double-sided imaging setup were compared using the Modulation Transfer Function (MTF) [56, 80]. The Edge Spread Function (ESF) was computed for every contrast region of interest in the reconstructed image and fitted with an error function to suppress noise. The derivative of the fits yielded the Line Spread Functions (LSF), and the MTF was finally obtained as their Fourier transform. As a metric for comparison the spatial frequency lp/cm at which the MTF drops below the 10% level was used.

For the pCT reconstructions of the Catphan® CTP528 line pair module (phantom modules are detailed later in section 3.3), the MTF was assessed from the maximum-minimum contrast measured for each set of line pairs relative to the reference contrast. Following Piersimoni et al. [79], a discrete MTF was obtained from the contrast $C(f)$ between adjacent maxima and minima in a profile over the line pair inserts of the same spatial frequency f(lp/cm). For a robust estimate, the contrast was averaged over all pairs of adjacent maxima and minima corresponding to the same spatial frequency in Equation 2.20. The contrast at $f = 0$ was obtained using the peak RSP value reconstructed for the 1 lp/cm aluminium insert and the RSP reconstructed for the epoxy material for

the ideal double-sided reconstruction.

$$\mathrm{MTF(f)} = \frac{\mathrm{C(f)}}{\mathrm{C(0)}}, \text{ where } \mathrm{C(f)} = \left\langle \frac{\mathrm{RSP_{max}} - \mathrm{RSP_{min}}}{\mathrm{RSP_{max}} + \mathrm{RSP_{min}}} \right\rangle. \tag{2.20}$$

WEPL error and noise in proton radiography

The WEPL errors of reconstructed pRad of a anthropomorphic head phantom were quantified by the difference between the WEPL in the image pixel in the reconstructed pRad and the corresponding WEPL in the pixel in the ground-truth pRad.

Additionally, the noise in each image pixel was obtained as the standard error of the mean of the weighted WEPL distribution in that pixel, where the weights were the same ones used in the image reconstruction from the algorithm by Collins-Fekete et al. [71].

For pRad of water based phantoms with aluminium inserts, the contrast-to-noise ratio (CNR) of relevant inserts was evaluated using,

$$\mathrm{CNR} = \frac{\overline{\mathrm{WET}}_{\mathrm{insert}} - \overline{\mathrm{WET}}_{\mathrm{Water}}}{\sqrt{(\sigma_{\mathrm{insert}})^2 + (\sigma_{\mathrm{water}})^2}}. \tag{2.21}$$

Where $\overline{\mathrm{WET}}_{\mathrm{insert}}$ and σ_{insert} are the mean and standard deviation, respectively, of WET values in the central area ($2.5 \times 2.5\,\mathrm{mm}^2$) of the aluminium insert. $\overline{\mathrm{WET}}_{\mathrm{Water}}$ and σ_{Water} are the mean and standard deviation of the reconstructed WET values of the homogeneous water tank. A total of 100 image pixels were used for calculating each mean and standard deviation.

2.7 Bergen digital tracking calorimeter

A proof-of-concept of a Digital Tracking Calorimeter (DTC) based on results obtained using an ALICE-FoCal collaborative DTC prototype showed that the CMOS MAPS technology can be used for proton imaging purposes with good WEPL resolution and high readout speed ensuring low scan times [81].

The ALICE PIxel DEtector (ALPIDE), a CMOS MAPS based sensor chip, is developed for the upgrade of the Inner Tracking System (ITS) of the ALICE experiment at the CERN Large Hadron Collider (LHC) [82, 83]. The ALPIDE measures 15 mm by 30 mm and includes 512×1024 pixel cells designed to achieve a position resolution of

5 μm on hits, this sensor chip is the foundation of the Bergen DTC prototype to be used for proton imaging purposes [19]. Detailed design optimization studies have been performed by Pettersen et al. [84] using MC simulated data and focused on optimizing the DTC absorber material and absorber thicknesses between sensitive ALPIDE layers in terms of WEPL accuracy and tracking efficiency of protons. Based on the expectation of the prototype performance, dimension of reconstruction volume to be imaged (patient head), and results from the simulated data, some design recommendations were presented (see the work by Pettersen et al. [84] for detailed descriptions of the design optimization efforts):

- In the longitudinal direction, the DTC should comprise of alternate layers of ALPIDE sensors and aluminium absorber layers. Based on the track reconstruction efficiency and reconstructed WEPL accuracy, the thickness of the absorber should be kept as low as possible, strictly below 4 mm. In this fashion, 41 layers, each made of ALPIDE chips supported by 3.5 mm-thick aluminium absorbers are recommended to fully encompass the dynamic range of protons up to 230 MeV.

- Two layers in front of the DTC will function as the rear position sensitive tracker pair. Therefore, they should contain as little material as possible to reduce scattering and subsequent deterioration of proton angle measurements used in proton path estimations inside the patient. This is achieved by thinning down the material budget of the supports on which the tracker pair ALPIDEs will be mounted.

- Proton Readout Units (pRU) must be able to handle the combined data from 10 M protons per second (10 MHz) to ensure low scan times.

Figure 2.4 is a section render of the DTC design (as of August 2020) showing the two front tracker layers spaced 5 cm apart, followed by the sandwiched 41 ALPIDE/aluminium absorber layers and associated transition cards used to communicate with the DTC and its ALPIDE chips. More details about this DTC design, proton CT readout units (pRU) and system architecture is presented in the Bergen pCT 2020 status paper [19]. The MC model of this detector designed for use in this thesis work will be explained in section 3.4.

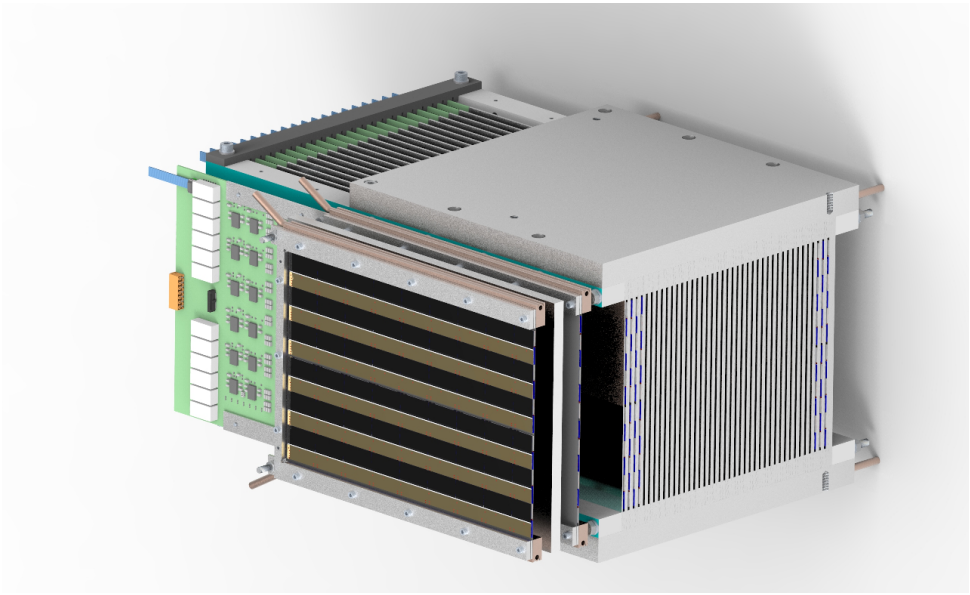

Figure 2.4: Sectional three dimensional rendering of the DTC design. The light green structures on the side are transition cards. The two front layers consisting of alternating ALPIDE chips are mounted on 0.2 mm thick carbon fiber sheets, followed by 41 layers of ALPIDE mounted on 3.5 mm thick aluminium absorbers. Light grey aluminium support structures at the top and bottom ensure that the layers are fixed in place. Courtesy of Ton Van Den Brink, Utrecht University.

3. Monte Carlo simulation for proton imaging

A proton imaging framework based on Monte Carlo simulations with the intention of investigating and demonstrating the feasibility of using a single-sided proton imaging setup, including the Bergen DTC prototype setup, was designed for this thesis work. The overall motivation being: By obtaining MC calculated proton data for use in image reconstruction and subsequently analyse the resulting image quality, the image quality impact and potential application of a single-sided imaging setup could be estimated. The simulation framework is also expected to function as a foundation for future studies potentially bringing proton imaging closer to a clinical reality. To achieve this, the MC simulations were to be built using existing and well validated MC tool-kits, i.e. GEANT4 (GEometry ANd Tracking), and make use of the many pre-defined mechanisms to tailor and describe a proton imaging setup with tracker planes and relevant phantoms that can be readily modified or exchanged depending on the imaging setup characteristics to be investigated. This MC simulation framework is described in its entirety in this chapter and consists of MC simulation settings (physics, material definitions), the proton beam source (beam scanning), implemented phantoms to be imaged, and tracker plane characteristics (placements, material budgets).

The simulations in this thesis were designed and performed on a Lenovo laptop with an Intel® Core™ i5-6300U CPU @ 2.40 GHz × 4, and a Lenovo desktop with an Intel® Xeon(R) CPU E5-2620 v4 @ 2.10 GHz × 16. Both computers were running on the Ubuntu 18.04.5 LTS operative system. All data processing and analysis are developed and performed using ROOT 6.18 [85].

3.1 GATE

GATE (GEANT4 Application for Emission Tomography) is a general purpose MC tool-kit focused on particle transportation and medical radiation physics [39, 40]. This tool-kit overlays GEANT4 (GEometry ANd Tracking) [51, 52] taking advantage of its well-validated physics models and sophisticated geometry description for use in high-energy physics. The GATE MC tool-kit is dedicated to simulations in medical imaging and ra-

diotherapy using a scripting mechanism (macros) to configure and perform detailed GEANT4 simulations with relative ease and speed. GATE contains hundreds of predefined mechanisms to build and manage complicated geometries, radiation sources, and logging interaction histories and particles through actors/sensitive volumes, making it possible to perform and design GEANT4 MC simulations of complex and realistic setups in medical physics and technology.

Geometry and material definition

Each geometric volume in a MC simulation is characterized by its shape, size, position, and material composition. Materials are defined in a material database holding all the information required for GATE to assign the nuclear properties from the GEANT4 data sets. This material database contains two GEANT4 structures called elements and compounds that are used to define the physical properties of the atoms, molecules, and compounds involved in the materials used in the simulation. An element in GATE stores the name, symbol, atomic number, and molar mass of the element. A compound is a combination of elements and is used by GATE to assign material properties to geometric volumes during a simulation. These combinations of elements require defining four additional parameters; the material's name, density, constituent element(s), and their relative mass fractions. Such materials and compounds must be carefully chosen and correctly defined as they can vary greatly and should accurately mirror the materials involved in the realistic set-up to be investigated. Material definitions and properties included in this thesis are listed in Table 3.3.

The RSP of water and the involved materials in the MC simulations needed for accurate evaluation of the reconstructed RSP values from proton imaging was obtained directly from the GEANT4 code underlying the GATE simulation. The average RSP of the involved materials were obtained by calculating the stopping power in the material at steps of 0.01 MeV in the region between 70 MeV and 300 MeV and dividing by the corresponding stopping power in water. These average reference RSP values for each material are collected in the last column in Table 3.3.

Physics and step-size

Alternative physics models and step-limits are applicable and recommended depend-

ing on the problem being simulated, e.g. high or low energy region, particle species to be transported. For this reason various reference *physics lists* are defined and available in GEANT4. For medical physics simulations the recommended physics list is *QBBC_EMZ*, this contains a proven set of electromagnetic physics models selected from the low energy and standard packages [86–88].

The most important processes for determining the trajectory of a charged particle are the multiple scattering process and the transportation process. Simulation of particle transport in MC is performed step-by-step and in principle one must use small steps in order to ensure an accurate simulation, however the computing time increases as the step-size decreases. In GEANT4 the step-size (ΔS_{lim}) is controlled by its *G4SteppingManager* and the electromagnetic step-sizes are limited by a continuous *StepFunction* [89],

$$\Delta S_{lim} = \alpha_R + \rho_R(1-\alpha_R)\left(2-\frac{\rho_R}{R}\right). \tag{3.1}$$

Where the two default parameters α_R (step/range) and final range ρ_R, set by default in the electromagnetic option 4 (EMZ) [89] to be: for electrons $\alpha_R = 0.2$ and $\rho_R = 0.01\,\text{mm}$, and for protons $\alpha_R = 0.1$ and $\rho_R = 0.02\,\text{mm}$ [90]. The step size gradually decreases until the range becomes lower than ρ_R at which the step-size becomes equal to the range of the particle. The particle is then tracked down to zero energy using continuous energy loss. If the primary particle does not have enough energy to produce secondaries that have a range larger than 1 mm (production cut), then the secondary particle production stops. In this thesis, the default step-lengths from the EMZ option and secondary production threshold (1.0 mm) are used in all simulations.

For more in-depth details about the underlying physics models in the QBBC_EMZ physics list, see the GEANT4 Physics Reference Manual [91] and Ivantchenko et al. [86].

Scoring (measurements)

To interact with the simulations and output the relevant quantities, be it particle type, position, energy, dose deposition, etc. GATE offers several different *actors* tasked with measuring the quantities that the user is interested in. In this work the *phase space actor* is used to record the position, energy, and particle name of particles entering/exiting a volume of choice. In the ideal tracker simulations, these sensitive volumes are thin

planes made of air, same as the surroundings (i.e. zero material budget), and located at the same position as the tracker pairs in the imaging setup. A phase space actor is then attached to these planes functioning as trackers. These trackers record the x, y, and z position of the particles, their energy, and particle name. These position measurements were then used as input to the MLP, and the energy in subsequent WEPL/RSP calculation detailed in section 3.5. The recorded particle names also allow for easier filtering of secondaries to be excluded from image reconstruction. For the more realistic simulations where the tracker planes have material budgets modelled after the Bergen DTC, to be detailed later in section 3.4, the phase-space actors are attached to the sensitive ALPIDE/silicon volumes of the trackers. The inherent position resolution of the tracker technologies were included by sampling from a Gaussian with a standard deviation based on the position resolution of the tracker technology listed in Table 1.1.

3.2 Proton beam source

Pencil beam properties

Another important setting in MC simulations is the definition and application of the radiation source properties. A pencil beam scanning system is used in this thesis, and a pencil beam is defined by its beam spot properties at the isocentre in a treatment room and by the pencil beam properties passed on by the beam delivery system. These spot properties include the particle energy, energy spread, spot-size in x- and y-direction, spot-divergence and spot-emittance. In a Treatment Planning System (TPS) the spot-weight in terms of number of particles in each spot-position at the isocentre is also involved. A realistic pencil beam setting found at the Heidelberg Ion Beam Therapy Center (HIT) [92] was used as a foundation for the 7 mm Full Width Half Maximum (FWHM) thick pencil beam used for proton imaging purposes in this thesis. A smaller pencil beam with reduced lateral uncertainty and size is expected to increase the spatial resolution in a single-sided setup [56]. Hence, another smaller pencil beam with a thickness of 3 mm FWHM was investigated. The exact details of the pencil beam properties and TPS settings are listed in Table 3.1. Smaller spot spacing, as a function of pencil beam FWHM, was also investigated following the rational that a denser packing of protons corresponding to the Gaussian center of the beam spot could increase

TPS source characteristics

Energy	230 MeV
Nozzle exit to iso-centre distance	500 mm
Scanning magnet X to iso-centre distance	6600 mm
Scanning magnet Y to iso-centre distance	6600 mm

Pencil beam characteristics

Beam characteristic [FWHM]	3 mm	7 mm
Spot size in x (standard deviation) [mm]	1.3	3.0
Spot size in y (standard deviation) [mm]	1.3	3.0
Spot divergence theta [mrad]	2.8	2.8
Spot divergence phi [mrad]	2.8	2.8
Spot emittance theta [mm*mrad]	3.0	3.0
Spot emittance phi [mm*mrad]	3.0	3.0

Table 3.1: TPS set-up settings and 3, and 7 mm FWHM pencil beam characteristics used to investigate image quality. All pencil beam characteristics are confirmed with MC at the iso-centre of the simulation coordinate-system.

the image accuracy in pRad with the reconstruction algorithm by Collins-Fekete et al. [71]. This could be imagined since the WEPL of each image pixel is calculated as a weighted mean over all protons crossing into the pixel column through the object. The investigated spot spacing were set to 0.5, 1 and 2 times the lateral FWHM of the beam. Additionally, for the 7 mm beam, a spot spacing of only 1 mm was investigated.

Spot scanning

Spot scanning was emulated using the built in TPS source available in GATE [93], albeit some changes to the source code was performed to better control the spot weight and identifying the proton beams without the need for additional beam monitoring. By changing the source code and setting the appropriate flags controlling the behavior of the beam scanning, as detailed in section A.1, the pencil beam scanning described in this section is made available. The number of protons in each spot was influenced by the total number of protons used to reconstruct both a pRad and pCT projection of the paediatric head phantom. In the pRad of the head phantom, 10.5 million protons were homogeneously spread over a $180 \times 180\,\mathrm{mm}^2$ area covering the entirety of the head phantom. Similarly, 3.5 million protons were simulated in a single pCT projection when scanning the same head phantom. These numbers are in line with the amount used in other studies that have investigated reconstructed pRad [71] and pCT of a head

Table 3.2: Number of protons in each spot for the respective pencil beam and spot-spacing. The amount is based on covering a $180\times180\text{mm}^2$ area with 10 M protons in pRad and 3.5 M protons in a single pCT projection.

Spot weights			
	3 mm FWHM beam	**7 mm FWHM beam**	
Spot spacing	pRad	pRad	pCT
1 mm	NA	300	NA
0.5 FWHM	853	3698	NA
1 FWHM	3420	15000	5000
2 FWHM	13333	59170	NA

phantom [79, 94]. These two numbers were then used as a foundation to determine the general spot weight settings and was designed to stay consistent across all pRad and pCT simulations. E.g. for the 7 mm FWHM pencil beam and 1 FWHM spot spacing, 700 spots are needed to cover the $180\times180\,\text{mm}^2$ head phantom area, this correspond to 15000 protons per spot in pRad (10.5 M protons divided by 700 spots), and 5000 protons per spot in pCT (3.5 M protons divided by 700 spots) for the given pencil beam and spot spacing. The exact number of protons in each spot for each investigated pencil beam and spot-spacing setting are listed in Table 3.2. Based on the image quality of pRad affected by spot spacing and pencil beam size to be presented later in section 5.2 of this thesis work, only the most contemporary relevant 7 mm FWHM pencil beam and 1 FWHM spot spacing setting was used for pCT simulations.

3.3 Phantoms

A total of six different phantom geometries were implemented in GATE to investigate the impact of proton imaging setups on image quality (single-sided versus double-sided), beam parameters, and realistic Bergen DTC prototype properties impact on image quality. The first three phantoms were based on a water box both with and without aluminium cube inserts designed to investigate the impact of beam spot-size, spot-spacing, and removal of the front tracker on the MLP and spatial resolution of insert edges. The last three phantoms, two of which are Catphan® (The Phantom Laboratory, Salem, New York, USA) phantom modules designed to investigate spatial resolution (CTP528 line pair module) and RSP accuracy (CTP404 module). The final phantom, a digitized paediatric head phantom based on the CIRS model HN715 (Norfolk, Virginia,

USA) was implemented as a clinically relevant case.

All six phantoms were placed such that their rotational center aligned with the isocentre of the GATE Cartesian coordinate system. A complete lists of all used material compositions, densities, and their reference RSP are listed in Table 3.3.

3.3.1 Water phantoms

The first phantom was a 200 mm×200 mm×200 mm homogeneous water block used to study the accuracy and impact the single- and double-sided proton imaging setups, and beam spot size have on the estimated MLP compared to the actual MC ground truth path of the protons.

The second water phantom was a 200 mm×200 mm×200 mm homogeneous water block containing a 20 mm×20 mm×20 mm aluminium cube insert placed in the very centre of this water block. This phantom was used to study the impact of spot-spacing and beam spot size on the spatial resolution of reconstructed pRad. The TPS spot scanning plan covered the central $40\times40\,mm^2$ area overlapping the aluminium insert with beam weights dictated by the investigated spot spacing from Table 3.2. This phantom will be referred to as *spot-phantom* in this thesis work.

The third phantom was a 200 mm ×200 mm×200 mm homogeneous water block where five 10 mm×10 mm×10 mm aluminium cube inserts were placed at five different depths (15 mm, 57.5 mm, 100 mm, 142.5 mm, 185 mm) inside. The cubes were slanted 5 degrees relative to the vertical image pixel direction to evaluate the MTF from the edge of the cubes. This phantom enables the investigation of spatial resolution as a function of object depth. The TPS spot scanning plan covered the central $80\times80\,mm^2$ area overlapping the aluminium inserts with beam weights dictated by the investigated spot spacing from Table 3.2. This phantom is depicted in Figure 3.1 and will be referred to as *step-phantom* throughout this thesis work.

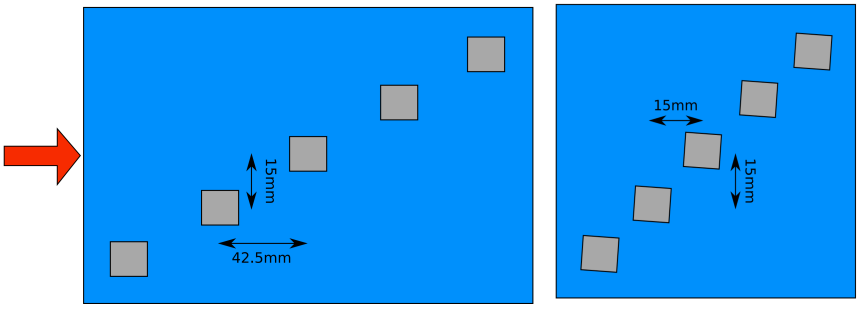

(a) Side-view of the step-phantom.

(b) Front/beam-view of the step-phantom.

Figure 3.1: Side (a) and front view (b) of the step-phantom. Five aluminium cubes of 10 mm edge length were slanted five degrees and placed at increasing depths inside a water tank. The red arrow represents the beam direction and black arrows mark the distances between the centres of the aluminium inserts.

3.3.2 Line pair module - (CTP528)

The fourth phantom was a Catphan® CTP528 phantom module (line pair) to be applied when investigating the spatial resolution of a full pCT scan. The phantom is an epoxy cylinder with height 40 mm and 150 mm diameter that contains small aluminium inserts at a fixed radial position with increasing spatial frequency (1–21 line pairs per cm – lp/cm), Figure 3.2. The CTP528 phantom area ($160 \times 40\,mm^2$) was covered with 168 beam spots and 5000 protons per spot (as dictated by the 7 mm FWHM beam and 1 FWHM spot spacing from Table 3.2).

3.3.3 Sensitometry module - (CTP404)

The fifth phantom was a Catphan® CTP404 phantom module (sensitom) used to assess the RSP accuracy of reconstructed pCT images. The phantom is made of an epoxy cylinder of 25 mm height, and 150 mm diameter, and contains 8 cylindrical cavities of 12.2 mm diameter, 6 of these cavities are filled with different plastic inserts, and two cavities with air. Exact materials are shown in Figure 3.3. The CTP404 phantom area ($160 \times 30\,mm^2$) was covered with 120 beam spots and 5000 protons per spot.

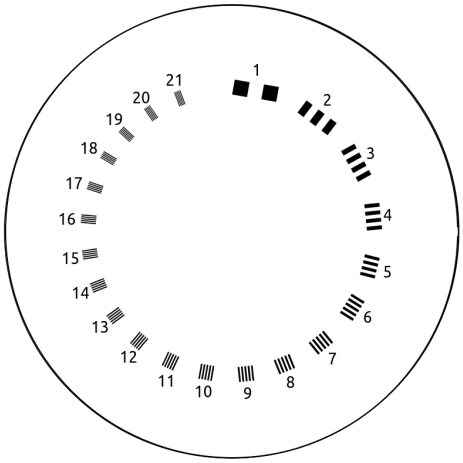

Figure 3.2: CTP528 line-pair module from Catphan® with numbered line pairs. Figure re-drawn from the Catphan® 412-424 Manual [95].

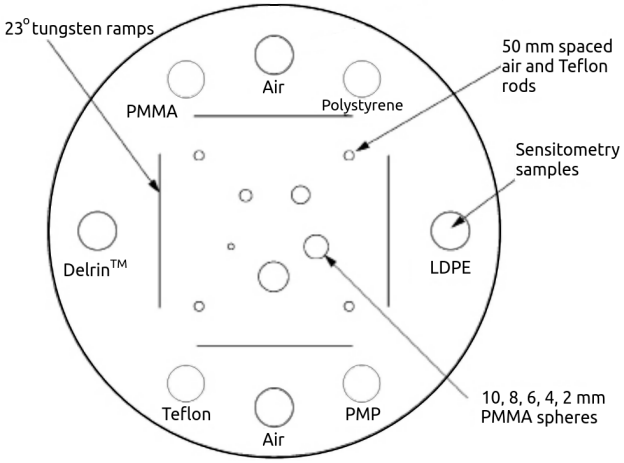

Figure 3.3: CTP404 sensitometry module from Catphan®. Figure re-drawn from the Catphan® 500-600 Manual [96].

3.3.4 Digitised paediatric head phantom

Finally, to represent a clinically relevant case, a digitised paediatric head phantom based on the CIRS model HN715 (Norfolk, Virginia, USA) was implemented in the simulations. The phantom is a high resolution (0.1875 mm×0.1875 mm×1.25 mm) voxelised geometry digitised by Giacometti et al. [97]. It consists of 8 different materials (including air) with known RSP listed at the end of Table 3.3. For illustration purposes, four

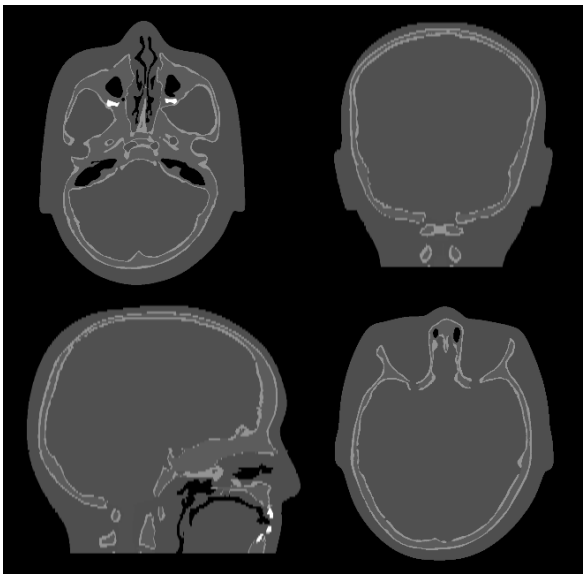

Figure 3.4: Four slices of the paediatric head phantom from its associated dicom files.

slices from the head phantom are shown in Figure 3.4.

3.4 Bergen DTC MC model

The DTC implemented in the MC simulation framework is a model of the system that is under construction by the Bergen pCT collaboration [19]. The detector is built to house the ALPIDE chips and distally form multiple sensitive layers that track the traversing particles through the detector until their range is reached and thus reconstructing the proton WEPL for use in pRad and pCT reconstruction. A figurative cross-section of the ALPIDE chip and associated flex board to be used in the DTC is seen in Figure 3.5a and details the thickness and material of its accompanying three Al/Pi foiled dielectric (FDI-A-50) components (chip-cable, top, and bottom) and kapton spacer [100]. The ALPIDE and its multilayered flexible communication board is glued unto rigid support structures where the sensitive area of the ALPIDE's will overlap to form a full sensitive plane as illustrated in Figure 3.5b [19]. The final detector will consist of 43 sensitive planes ensuring that 230 MeV protons will stop inside the DTC. The MC model used in this work has the same material budget as the planned detector, but all detector components and materials are approximated as slabs to eliminate the complicated overlapping

Material name	H	C	N	O	F	Mg	Al	Si	P	S	Cl	Ar	Ca	Ba	W	ρ [g/cm^3]	RSP
Air	-	0.01	75.53	23.18	-	-	-	-	-	-	1.28	-	-	-	-	0.00129	0.00114656
Water	-	11.19	-	88.81	-	-	-	-	-	-	-	-	-	-	-	1.00	1
Epoxy	7.80	71.09	2.03	19.08	-	-	-	-	-	-	-	-	-	-	-	1.16	1.14365
Aluminium	-	-	-	-	-	-	100.0	-	-	-	-	-	-	-	-	2.7	2.12406
Silicon	-	-	-	-	-	-	-	100.0	-	-	-	-	-	-	-	2.33	1.88539
LDPE	14.37	85.63	-	-	-	-	-	-	-	-	-	-	-	-	-	0.94	1.0036
Polystyrene	7.74	92.26	-	-	-	-	-	-	-	-	-	-	-	-	-	1.06	1.04783
PMMA	8.05	59.99	-	31.96	-	-	-	-	-	-	-	-	-	-	-	1.195	1.17918
PMP	14.4	85.6	-	-	-	-	-	-	-	-	-	-	-	-	-	0.83	0.886445
Delrin	6.71	40.0	-	53.29	-	-	-	-	-	-	-	-	-	-	-	1.41	1.36354
Teflon	-	24.02	-	-	75.98	-	-	-	-	-	-	-	-	-	-	2.2	1.83221
Tungsten Carbide	-	50.0	-	-	-	-	-	-	-	-	-	-	-	-	50.0	15.8	11.2536
CFRP	-	100.0	-	-	-	-	-	-	-	-	-	-	-	-	-	2.2	1.48386
Epoxy glue	7.09	76.03	-	16.88	-	-	-	-	-	-	-	-	-	-	-	1.05	1.02673
Kapton	2.64	69.11	7.33	20.92	-	-	-	-	-	-	-	-	-	-	-	1.42	1.31199
Soft tissue	8.48	57.45	1.65	24.6	-	7.62	-	-	-	-	0.19	-	-	-	-	1.055	1.04082
Brain tissue	8.17	53.62	1.53	26.51	-	9.98	-	-	-	-	0.19	-	-	-	-	1.07	1.04934
Spinal disk	7.07	52.46	2.11	27.60	-	9.55	-	-	-	-	0.21	-	0.98	-	-	1.10	1.06324
Trabecular bone	8.39	59.65	1.55	21.42	-	1.46	-	-	2.33	-	0.12	-	5.03	-	-	1.13	1.11132
Cortical bone	4.13	29.70	0.85	34.12	-	3.11	-	-	7.57	-	0.04	-	20.48	-	-	1.75	1.59108
Tooth dentin	4.51	35.35	1.23	29.41	-	-	-	-	9.20	0.08	0.04	-	19.84	0.33	-	1.66	1.51838
Tooth enamel	2.77	21.81	0.82	34.02	-	-	-	-	12.33	0.31	0.03	-	26.60	1.31	-	2.04	1.79506

Table 3.3: Atomic composition (fraction of mass in %), density and RSP of materials used in MC simulations. Atomic composition and density of compounds and elements were obtained from the GATE material database [98], the NIST compound database [99], and the underlying head phantom materials from Giacometti et al. [97].

structures. These DTC components include support plates functioning as energy absorbers (carbon fiber for the first two sensitive tracker layers, aluminium for the DTC interior), epoxy glue, ALPIDE (approximated as silicon) and its accompanying flex board. The first two layers, functioning as a tracker pair, differs from the main DTC body by consisting of two 200 μm Carbon Fibre Reinforced Polymer (CFRP) plates to reduce the material budget and scattering. The interior support plates are 3.5 mm thick aluminium plates spaced 2 mm apart and function as absorbers, together with the glued on ALPIDE and flex components they form one full detector layer. This interior detector layer is repeated a total of 41 times, amounting to a total length of 225.5 mm and ensuring that 230 MeV protons will come to a full stop inside the DTC. The total volume of the DTC is 270 mm$\times$165 mm$\times$225.5 mm. Figure 3.6 is a representation of the MC modelled detector and shows in more detail the slab thicknesses and materials. A complete lists of all used material compositions, densities as well as their RSP values are found in Table 3.3. No casings or structural support surrounding the outside of the detector was included in the proton imaging simulations since these have no impact on the proton interactions or WEPL reconstructions. This Bergen DTC MC model will hereafter be referred to as *DTC* in this thesis work.

3.5 WEPL estimation in Monte Carlo

The key proton property used to reconstruct pRad and pCT images for use in treatment planning is the proton WEPL through the imaged object. Two methods of extracting the WEPL information from a MC simulated proton is presented here, one ideal approach where the initial and residual energy is recorded on ideal detector planes before and after the imaged phantom, and a more realistic scenario where the WEPL is sampled from a Gaussian shaped distribution centered around the recorded ideal WEPL. This Gaussian distribution is based on the capability of the DTC prototype to accurately measure the proton WEPL and accounts for the systematic WEPL error and range straggling to be expected in the DTC.

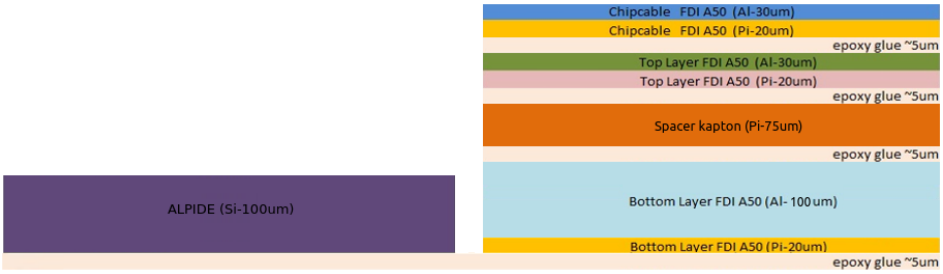

(a) Cross-section of the ALPIDE and flexible communication board components (material thicknesses are in parentheses). Figure re-drawn from Borshchov [100].

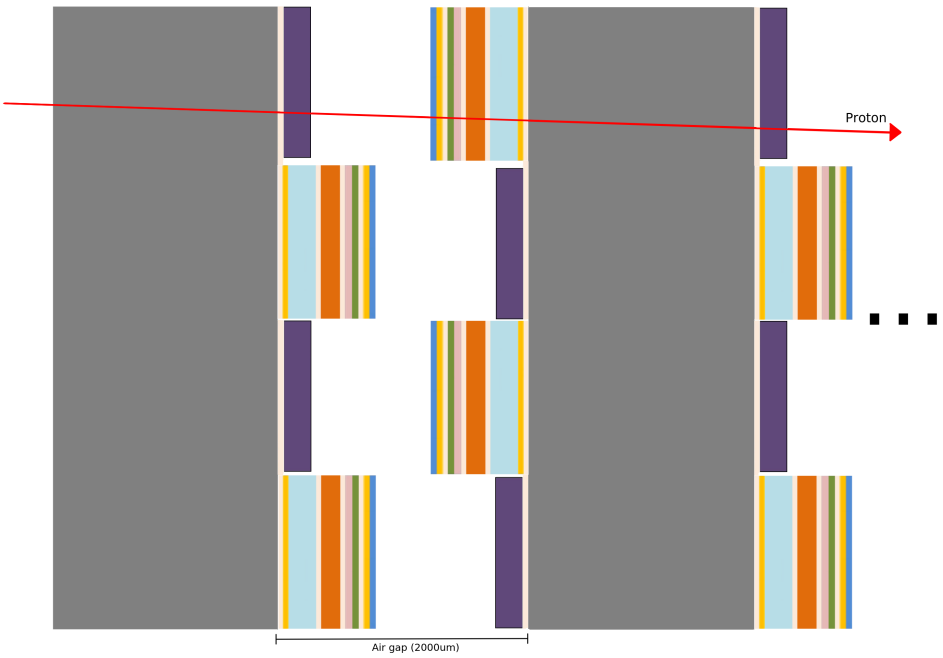

(b) Cross-section and sideways view of a single DTC layer with overlapping ALPIDE chips glued unto the aluminium absorbers.

Figure 3.5: Illustration of the ALPIDE and flexible communication board (a), and subsequent overlapping of ALPIDE and flex glued unto the aluminium absorbers forming a single sensitive layer (b).

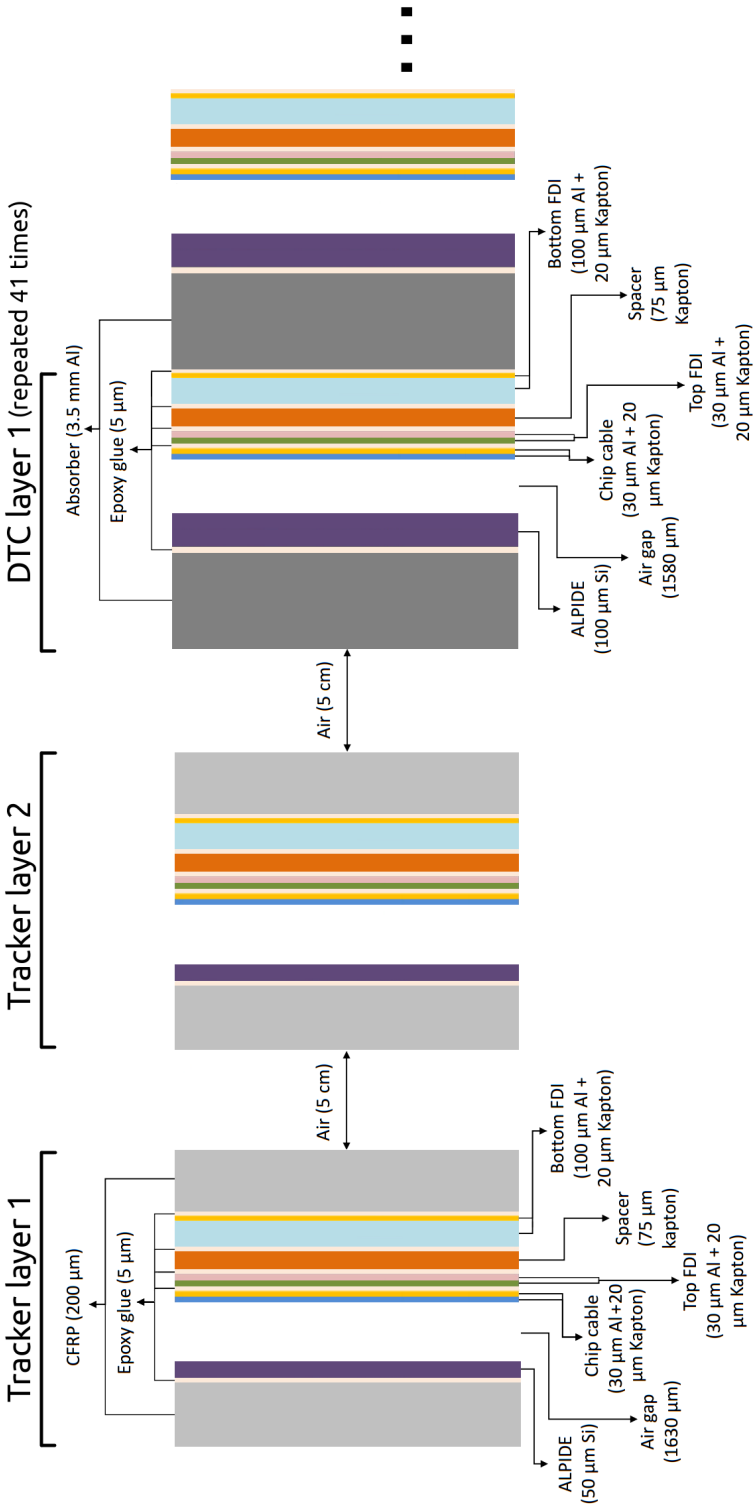

Figure 3.6: Detector geometry consisting of slabs approximating the final material budget of the Bergen pCT DTC as implemented in the MC framework.

3.5.1 Ideal WEPL estimation

Ideal tracker planes scored the initial energy (E_{in}) before and energy after (E_{out}) traversing the phantom to be imaged. This energy-loss was then converted to WEPL by integrating over the inverse stopping power in water,

$$\mathrm{WEPL} = \int_{E_{\mathrm{in}}}^{E_{\mathrm{out}}} \frac{1}{-\langle dE/dx \rangle_{water}} \mathrm{d}E \ . \tag{3.2}$$

The necessary stopping power table for water to integrate over was obtained directly from the GEANT4 code by calculating the stopping power in water at steps of 0.01 MeV for proton energy in the relevant energy range 70-300 MeV using the *GetTotalDEDX* function of the G4EmCalculator class in GEANT4.

3.5.2 Realistic WEPL estimation

A substantial analysis work-package designed by Pettersen et al. [84] includes a detailed description of the capabilities of the DTC prototype, including range/WEPL uncertainty of the protons traversing the DTC, and their inherent range straggling contributing to uncertainty in the range determination. This work-package includes charge diffusion considerations that activate multiple ALPIDE chip-pixels forming clusters when the ALPIDE is hit by a proton, thus identifying proton positions on the 41 sensitive layers for proton tracking considerations (efficiency) inside the DTC. An investigation of the DTC detailed in section 3.4 was performed to determine the systematic proton range uncertainty and range straggling in terms of WEPL for the DTC prototype, see Figure 3.7 for this dependency in relation to irradiated phantom thickness.

Thus, to extend the MC calculated ideal WEPL as detailed in subsection 3.5.1 to the more realistic $\mathrm{WEPL}_{\mathrm{DTC}}$ expected to be achievable with the DTC prototype, was determined by randomly sampling a Gaussian function with a mean value corresponding to the ideal WEPL shifted by the systematic uncertainty (proton range deviation in Figure 3.7), and standard deviation to the stochastic uncertainty (proton range straggling in Figure 3.7) expected for the DTC at the corresponding ideal WEPL. This $\mathrm{WEPL}_{\mathrm{DTC}}$ estimation disregards wrongly reconstructed proton tracks from potential tracking efficiency, future calibration efforts and effects, and overall efficiency of the DTC pro-

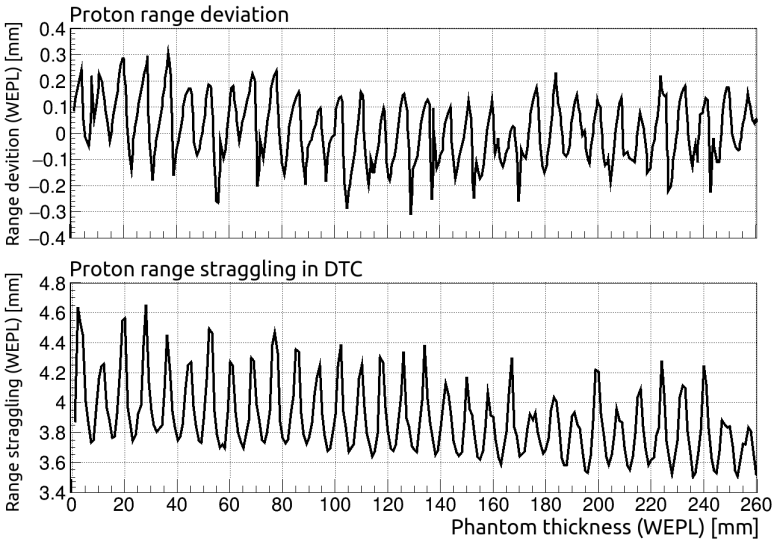

Figure 3.7: Basis for the theoretical limits of the DTC WEPL reconstruction. The systematic WEPL uncertainty and range straggling of protons after traversing phantom thicknesses ranging from 0 to 260 mm WEPL.

totype. The validity of this sampling approach was investigated in pRads of the head phantom and comparing the ideal double- and single-sided setup, the sampling of the WEPL_{DTC} (labelled *DTC (sampled)*), and a full MC simulation and analysis of the model detailed in section 3.4 using the work-package by Pettersen et al. [84] (labelled *DTC (analysed)*). The result of the WEPL error distribution (difference between reconstructed WEPL and the ground truth WEPL of the head phantom) from these four setups is presented in Figure 3.8. Given the comparable results between DTC (sampled) and DTC (analysed), the Gaussian sampling method described here is the preferred approach in this thesis work and is used when determining WEPL in all pRad and pCT images reconstructed and labelled *Bergen DTC*.

3.6 Discussing the reliability of the Monte Carlo simulations

The proof of concept by Pettersen [101] based on the ALPIDE-FoCal DTC prototype with MC simulations bench-marked with experimental data have proved that an ALPIDE-chip based DTC can be used for proton CT purposes with updated design cri-

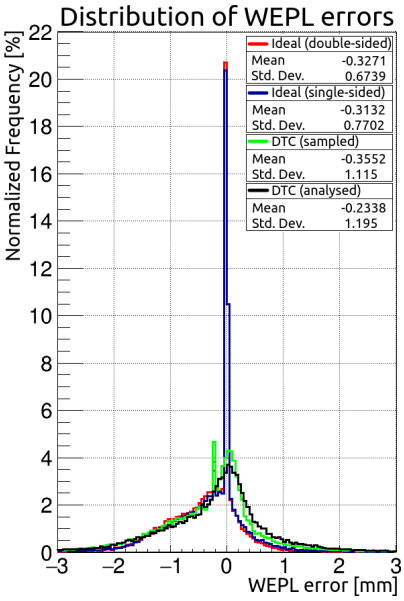

Figure 3.8: Distribution of WEPL error from pRad of the paediatric head phantom reconstructed from ideal MC data, and MC data based on the DTC MC model with both sampled, and analysed considerations. The mean and standard deviation of each WEPL error distribution is listed in the legend.

teria. These design criteria have been implemented in the updated MC model of the DTC.

The MC framework was built to ensure that the relevant simulation settings and accurate physics models for particle transportation in the clinical energy range were involved. The default settings in GATE and the physics-list QBBC_EMZ were deemed appropriate for the purposes of this work and are based on recommendations directly from the GATE collaboration and GEANT4 physics-list guide.

While this MC framework is designed to accurately model proton imaging setups, some simplifications have been made to accommodate accurate analysis and easier comparison of specific characteristics of the investigated imaging setups' impact on image quality. These simplifications are described and discussed in this section.

Proton beam source

The main proton pencil beam and source properties that emulate beam scanning in this work was based on a contemporary and clinical 7 mm FWHM pencil beam, but virtually any type of pencil beam is available in simulations by defining the appropriate

pencil beam properties, such as particle species, energy, divergent or convergent beam and the associated angular properties. These source definitions are available in GATE via the generic TPS beam scanning model by Grevillot et al. [93] and has been validated to achieve clinical performance and be usable for TPS bench-marking, making this TPS source model ideal for our investigations and simulations. Albeit, this model was modified slightly to allow for direct control of each pencil beam spot-weight, this was done to simplify the subsequent analysis of the proton events and readout from the simulations (for more details on the modified spot weight control, see section A.1). If the default stochastic spot-weight would have been used, additional beam delivery system monitoring of the pencil beams would have to be introduced in order to more easily identify the individual pencil beams. Any protons not adhering to the pencil beam in question, due to the stochastic spot-weighting, would be caught by the 3-sigma angular filter in later steps during image reconstruction, and so the impact from modifying the spot-weight in order to simplify the proton imaging simulation analysis is considered negligible. Secondary particles would similarly be identified by their angles and energy-loss (WEPL) after exiting the patient, including the DTC's capability as a continuous tracking device via the ALPIDE chip to identify secondaries by their topology, and so the explicit identification of the primary protons on the trackers is justified.

The second simplification in terms of the MC simulation settings is that no initial energy spread of the pencil beam is introduced. Energy spread is a beam delivery system and facility specific characteristic affecting the initial energy of the pencil beam. This choice aids us in focusing our investigations and observed image quality results in relation to the actual impact of changing the imaging setup (double-sided versus single-sided) without introducing TPS or facility dependent image noise. If energy spread was introduced in simulations, all protons would obtain a small stochastic error in their initial energy, effectively introducing RSP/WEPL uncertainties in images. This noise is expected to be limited due to the typically small energy spread from modern beam delivery systems, e.g. 0.3% at HIT [102]. This noise would also be reduced via WEPL filtering during the image reconstruction step. By removing this noise factor, the effect from the proton imaging setup modifications investigated in this thesis are more easily identified and analysed, justifying the removal of pencil beam energy spread.

The number of protons used in the pRad and pCT images was determined in relation

to the head phantom size and the amount of protons used in other studies. The amount of protons necessary for sufficient image quality is however a prospect for future studies and optimization efforts in the proton imaging field. The number of protons used in the pCT simulations in this work, 3.5 M protons in each projection and 360 projections in a 360 degree rotation in increments of 1 degree (amounting to 12.6×10^9 simulated protons), can be reduced without significant loss in image quality. However, this depends on the final efficiency of the prototype detector in question and the phantom size to be imaged. A significant amount of protons is expected to experience nuclear interactions as they traverse the DTC, and future tracking and calibration efforts will affect the final efficiency of the prototype leading to a loss of imaging protons used in reconstruction. Preliminary work-package analysis [84] of the DTC using the MC model detailed in this work and a performing a full pRad simulation of the head phantom encompassing MLP, WEPL reconstruction from the DTC, and pRad reconstruction has yielded a ~40% efficiency after all filtering and cuts in data processing had been performed [103]. This is a topic for discussion and improvement in the future when the DTC testing and calibration efforts are underway, and is outside the scope of this work.

The pRad simulation of the head phantom required about 7 CPU hours to complete on an Intel® Core™ i5-6300U CPU @ 2.40 GHz, and the complete full pCT simulation required approximately 852 CPU hours to complete on an Intel® Xeon(R) CPU E5-2620 v4 @ 2.10 GHz.

Geometry and phantoms

All applied material definitions involved in the MC simulations are detailed in Table 3.3 and most are based on the documentation following the phantom modules and the materials to be used in constructing the DTC. Some of the electrical components, particularly the metallic flex components connected to the ALPIDE and the sensitive detector layer of the ALPIDE are simplified to a single element, aluminium and silicon respectively. What is not included in the MC simulations is the overlapping nature between layers of ALPIDE as illustrated in Figure 3.5b to be present in the final DTC prototype. The final material budget of the DTC MC model is however defined as detailed and realistically as possible based on the design of the DTC at the time of writing. This ensures that the physics, energy-loss and scattering is modelled and accounted for in simulations

reflecting the WEPL/RSP reconstruction potential of the DTC prototype. An accurate material budget is particularly relevant for the tracker pair that induce scattering events directly affect the exit parameter vectors for use in MLP estimations and hull calculations.

WEPL estimation

The initial energy of the protons before entering the phantom is to be obtained from the beam delivery system, and as mentioned there is no energy spread present in the pencil beams, but the initial proton energy is obtained from an ideal phase-space plane located 15 cm before the phantom to be imaged. The residual energy is similarly obtained via a phase-space plane 15 cm downstream of the phantom, and the proton WEPL is calculated as described in section 3.5. For the DTC, where the residual energy is to be estimated by the detector itself, the WEPL_{DTC} is estimated based on the expected detector response from the DTC MC model. To simplify the DTC simulations and considerably reduce simulation time by excluding the full DTC model, except for the tracker pair, the calculated ideal WEPL is shifted by the systematic uncertainty of the detector response and undergoes a Gaussian sampling based on the inherent range straggling inside the DTC. These properties were extensively investigated using the MC model presented in section 3.4 and the pre-existing analysis tool from Pettersen et al. [84] and reported in Figure 3.7. This WEPL sampling is considered to reflect the results expected from the DTC. An investigation into the validity of the sampled WEPL model was however performed on the clinical head phantom where the reconstructed WEPL of every image pixel from the reconstructed pRad was compared with the ground truth WEPL in that pixel. Both the ideal WEPL measurement, the sampled WEPL, and the full WEPL measurement from the analysis work-package[84] was reconstructed and compared. A good agreement between the DTC (sampled) and DTC (analysed) WEPL error distribution was observed in Figure 3.8, with a difference in the standard deviation of only 0.08 mm, and the determination of the DTC WEPL through sampling was deemed to be a valid approach to estimating the DTC capabilities in this work. The difference is expected to come from confused proton tracks inside the DTC that assign a proton with a WEPL from a neighbouring proton, which will depend on the intensity of the incoming proton beam, efficiency of the tracking algorithm, and readout speed from the DTC and

subsequent data analysis of experimental data. This is a topic for future studies when the final version of the tracking algorithm and efficiency of the DTC is confirmed.

4. Radiation environment

Radiation has the potential to induce both temporary and permanent damage in modern digital circuits. Damaging effects that include displacement damage and total ionizing dose (TID) that are cumulative in nature and affect the lifetime of radiation sensitive electronics, and temporary radiation effects such as Single Event Effects (SEE) affecting the performance of exposed electronics. Field Programmable Gate Arrays (FPGAs) are particularly susceptible to SEE [104, 105]. The ALPIDE, while designed to be radiation hard, does have some radiation limits in terms of TID, and Non-Ionizing Energy Loss (NIEL) displacement damage.

This chapter investigates a proton imaging and proton therapy impact on the radiation environment inside a treatment room and relates the primary and secondary particle fluence and dose deposition to potential damages and expected lifetime of the most susceptible and exposed electronics used in the DTC. The sensitive electronics involve the ALPIDE detector chips and the chosen Xilinx® Kintex® UltraScale™ XCKU085-1FLVA1517C FPGA.

The radiation environment inside a treatment room where proton therapy and proton CT is performed is characterized by the primary protons and the secondary particles they produce when interacting with matter. The primary proton energy will affect the produced secondary particle properties. So a higher or lower initial proton energy together with varying the amount of traversed matter is expected to impact the radiation environment by potentially increasing or decreasing the amount, energy, and penetration depth of produced secondary particles. Such a change in the initial energy of primary protons and amount of traversed matter, is present in proton CT when compared to proton therapy. In proton therapy the initial primary proton energy is adapted to ensure the proton Bragg-peaks occur inside the intended TV inside the patient, whereas in proton imaging the protons are intended to pass completely trough the patient and are given a high initial energy to succeed in doing so (typically above 200 MeV). The number of primary particles involved is also different between therapy and imaging, whereas proton imaging require a number of primary protons in the order of 10^8 to reconstruct an image [106], proton therapy will typically require 10^{10} protons per Treatment Fraction

(TF) to deposit a prescribed dose to the TV. With proton imaging necessitating a detector system and readout electronics to be placed directly in the path of the beam exiting a patient, a high amount of radiation is expected to hit radiation sensitive electronics associated with the detector system during proton therapy.

4.1 Radiation damage on digital circuits

Single event upset

The radiation environment inside a particle therapy treatment room where mainly energetic hadrons are present means that Single Event Upsets (SEU) are of main concern when it comes to radiation effects affecting the performance of sensitive electronics (i.e. FPGAs). SEU occurs when a charged particle with enough energy to induce nuclear interactions in the silicon of a FPGA causes a charge disturbance in one of its memory cells and changes its contents, often referred to as a *bit-flip*. The number of SEU in a FPGA can be estimated using the following equation,

$$\#\mathrm{SEU} = \Phi_{\mathrm{HEH}} \times \sigma_{\mathrm{SEU}} \times \mathrm{C_M}\,. \tag{4.1}$$

Where Φ_{HEH} [cm^{-2}] is the fluence of high energy hadrons ($> 20\,\mathrm{MeV}$) incident on the FPGA, σ_{SEU} [cm^2/bit] is the SEU cross section of the affected FPGA, and $\mathrm{C_M}$ [bit] is the amount of configuration memory in the FPGA. Other single event effects can occur, but due to the resilience of modern FPGAs and especially the chosen Xilinx FPGA used in the DTC, these tend to be negligible [104].

Total ionizing dose and displacement effect

TID can over time generate defects in insulating layers and affect the performance of the device (e.g. shift in threshold voltage) causing irreversible damage and change operational settings. Displacement damage is caused by a particle energetic enough to cause an Non-Ionizing Energy Loss (NIEL) effect knocking an atom free from its lattice site, typically affecting semi-conductors by reducing their minority carrier lifetime [105, 107, 108].

4.2 FLUKA

The MC code FLUKA version 2011-3.0 in combination with Flair version 3.0-10 [30–32] was used to simulate a proton CT and proton therapy setting involving the DTC prototype. FLUKA is a useful computational tool when investigating a radiation environment in terms of secondary particle species, radiation damage to electronics, and radiation protection because many relevant quantities are readily available for scoring and analysis. Depending on the specific problem to be simulated, FLUKA activates relevant processes, options, and physics models through the use of FLUKA dubbed DEFAULTS that are analogue to GATE physics lists. The PRECISIO DEFAULT was chosen to simulate both proton CT and proton therapy settings due to its general application to precision simulations and relevant physics models for both proton therapy and proton imaging (for more details on the contents and options of all the applicable DEFAULTS, see the FLUKA manual [109]). The exact details and full FLUKA simulation setup via flair input files made for this thesis work and described in this section are available via the GitHub repository listed in section A.2.

Geometry set-up

A cylindrical and homogeneous water phantom with a radius of 80 mm and height of 240 mm was used to emulate a patient head, its center position was placed 230 mm from the first tracker plane (the phantom edge is thus located 150 mm distance from the innermost DTC tracker. The DTC model with its two tracker planes is modelled as presented in section 3.4 with some additional external Printed Circuits Boards (PCB) made of plastic approximating the readout boards attached to every second DTC layer on each side (as observed in Figure 2.4), and an aluminium block emulating the relevant support frame. All of these structures are illustrated in Figure 4.1a. The radiation environment is expected to be approximately symmetrical around the DTC and so only one side of the DTC is investigated to simplify and reduce simulation time. Additionally, six pure silicon blocks ($4 \times 4 \times 2\,\mathrm{cm}^3$) approximating as FPGAs are placed next to the DTC at increasing lateral distance (10 cm, 50 cm, 100 cm, 200 cm, 300 cm, and 400 cm) from the edge of the PCBs connected to the DTC. Figure 4.1b shows the locations of the first four FPGA objects in relation to the DTC.

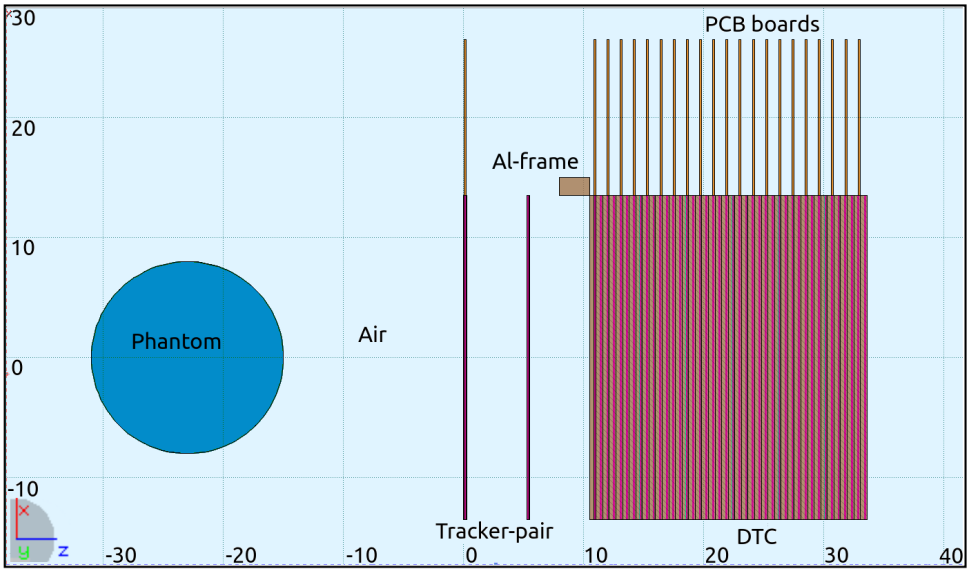

(a) The geometry set-up in FLUKA as viewed from the top-down (along the y-axis), the proton beam starts 50 cm downstream from the front-face of the first tracker placed at the iso-centre of the simulation world filled with air. The protons move along the z-axis and passes through the water phantom and air, before hitting the tracker pair and DTC. The PCB boards are 13.5 cm wide, 16 cm tall and 0.17 cm thick.

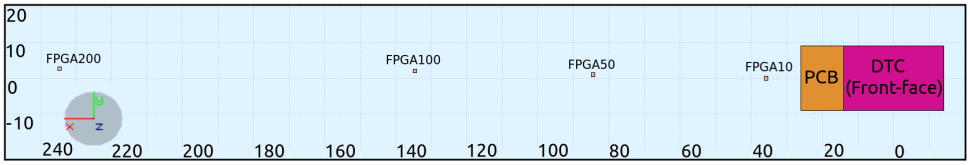

(b) Beam-eye view of the FLUKA geometry (along the z-axis). Only the first four nearest FPGA objects are visualized in this figure.

Figure 4.1: Overview of the FLUKA geometry set-up of a general proton imaging and proton therapy setting. The grid scale is in centimetre.

Scoring radiation damage with FLUKA

The FLUKA MC code allows the user to define sensitive scoring volumes dubbed USRBIN [110], these are Cartesian binning detectors divided into bins that are requested to score relevant quantities within. The explicit scoring quantities available in FLUKA that are of special interest concerning radiation environment and damage to electronics are:

- *DOSE*, the total dose deposited [Gy]. Related to the cumulative radiation damage effect, TID.

- *HADGT20M*, the fluence of hadrons with energy greater than 20 MeV [cm^{-2}]. Neutrons of lower energies are also included and weighted according to the ratio of their Single Event Upset (SEU) cross section to the one of > 20 MeV hadrons. This quantity is related to single event effects and scales with the rate of SEU as estimated by Equation 4.1.

- *SI1MEVNE*, silicon 1 MeV neutron equivalent fluence [cm^{-2}]. Related to the cumulative displacement damage effect scaling with the amount of NIEL that occur.

To score the relevant DOSE, HADGT20M, and SI1MEVNE quantities inside objects and volumes of interest, the following USRBIN volumetric meshes were defined and superimposed onto the objects in the simulations:

- Six individual USRBINs covering each of the six FPGA objects were applied for scoring DOSE.

- Each of the two DTC tracker layers were covered with a USRBIN with bin sizes $0.1 \times 0.1 \times 5 \cdot 10^{-4}\,cm^3$ tasked with scoring DOSE, HADGT20M, and SI1MEVNE.

- All remaining 41 layers of the DTC were covered with a single USRBIN consisting of bin sizes $0.25 \times 0.2 \times 0.025\,cm^3$ to score DOSE, HADGT20M, and SI1MEVNE inside the DTC.

- For scoring the HADGT20M and SI1MEVNE fluence outside the DTC and when entering the FPGA locations, a single $450 \times 6 \times 350\,cm^3$ USRBIN with bin sizes $1 \times 1 \times 1\,cm^3$ was defined to envelop the beam, DTC, and FPGA objects. This USRBIN covers the lateral (x-direction) positions starting from 0 cm to 450 cm, the depth (z-direction) positions -100 cm to 250 cm, inside a slice covering (y-direction) position -3 cm to 3 cm in height. (The exact area is represented in both Figure B.1 and Figure B.3.)

The results reported by FLUKA are inherently normalized to *per primary* (or *per primary proton* in the case of proton imaging and proton therapy simulations). These results can be manually scaled by the user with respect to the number of protons present during irradiation, given by an assumed or known beam rate or proton number involved in the simulated scenario. In this thesis work the normalized per primary results from

FLUKA will be reported and later extended in section 4.6 to make assumptions regarding the expected lifetime and radiation effects affecting the DTC and FPGAs.

4.3 Simulating radiation environment in proton CT

In pCT, where the primary protons have high initial energies to pass through the patient before penetrating and stopping inside a detector (e.g. 230 MeV), energetic secondary particles (e.g. secondary protons, neutrons, and photons) are expected to be produced in large numbers. Their high energy also make them capable of scattering and traversing over a wide area inside the treatment room. This gives rise to a radiation environment that necessitates radiation protection measures and requirements with respect to the radiation hardness of exposed equipment around the DTC, including the DTC itself. The majority of dose from primary protons is expected to be deposited at the end of the primary particle range, which in proton imaging is inside the DTC. Due to the relatively wide range of phantom thicknesses (e.g. 0–180 mm for a child's head) protons exiting the patient and entering the DTC will have a wide range of energies and thus different ranges inside the DTC and as a consequence spreading the dose distribution. In terms of secondary particle species, neutrons have high penetrative properties and can traverse considerable distances and through thick walls with their initial energy conserved from their initial creation vertex. Neutrons are expected to be produced in large numbers around the range of the primary protons inside the DTC, potentially causing damage to the ALPIDE themselves and also to escape the DTC and by this increase the neutron fluence inside the treatment room.

To emulate a proton imaging setting, a FLUKA provided user routine written in FORTRAN programming language was tailored to make FLUKA perform pencil beam spot scanning covering the water phantom and the front facing area of the DTC. The exact same 7 mm FWHM pencil beam properties as detailed in section 3.2 and used in GATE was reproduced in FLUKA. A total of 450 spot coordinates were defined to cover the positions from -8.4 cm to 8.4 cm in width and -6.0 cm to 6.0 cm in height on the first tracker front-face to cover the water phantom. The code from the written user source file controlling the beam scanning is found in section A.2. A total of 73135000 (73.135 M) protons were simulated in 65 cycles with 1125000 protons in each cycle, for

a total simulation run time of approximately 130 CPU hours (Intel® Core™ i5-6300U).

4.4 Simulating radiation environment in proton therapy

In state-of-the-art beam delivery systems the dose is delivered to the TV via horizontal and vertical scanning of proton pencil beams to achieve lateral coverage of the TV. The TV is to be covered longitudinally by the formation of a Spread Out Bragg Peak (SOBP) by overlapping multiple Bragg-peaks in succession. The SOBP was formed in the FLUKA simulations by editing and linking a FORTRAN user routine containing an energy distribution and a set of weights that are applied to the simulated primary particles forming a flat SOBP covering the TV longitudinally. The calculation tools created by Johnsen [111] was used for this purpose and the calculated energy distribution and weights for each of the beams are described by the following process:

The Bragg-Kleeman (BK) rule gives the relationship between range and energy of a particle in matter, Equation 1.6, repeated here for readability,

$$\mathcal{R} = \mathrm{a}\mathrm{E}_{\mathrm{in}}^{\mathrm{b}}\,.$$

where E_{in} is the initial energy of the particle, a and b are material and particle dependent constants. For protons in water, $\mathrm{a} = 2.633 \times 10^{-3}$ and $\mathrm{b} = 1.735$, these values were obtained from the work done by Zhang et al. [37], who fitted the BK rule to range curves and experimental data from proton, helium and carbon ions over a wide range of energies and materials. To create a SOBP spanning the desired range, i.e. 5 cm with maximum range 11 cm, several successive beams of sequential energies must be added together. The range of each of these contributing beams, r_k $(k = 1, 2, ..., n)$ are determined by the equation,

$$r_k = \left[1 - \left(1 - \frac{k}{n}\right)\chi\right] R_0\,, \tag{4.2}$$

where R_0 is the desired maximum depth, χ is the fraction of the maximum depth and width of the SOBP, and n is the number of energy intervals. By applying the ranges from Equation 4.2 to the BK rule section 4.4, the corresponding energy of each beam

(e_k) in the SOBP are obtained,

$$e_k = \left(\frac{r_k}{a}\right)^{\frac{1}{p_0}}. \tag{4.3}$$

In order to achieve a flat dose plateau in the SOBP, the individual proton beams must be weighted such that the proximal Bragg peak in the SOBP receives the lowest weight and the distal Bragg peak receives the highest. These beam weights, w_k are:

$$w_k = \begin{cases} 1-(1-\frac{1}{2n})^{1-\frac{1}{b}} & \text{for } k=0 \\ [1-\frac{1}{n}(k-\frac{1}{2})]^{1-\frac{1}{b}} - [1-\frac{1}{n}(k+\frac{1}{2})]^{1-\frac{1}{b}} & \text{for } k=1,...,n-1 \\ (\frac{1}{2n})^{1-\frac{1}{b}} & \text{for } k=n \end{cases}. \tag{4.4}$$

The parameter b will vary with energy, depth and width of the SOBP as seen in Johnsen [111], but the b value of 1.6 was empirically found to give a sufficiently flat SOBP plateau for the radiation environment investigations in this work.

The maximum proton range (R_0) of 11 cm, the desired SOBP width of 5 cm ($\chi = 11\,\text{cm}/5\,\text{cm}$) and 50 (n) equidistant beam energies were chosen and used in conjunction with Equation 4.2, 4.3, and 4.4 to find the necessary proton energy and corresponding weights to obtain this SOBP. The resulting proton energies spanned from 77.1 MeV to 115.9 MeV. The applied FLUKA user routine is found in section A.2 and lists the energies under the data block `DATA ENEDGE` (in GeV), and the weighting factors under `DATA CUMPR`. The user routine was further edited with initial particle coordinates constructed to fully cover the TV in the horizontal and vertical directions ($5\,\text{cm} \times 5\,\text{cm}$).

The resulting SOBP is seen in the depth dose profile in Figure 4.2. The flatness of the dose-plateau is considered to be sufficient for the investigations in question and the dose is scaled to an average treatment fraction (TF) delivering a physical dose of 2 Gy and requiring a total of $3.11 \cdot 10^{10}$ protons to achieve this. A total of 337.5 M protons were simulated in 300 cycles with 1125000 protons in each cycle and resulting in a simulation run time of approximately 96 CPU hours (Intel® Core™ i5-6300U).

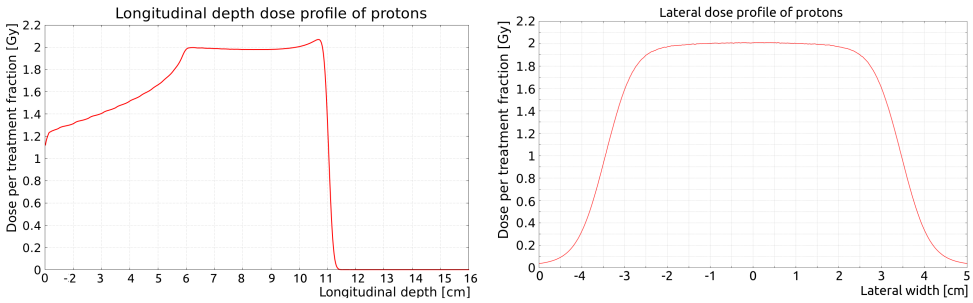

(a) (b)

Figure 4.2: Depth dose profile inside the water phantom. The dose plateau is covering the intended 6-11 cm range and the physical dose has been approximately normalised to 2 Gy in the dose plateau.

4.5 Radiation environment results

This section is divided into three subsections each reporting the scored HADGT20M fluence, SI1MEVNE fluence, and DOSE inside the USRBINs described in section 4.2.

4.5.1 Hadrons with energy greater than 20 MeV

The fluence of hadrons with energies greater than 20 MeV (HADGT20M) is related to SEU and are thus especially impactful on FPGAs that are sensitive to SEU. Overview maps of the HADGT20M fluence outside the DTC and at relevant positions for the placement of sensitive equipment during both pCT and proton therapy is seen in Figure B.1. The average HADGT20M fluence inside a smaller projection covering the last half of the DTC ranging from longitudinal position 20 cm to 32 cm, where the fluence is observed to be most abundant and approximately constant in relation to possible FPGA locations, is investigated. This average HADGT20M fluence is shown with respect to lateral distance from the center of the DTC in Figure 4.3. The peak observed for pCT, and the observed dip for proton therapy between 0 cm and 13.5 cm in this figure is due to the particle fluence appearing inside the DTC. The exact fluence per cm^2 scored on the six FPGAs positions are collected in Table 4.1 for readability.

HADGT20M fluence inside the DTC

The ALPIDE has its own SEU mitigation technique (Triple Modular Redundancy)

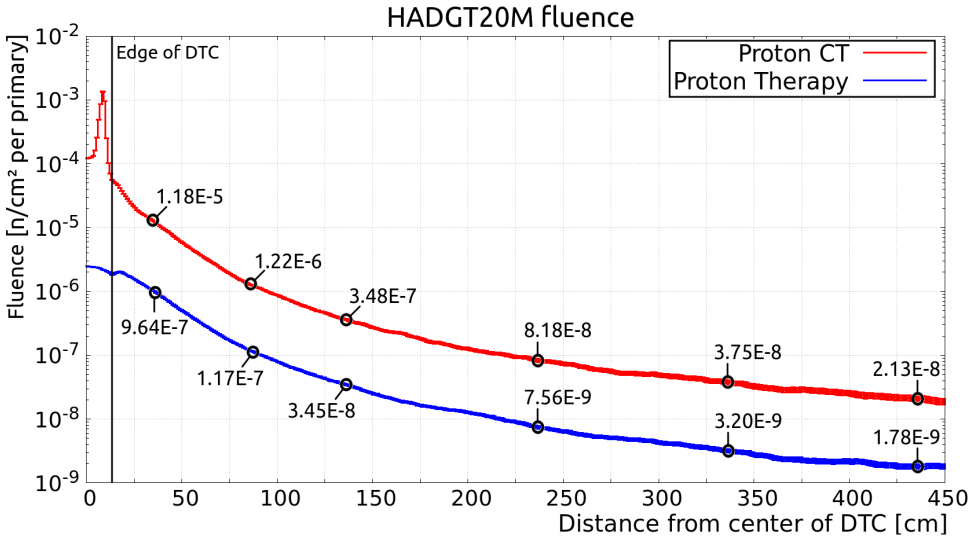

Figure 4.3: The average HADGT20M fluence with respect to distance from the center of DTC inside a projection of size 6 cm in height and 12 cm in width starting at longitudinal position 20 cm (covering the last half of the detector). The six investigated FPGA locations are marked and noted for readability. Error-bars are plotted and appear as a widening of the graph with increasing distance.

Table 4.1: Fluence of >20 MeV Hadrons per primary proton [cm^{-2}]. The corresponding error in percent is given in paranthesis.

Distance from DTC [cm]	Proton CT [cm^{-2}]	Proton therapy [cm^{-2}]
10	$1.18 \cdot 10^{-5}$ (0.3)	$9.64 \cdot 10^{-7}$ (0.7)
50	$1.22 \cdot 10^{-6}$ (1.1)	$1.17 \cdot 10^{-7}$ (1.9)
100	$3.48 \cdot 10^{-7}$ (1.8)	$3.45 \cdot 10^{-8}$ (3.8)
200	$8.18 \cdot 10^{-8}$ (3.8)	$7.56 \cdot 10^{-9}$ (8.0)
300	$3.75 \cdot 10^{-8}$ (6.0)	$3.20 \cdot 10^{-9}$ (11.4)
400	$2.13 \cdot 10^{-8}$ (8.0)	$1.78 \cdot 10^{-9}$ (14.8)

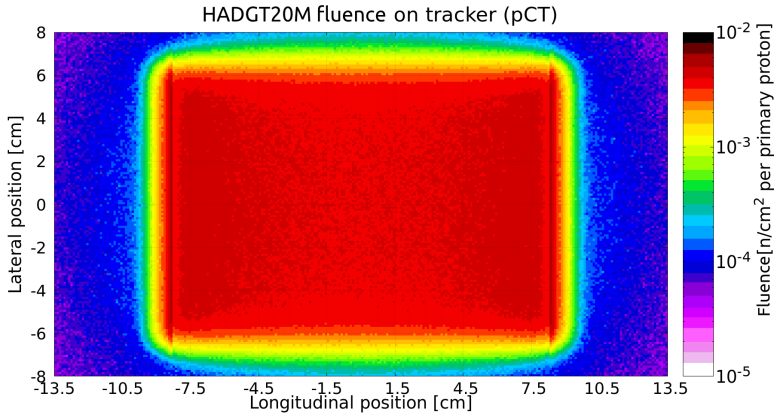

Figure 4.4: The average HADGT20M fluence on the front tracker. An increased HADGT20M fluence is seen along the vertical position at -8.4 cm and 8.4 cm. This corresponds to the spot positions just outside the edge of the phantom and contains mostly primary protons not affected by the phantom (approximating a beam-dump).

[112], and so the HADGT20M fluence is less relevant inside the DTC, nevertheless for the sake of insight into the fluence distribution of hadrons, the HADGT20M was scored inside the trackers and DTC. On the front tracker, Figure 4.4, and inside the DTC, Figure B.2, a maximum was observed at longitudinal position -8.4 cm and 8.4 cm, just to the left and right of the water phantom (upright cylinder with a radius of 8 cm), this coincides with the spot positions where the 7 mm FWHM pencil beams were aimed. Two separate profiles covering the central part of the DTC and this maximum edge through the DTC is shown in Figure 4.5. The DTC internal HADGT20M fluence for proton therapy is not shown as this is relatively homogeneously spread and the maximum occurs on the very first tracker. The maximum amount of particle fluence and dose deposition occurring during proton therapy is listed later in Table 4.4.

4.5.2 1MeV neutron equivalent fluence in silicon

The fluence of 1 MeV neutron equivalent in silicon (SI1MEVNE) is related to displacement effects (NIEL). Similarly as for HADGT20M, overview maps of the SI1MEVNE fluence outside the DTC and at relevant positions for the placement of sensitive FPGAs is found in Figure B.3. The average SI1MEVNE fluence inside a projection covering the last half of the DTC and with respect to lateral distance from the DTC is shown in Figure 4.6 and the fluence in the six FPGAs are collected in Table 4.2 for readability.

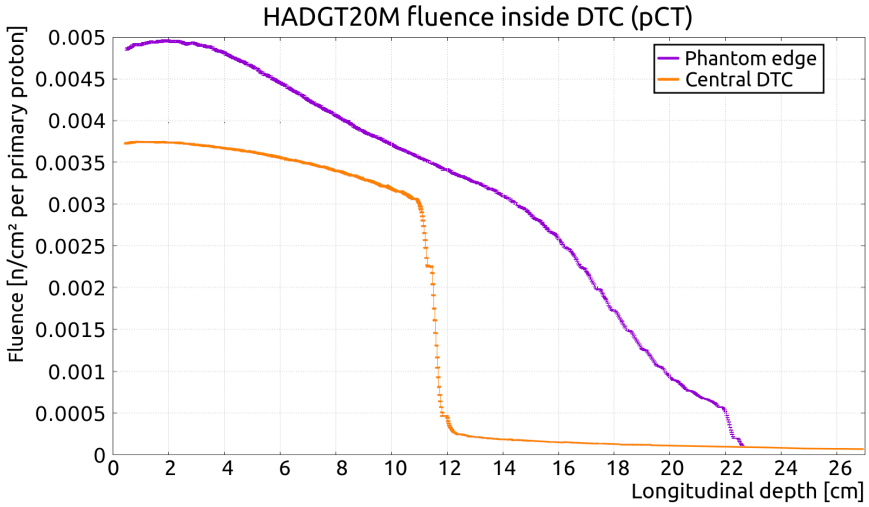

Figure 4.5: HADGT20M fluence profile both inside the central part of the DTC covered by a $1 \times 1\,\mathrm{cm}^2$ projection along the entire length of the DTC, and inside the observed maximum edge covered by a $0.5 \times 1\,\mathrm{cm}^2$ projection centered around longitudinal position -8.4 cm and spanning the entire length of the DTC. Error-bars are plotted, but appear too small to be seen.

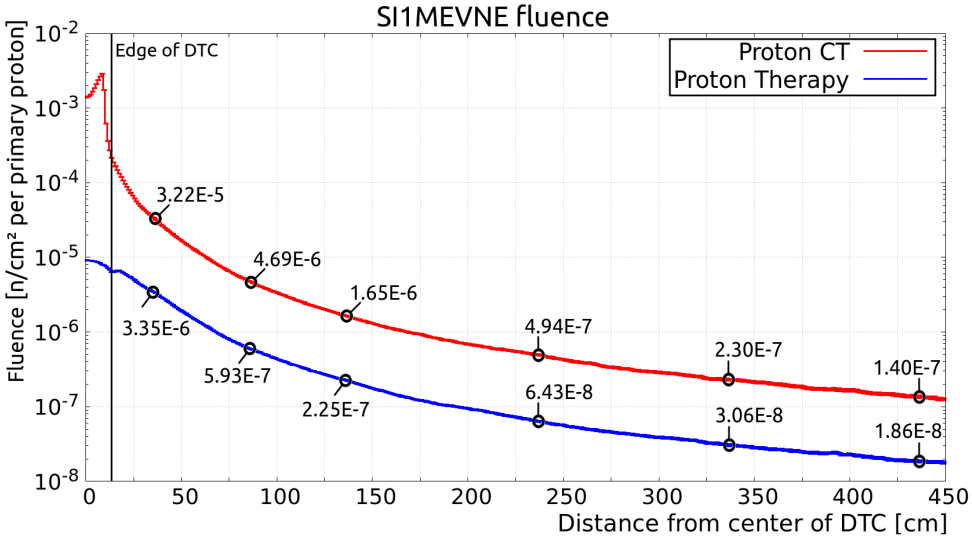

Figure 4.6: The average SI1MEVNE fluence with respect to distance from center of DTC inside a projection of size 6 cm in height and 12 cm in width starting at longitudinal position 20 cm (covering the last half of the detector). The six investigated FPGA locations are marked and noted for readability.

Table 4.2: 1 MeV neutron equivalent fluence per primary proton [cm^{-2}]. Error-bars are plotted, but appear too small to be seen.

Distance from DTC [cm]	Proton CT	Proton therapy
10	$3.22{\cdot}10^{-5}$ (0.3)	$3.35{\cdot}10^{-6}$ (0.4)
50	$4.69{\cdot}10^{-6}$ (0.5)	$5.93{\cdot}10^{-7}$ (0.7)
100	$1.65{\cdot}10^{-6}$ (1.3)	$2.25{\cdot}10^{-7}$ (1.5)
200	$4.94{\cdot}10^{-7}$ (2.5)	$6.43{\cdot}10^{-8}$ (2.9)
300	$2.30{\cdot}10^{-7}$ (3.6)	$3.06{\cdot}10^{-8}$ (4.2)
400	$1.40{\cdot}10^{-7}$ (4.8)	$1.86{\cdot}10^{-8}$ (5.4)

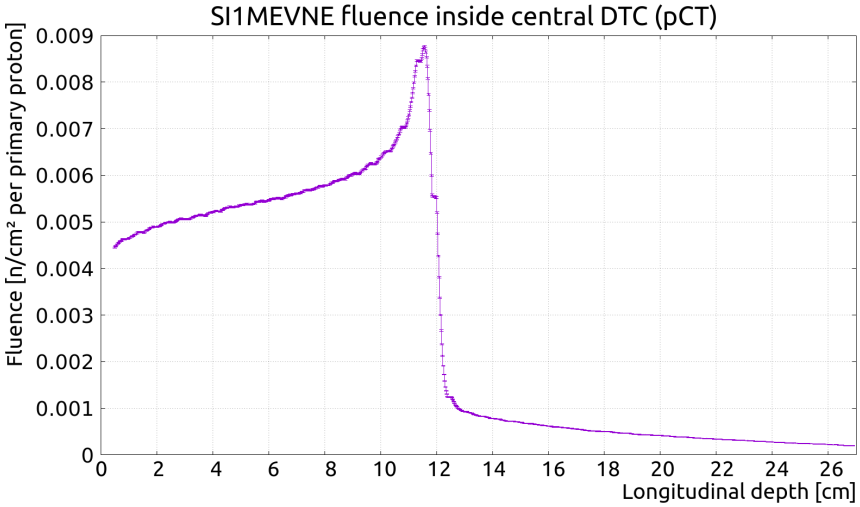

Figure 4.7: Average SI1MEVNE fluence depth profile inside a $2 \times 2\,cm^2$ projection going through the central part and along the total length of the DTC during pCT. Error-bars are plotted in the figure.

Neutron equivalent fluence inside the DTC

The fluence of SI1MEVNE inside the trackers and DTC is investigated due to the sensitivity of the ALPIDE in terms of its NIEL radiation limit [82]. In proton CT the highest amount of SI1MEVNE occur around the range of the protons inside the central part of the DTC as observed in Figure B.4a. A one dimensional depth profile through the central part of the DTC where the maximum occur is presented in Figure 4.7 and reveals the maximum amount of SI1MEVNE fluence inside the DTC. In proton therapy, see Figure B.4b, reveal that the first tracker experiences the highest fluence of neutron equivalent particles, this maximum value is listed later in Table 4.4.

Table 4.3: Deposited dose in Gy per primary proton to FPGA structures. The corresponding error in percent is given in parenthesis.

Distance from DTC [cm]	Proton CT [Gy/primary]	Proton therapy [Gy/primary]
10	$7.13{\cdot}10^{-15}$ (1.4)	$5.33{\cdot}10^{-17}$ (3.5)
50	$8.11{\cdot}10^{-16}$ (4.9)	$1.59{\cdot}10^{-17}$ (7.2)
100	$1.66{\cdot}10^{-16}$ (8.1)	$5.79{\cdot}10^{-18}$ (8.8)
200	$2.43{\cdot}10^{-17}$ (17.6)	$2.03{\cdot}10^{-18}$ (18.7)
300	$1.55{\cdot}10^{-17}$ (31.1)	$8.69{\cdot}10^{-19}$ (18.1)
400	$6.99{\cdot}10^{-18}$ (37.5)	$5.99{\cdot}10^{-19}$ (24.6)

Table 4.4: Peak values observed inside the DTC per primary proton, p. The maximum HADGT20M was observed at the edge of the phantom, maximum of SI1MEVNE around the range of the protons, and the maximum dose at the nominal Bragg peak location. Corresponding error in percent is given in parenthesis.

Maximum values inside the DTC		
	Proton CT	**Proton therapy**
Peak HADGT20M fluence [cm^{-2}/p]	$5.00{\cdot}10^{-3}$ (0.3)	$1.37{\cdot}10^{-5}$ (0.7)
Peak SI1MEVNE fluence [cm^{-2}/p]	$8.76{\cdot}10^{-3}$ (0.1)	$4.14{\cdot}10^{-5}$ (0.6)
Peak dose [Gy/p]	$9.35{\cdot}10^{-12}$ (0.4)	$8.51{\cdot}10^{-16}$ (10.0)

4.5.3 Total ionizing dose

The total deposited dose in Gray (Gy) per primary was scored inside each of the six FPGA structures and the results are listed in Table 4.3.

Total ionizing dose inside the DTC

The dose deposition inside the DTC during pCT is shown in Figure 4.8a and a depth-dose profile of the maximum dose observed inside the central part of the DTC is shown in Figure 4.8b revealing the Bragg peak. The maximum dose in the Bragg peak during pCT, and the maximum dose deposited in proton therapy (occurring inside the first tracker) is listed in Table 4.4, along with the observed maximum HADGT20M and SI1MEVNE values inside the DTC during pCT and proton therapy.

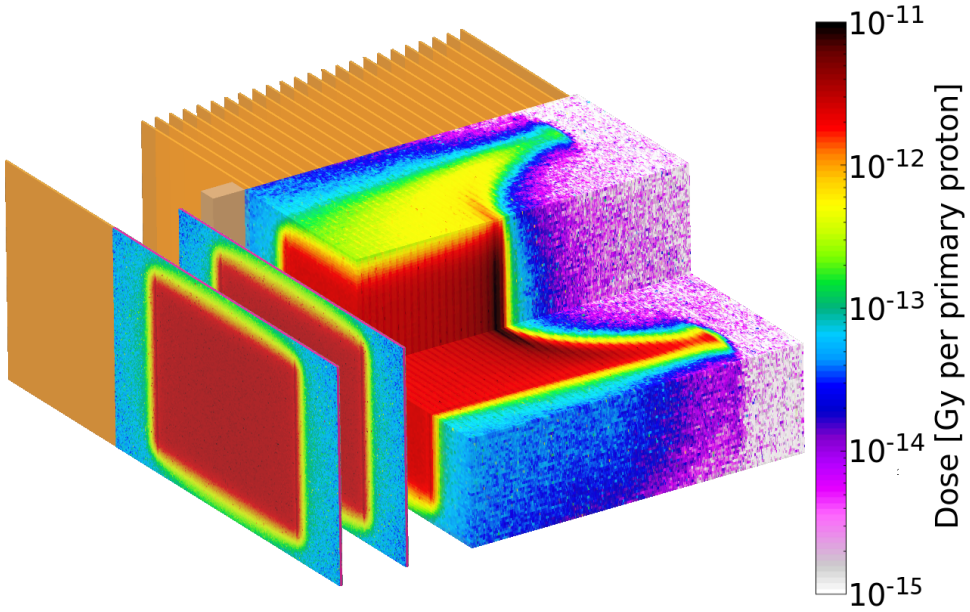

(a) Dose (Gy per primary) deposited inside the DTC from proton CT.

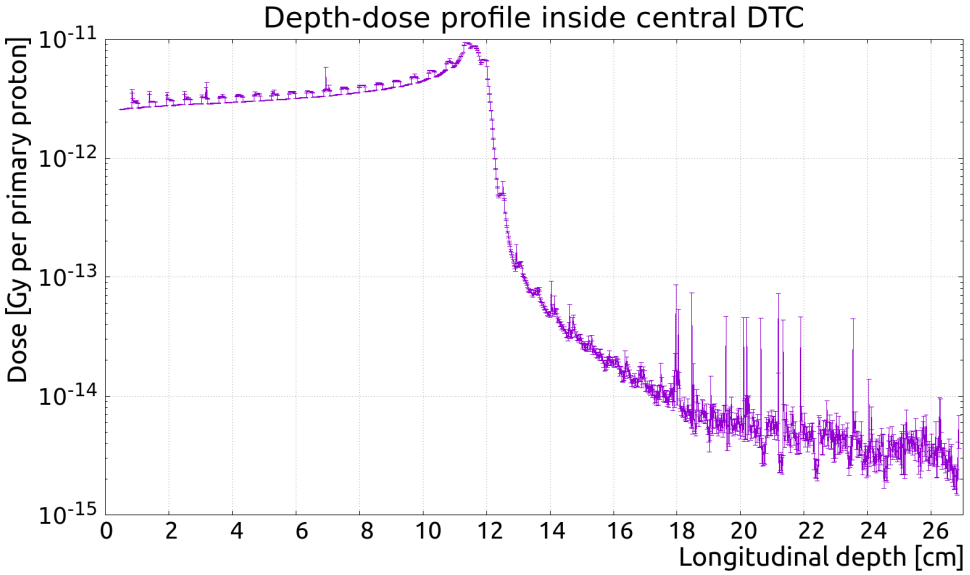

(b) Depth dose profile per primary proton inside a $1\,\mathrm{cm}^2$ projection covering the central part of the DTC. The "sawtooth" structure observed is due to the material differences involved in the DTC design described in section 3.4.

Figure 4.8: Deposited dose (Gy) inside the DTC from proton CT.

4.6 Discussion of the FLUKA simulated radiation environment and expected radiation effects in sensitive electronics

FLUKA simulated radiation environment

FLUKA simulations of the radiation environment surrounding the DTC has given insight into the overall radiation levels that the electronics is expected to be exposed to during a pCT and proton therapy. The irradiation settings described in section 4.3 were modelled based upon what can be expected during proton imaging with the DTC, as given by the energy and spot-positions covering the front face of the DTC (-8.4 cm to 8.4 cm horizontally and -6 cm to 6 cm vertically). In proton therapy, section 4.4, the chosen $5 \times 5 \times 5\,\mathrm{cm}^3$ TV inside a cylindrical water phantom and 2 Gy physical dose was based on a suggestion from personal communications with experienced medical physicists. However, there are a range of factors that will affect the overall radiation environments in pCT and proton therapy, including a patient geometry that does not require symmetrical radiation fields, or a tumor placement, size, and fractionation scheme that will affect the amount of primary protons in a proton therapy treatment. The bin-sizes of the FLUKA USRBINs can also affect the results by reporting a lower average if the USRBIN bin-size is too large and does not contain a relatively constant fluence or dose due to variation in material or impinging fluence inside each bin. The bin-sizes used in the FLUKA simulations have been investigated with preliminary simulation settings that applied smaller bins testing the effect of bin-size inside the FPGA objects, due to the relatively constant fluence impinging on the FPGA objects, the chosen bin size did not affect the average results beyond the reported errors. Inside the DTC the bin-sizes can have an affect due to the small thickness of the layer materials (e.g. $5\mu m$ of glue) that make several materials fit inside the same bin and affecting the average dose deposition. The DTC bin-size thickness of 0.025 cm is fine enough bring out the *saw-tooth* effect observed in the depth dose profile inside the DTC in Figure 4.8b. Between the saw-tooth spikes the dose deposition in the aluminium absorber is seen and the spikes themselves contain the dose deposited in the ALPIDE and accompanying flex materials. The high error associated with the DOSE deposited in the FPGAs at large distances, particularly

those further than 200 cm away from the edge of the DTC, points to the relatively small amount of dose deposited at these distances, as expected from the inverse-square law detailing the decrease in dose with distance from the source ($1/\text{distance}^2$).

For these reasons, in the discussion of the radiation environment in this section, the results from the FLUKA simulations will be multiplied with a safety factor of 10. This safety factor is intended to account for geometrical simplifications in the simulations, i.e. no cables or PCBs around the FPGAs, the overall bin-sizes of the USRBINs affecting average results, and for the varying amount of protons involved in a pCT or proton therapy session.

Expected radiation effects and lifetime of the DTC

By combining the FLUKA calculated secondary particle fluences and dose *per primary proton* inside the FPGAs, presented in Table 4.1 for HADGT20M, Table 4.2 for SI1MEVNE, and Table 4.3 for the DOSE, including the maximum values found inside the DTC listed in Table 4.4, with known or assumed proton rates and radiation hardness limits of the involved electronics, it becomes possible to estimate the radiation effects and lifetime of the DTC.

Given by the design goal of the DTC, a proton rate of 10 M protons per second is assumed during pCT. In proton therapy, based on a treatment fraction delivering a physical dose of 2 Gy inside the 5 cm×5 cm×5 cm TV (requiring 3.11×10^{10} protons) in a 100 second time window, an average proton rate of 311 M protons per second is assumed. This will scale the FLUKA scored secondary particle fluence and dose in terms of *per second*. The scaled HADGT20M, SI1MEVNE, and DOSE values are listed in Table 4.5 for the six FPGA distances and the maximum values observed inside the DTC relating to the ALPIDE.

Combining the scaled fluence and dose results from Table 4.5 with the known radiation-hardness limits and SEU cross section of the FPGA, and the radiation limits of the ALPIDE, the radiation effects and lifetime of the DTC can be estimated. The expected number of SEU in the FPGAs can be estimated by using the HADGT20M fluence results from Table 4.5 in combination with Equation 4.1, where the configuration memory is $512 \cdot 10^6$ bit and the SEU cross section is $1.89 \cdot 10^{-15}$ [cm^2/bit] for the Xilinx Ultrascale FPGA [113]. As every single of the 43 readout unit boards connected to the

Table 4.5: The HADGT20M fluence, SI1MEVNE fluence, and dose per second in pCT and proton therapy (pT) in the FPGAs, and maximum values in the ALPIDE. The total dose is calculated with both pCT and pT combined as the DTC is expected to be present during proton therapy. The safety factor of 10 is included. The corresponding error in percent is given in parenthesis.

FPGA			
		pCT	**pT**
HADGT20M	Dist. from DTC [cm]	Fluence [cm^{-2}/s]	Fluence [cm^{-2}/s]
	10	1180 (0.3)	2998 (0.7)
	50	122 (1.1)	363.9 (1.9)
	100	34.8 (1.8)	107.3 (3.8)
	200	8.18 (3.8)	23.5 (8.0)
	300	3.75 (6.0)	9.95 (11.4)
	400	2.13 (8.0)	5.54 (14.8)
SI1MEVNE	10	3220 (0.3)	10419 (0.4)
	50	469 (0.5)	1844.2 (0.7)
	100	165 (1.3)	699.8 (1.5)
	200	49.4 (2.5)	200.0 (2.9)
	300	23.0 (3.6)	95.2 (4.2)
	400	14.0 (4.8)	57.8 (5.4)
DOSE		**pCT**	**pCT+pT**
	Dist. from DTC [cm]	Dose [Gy /s]	Dose [Gy /s]
	10	$7.13{\cdot}10^{-7}$ (1.4)	$8.79{\cdot}10^{-7}$ (3.5)
	50	$8.11{\cdot}10^{-8}$ (4.9)	$1.31{\cdot}10^{-7}$ (7.2)
	100	$1.66{\cdot}10^{-8}$ (8.1)	$3.46{\cdot}10^{-8}$ (8.8)
	200	$2.43{\cdot}10^{-9}$ (17.6)	$8.74{\cdot}10^{-9}$ (18.7)
	300	$1.55{\cdot}10^{-9}$ (31.1)	$4.25{\cdot}10^{-9}$ (18.1)
	400	$6.99{\cdot}10^{-10}$ (37.5)	$2.56{\cdot}10^{-9}$ (24.6)
ALPIDE			
		pCT	**pT**
Max. values	Dose	$9.35{\cdot}10^{-4}$ (0.4) [Gy /s]	$2.65{\cdot}10^{-6}$ (10.0) [Gy /s]
	SI1MEVNE	876000 (0.1) [cm^{-2}/s]	12875.4 (0.6) [cm^{-2}/s]
	HADGT20M	500000 (0.3) [cm^{-2}/s]	4260.7 (0.7) [cm^{-2}/s]

DTC layers will contain a FPGA and are exposed to radiation (all 43 FPGAs are here assumed to be exposed to the same amount of radiation as the simulated FPGA objects), the number of SEU expected is given for the entire system. The time it takes to observe the first occurrence of SEU in this 43 FPGA system is listed in Table 4.6. Included in this table is the expected time until the FPGA reaches a conservative 100 Gy TID limit.

The expected time until the ALPIDE reaches its TID and NIEL design requirement limits of 27000 Gy and $1.7 \cdot 10^{13}$ [$1\,\mathrm{MeV n_{eq}/cm^2}$] respectively [82] are also listed in Table 4.6. It is noted that these ALPIDE design limits have been observed to be exceeded in real-life without severe damage to its operations [114]. The maximum values in Table 4.6 assume that the maximum occurs at the same position at all times, this is not necessarily true in real-life as either the patient, or the gantry and DTC, will rotate and thus shift the position of the Bragg peak inside the DTC depending on the changing thickness and type of patient tissue traversed. However, when considering the location of the maximum to be fixed, a worst-case scenario is expected and is considered a valid approach in radiation protection or radiation damage estimations.

Based on the results collected in Table 4.6, the first expected SEU at a distance of larger than 100 cm will likely occur after 690 seconds and this is within tolerable limits that can be handled with simple off-the-shelf mitigation techniques. Given the conservative TID-limit of 100 Gy for the FPGAs, the FPGAs can be considered radiation hard enough to outlast the ALPIDE. In terms of the lifetime of the DTC, the ALPIDE will not reach their TID limit before after $2.88 \cdot 10^7$ seconds (0.91 years), or reach their NIEL radiation hardness limit before after $1.91 \cdot 10^7$ seconds (0.61 years) of constant proton CT and proton therapy irradiation. By making assumptions based on a pCT scan time of 56 s (assuming 560 M protons are enough for imaging with the DTC) and an average treatment time of 100 s where irradiation occurs, the DTC prototype can be expected to be used to image a total of 122436 patients before reaching the NIEL design limit of the ALPIDE. If one also assumes that a proton therapy facility treats 15 patients a day 250 days per year, it will take 32.6 years before the DTC is expected to show an impact in its operating efficiency.

Thus, given the assumed proton intensity, and inclusion of a safety factor of ten accounting for potential inaccuracies due to simplifications and assumptions in simulations, the proton CT and proton therapy radiation environment is not expected to

Table 4.6: Expected FPGA and ALPIDE health and life-time from being exposed in both proton CT and proton therapy. All 43 FPGA are considered as a single system and the time it takes for a single SEU to occur is estimated (1 SEU). A conservative TID limit of 100 Gy for the FPGA is used. The ALPIDE design limits are 27000 Gy and $1.7 \cdot 10^{13}\,1\,\mathrm{MeV n_{eq}/cm^2}$ for TID and NIEL limits respectively [82].

FPGA			
		Proton CT	**Proton therapy**
1 SEU	Dist. from DTC [cm]	Time [s]	Time [s]
	10	20.4	8.0
	50	196.9	66.2
	100	689.7	224.7
	200	2941.2	1022.5
	300	6410.3	2415.5
	400	11286.7	4347.8
DOSE (TID)		**Proton CT**	**pCT + pT**
	Dist. from DTC [cm]	Life-time [s]	Life-time [s]
	10	$1.40 \cdot 10^8$	$1.14 \cdot 10^8$
	50	$1.23 \cdot 10^9$	$7.63 \cdot 10^8$
	100	$6.02 \cdot 10^9$	$2.89 \cdot 10^9$
	200	$4.12 \cdot 10^{10}$	$1.14 \cdot 10^{10}$
	300	$6.45 \cdot 10^{10}$	$2.35 \cdot 10^{10}$
	400	$1.43 \cdot 10^{11}$	$3.91 \cdot 10^{10}$
ALPIDE			
		Proton CT	**pCT + pT**
Maximum values	Dose (TID)	$2.89 \cdot 10^7$ [s]	$2.88 \cdot 10^7$ [s]
	NIEL limit	$1.94 \cdot 10^7$ [s]	$1.91 \cdot 10^7$ [s]

induce any critical radiation damage or otherwise considerably limit the lifetime of neither the DTC or FPGAs when the FPGAs are located 100 cm or more from the DTC. However, the amount of protons needed to perform a full proton CT image in a clinical environment has not been optimized in experimental studies, and the amount of protons involved during proton therapy can vary considerably depending on the tumor site and size of the TV. The inclusion of a safety factor of 10 is intended to limit the impact of the assumptions made in regards to the proton intensity, and the results with this safety factor included show that the radiation environment is still within tolerable limits and the DTC proton imaging system will likely survive inside a clinical radiation environment for as long as the proton therapy facility itself is operational (typically 30 years).

It is noteworthy that other assumptions concerning the safety factor and/or proton intensity is possible to include by scaling the presented *per primary proton* results in Table 4.1 (HADGT20M), Table 4.2 (SI1MEVNE), Table 4.3 (DOSE), and Table 4.4 (maximums inside the DTC) with their own safety factor or proton rates.

5. Reconstruction precision in single-sided proton imaging

This chapter uses the MLP and reconstruction tools detailed in chapter 2 and the developed MC simulations framework described in chapter 3 to investigate the impact on reconstruction precision (MLP accuracy, spatial resolution and RSP accuracy) when removing the front tracker pair. The effects of spot-spacing and pencil beam spot-size in a single-sided setup was also investigated in conjunction with ideal trackers, including evaluation of the expected image quality from the DTC currently under construction by the Bergen pCT collaboration.

5.1 Impact of a single-sided imaging setup on most likely path

A single-sided imaging setup will negatively affect the MLP estimation due to the increased position uncertainty of the protons incident on the phantom [56][1]. However, the work by Krah et al. [56] focused on the accuracy of the MLP without reconstructed images. In this section, the impact on MLP estimations when removing the front tracker is investigated inside a 20 cm water phantom, and the overall impact on image quality will be investigated later in this chapter.

Prior to the existence of the extended-MLP formalism by Krah et al. [56], an initial assumption of the proton entrance position obtained directly from the mean TPS spot positions and applied to the MLP formalism by Schulte et al. [60] was investigated in the 20 cm thick water phantom and the spot-phantom described in section 3.3. Figure 5.1 show the quality of the MLP estimations compared to the ground-truth MC path of the protons using the 7 mm and 3 mm FWHM pencil beams in a single-sided setup with ideal trackers and the homogeneous water phantom. Both the MLP estima-

[1] While in their work, Krah et al. do not directly consider a single-sided imaging setup where the direction of exiting protons is considered, but it is straightforward to apply their methodology to such a case as well.

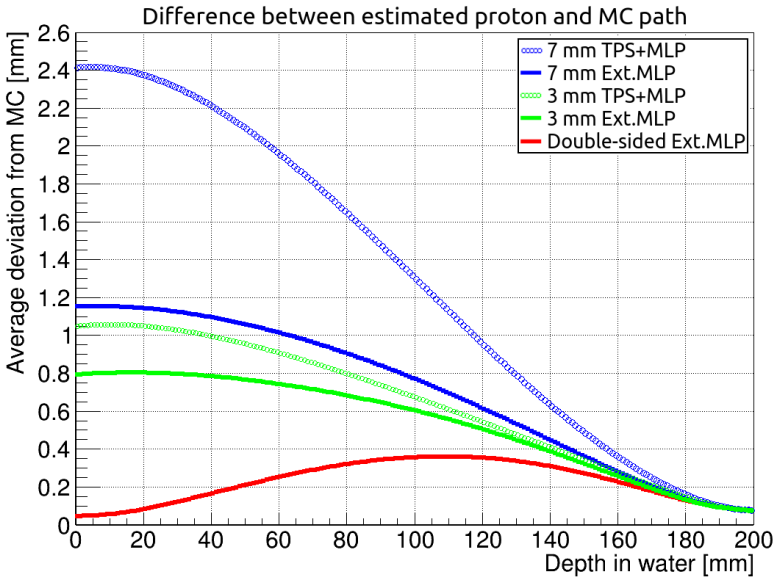

Figure 5.1: The average deviation of the MLP path from the MC ground truth path. The blue curves denote the 7 mm FWHM beam and the green curves the 3 mm FWHM beam: Dotted curves depict TPS mean position and direction input used directly in MLP, full curves refers to the extended-MLP formalism taking the incoming pencil beam uncertainties into account. The red curve is the MLP estimation in an ideal double-sided setup.

tions with initial proton TPS beam spot position and pencil beam angle as input, and the extended-MLP estimation based on the TPS input and included pencil beam uncertainties (spot size and beam divergence) are compared in the same figure. Including comparison with the double-sided imaging setup not dependent on the physical pencil beam properties or TPS settings. Comparing the ideal tracker setups to more realistic imaging setups where the trackers have a position resolution and material budget that induce scattering and negatively affecting MLP was done in Figure 5.2. Here, a SSD-based pCT setup inspired by the existing prototype Loma Linda phase II double-sided setup [106] was used as an example of a realistic setup. These trackers were each approximated as 0.4 mm thick silicon blocks to account for their material budgets, and a position resolution of 155 μm. The impact of the DTC trackers (detailed in section 3.4) on the MLP was also investigated and compared to the Loma Linda phase II inspired setup if their front tracker pair were to be removed to form an equivalent single-sided setup. Only the 7 mm FWHM pencil beam consisting of 230 MeV protons traversing the 20 cm thick water phantom was investigated in this comparison. Due to the dis-

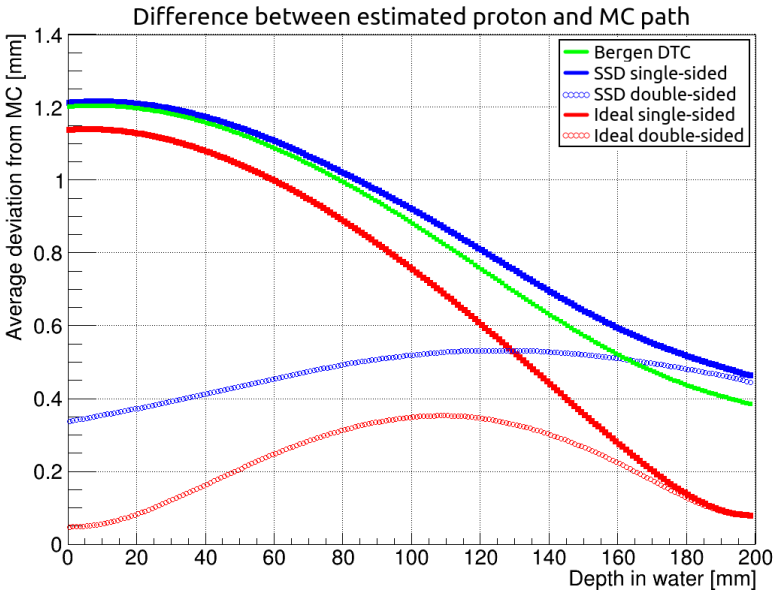

Figure 5.2: The average deviation between estimated MLP and MC path for both ideal and realistic tracker properties in single- and double-sided setups applying a 7 mm FWHM pencil beam. The Loma Linda phase II prototype [106] inspired SSD trackers is used as an example on a realistic double-sided set-up.

tance between the phantom and the inner-most tracker plane (D_p), fixed to 15 cm, and the scattering occurring due to the material budget of the tracker pair, the angle and subsequent hull projection causes the proton position at the rear of the phantom to be misplaced due to inaccuracies in the estimated direction vector of the proton. In a hypothetical single-sided imaging setup where the trackers are placed directly on the surface of the phantom, an improved MLP estimation as can be seen in Figure 5.3, particularly in the rear of the phantom close to the remaining tracker pair when compared to the 15 cm distance. The position resolution of the trackers (5 μm for the DTC and 155 μm for the SSD) become the main limiting factor in the MLP accuracy as observed close to the rear tracker pair at exit position 200 mm.

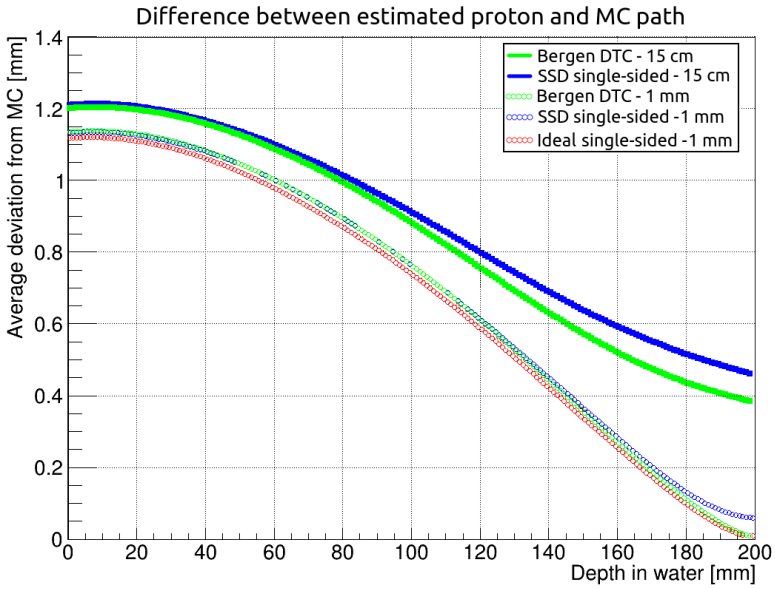

Figure 5.3: The average deviation between estimated MLP and MC path for both ideal and realistic tracker properties in the single-sided setup. The 7 mm FWHM pencil beam of 230 MeV protons are traversing a 20 cm thick water phantom. The distance between phantom edge and inner tracker is 15 cm for the full curves, and only 1 mm for the dotted curves. Note the difference between the 1 mm case for SSD single-sided and DTC at position 200 mm

5.2 Effects of pencil beam spot size and spot-spacing on MLP and spatial resolution

Initial attempts at using the TPS spot mean position/direction information as input to the MLP estimation by Schulte et al. [60] in a single-sided setup resulted in considerable image deterioration in the form of sampling artifacts due to the systematic shift in the entrance positions of the particles. Such artifacts are shown in reconstructed pRads of the spot-phantom (defined in section 3.3) for some selected spot spacing values in Figure 5.4. By using the mean position/direction in the pencil beam as proton entrance position results in a systematic shift of the MLP, particularly in the beginning of the phantom. This can be understood from Figure 5.5 and results in under-sampling of the shaded object regions during pRad reconstruction. The size of these empty areas, and therefore the observed sampling artifacts, are dependent on the spot size, and similar artifacts were observed for all investigated pencil beam spot sizes and spot-spacing

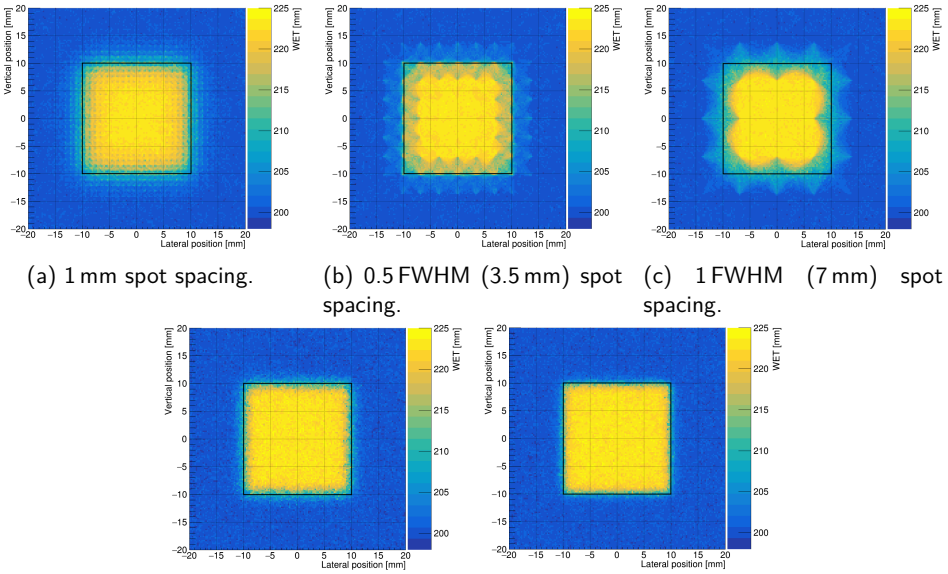

(a) 1 mm spot spacing.

(b) 0.5 FWHM (3.5 mm) spot spacing.

(c) 1 FWHM (7 mm) spot spacing.

(d) 1 FWHM (7 mm) spot spacing, reconstructed with the extended-MLP (Single-sided).

(e) 1 FWHM (7 mm) spot spacing (Double-sided).

Figure 5.4: The *spot-phantom* was scanned with 7 mm FWHM, 230 MeV proton beams at three different spot-spacing settings. The pRads in (a), (b), and (c) were reconstructed using only the TPS mean position/direction as input to the MLP by Schulte et al. [60]. Figure (d) is reconstructed using the extended-MLP and Figure (e) is the double-sided setup not dependent on spot spacing. The black outline encases the actual edges of the aluminium cube.

when this TPS MLP approach was used in a single-sided setup. However, these artifacts disappear for the 7 mm beam when the initial position of the proton is estimated using the extended-MLP. In which case no difference in spatial resolution nor noise was observed for the 7 mm beam when using 1 FWHM or smaller spot-spacing, Figure 5.4. The 2 FWHM spot-spacing did increase the noise, as is expected due to the large distance between spots and thus reduced number of protons between spots. For the double-sided system, the image quality was not affected by the spot size nor by the spacing between spots, as expected due to the proton positions being explicitly recorded on the front tracker.

For the smaller 3 mm FWHM spot however, artifacts were present in the reconstructed single-sided pRad when a 1 FWHM spot-spacing was used with the extended-MLP. This became apparent for the *step-phantom* as seen in Figure 5.6a. These artifacts

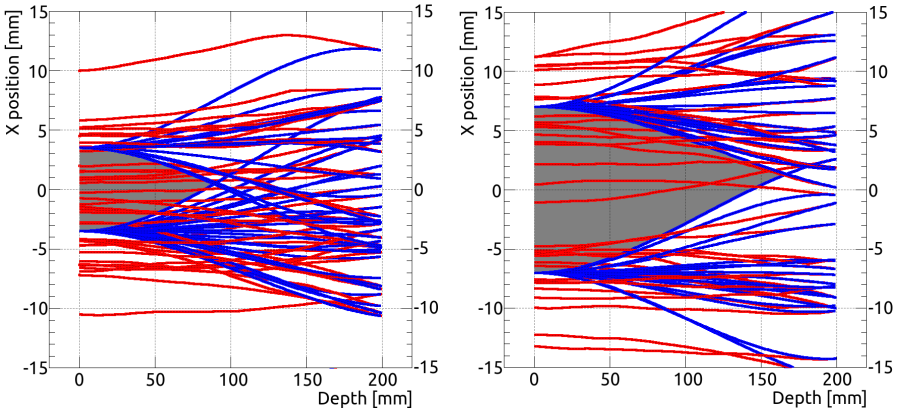

(a) 7 mm beam spot spacing (TPS+MLP).

(b) 14 mm beam spot spacing (TPS+MLP).

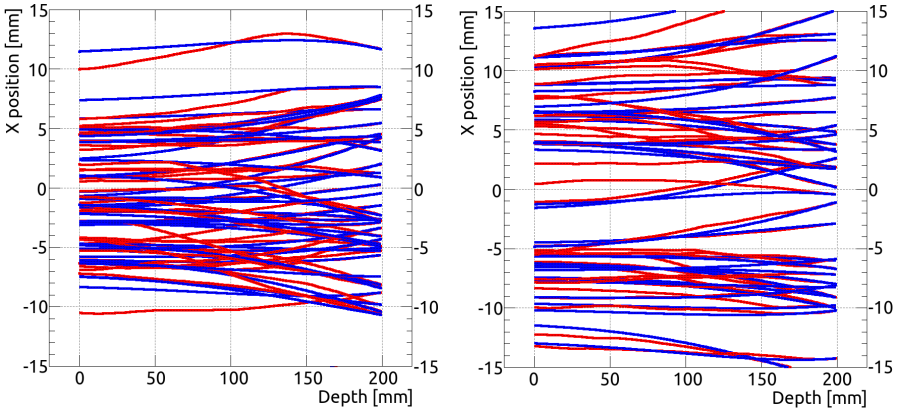

(c) 7 mm beam spot spacing (extended MLP).

(d) 14 mm beam spot spacing (extended MLP).

Figure 5.5: Illustrating the loss of information that is located inside the shaded region caused by wrongly reconstructed proton paths during single-sided proton imaging. Red lines are the true MC proton paths and blue lines are the estimated proton paths. assuming the beam central Gaussian position at entry. A beam spot size of 7 mm FWHM and spot spacing of (a) 1 times and (b) 2 times its FWHM visually emphasises the effect on the shaded region. Figure (c) and (d) contain the same proton data as in (a) and (b), but proton paths are estimated with the extended MLP.

stem from the the smaller corresponding uncertainty (e.g. $\sigma = 1.3\,\text{mm}$ for the 3 mm FWHM beam and $\sigma = 3.0\,\text{mm}$ for the 7 mm FWHM beam) of the beam spot involved in the calculation of the extended-MLP: For a highly focused beam, the extended-MLP will effectively approach the pencil beam mean position and underestimate the spread of protons entering the phantom, as observed in Figure 5.6b. The underestimated spread induces similar artifacts as in Figure 5.4, but these were mitigated by a smaller spot spacing (e.g. 0.5 FWHM) due to the overlapping of the proton distributions and avoiding under-sampling of information in the gaps between pencil beam spots. For the 7 mm FWHM beam, the pencil beam entrance distribution as estimated from the extended-MLP approaches the true distribution of the protons as shown in Figure 5.6d and does not induce image artifacts.

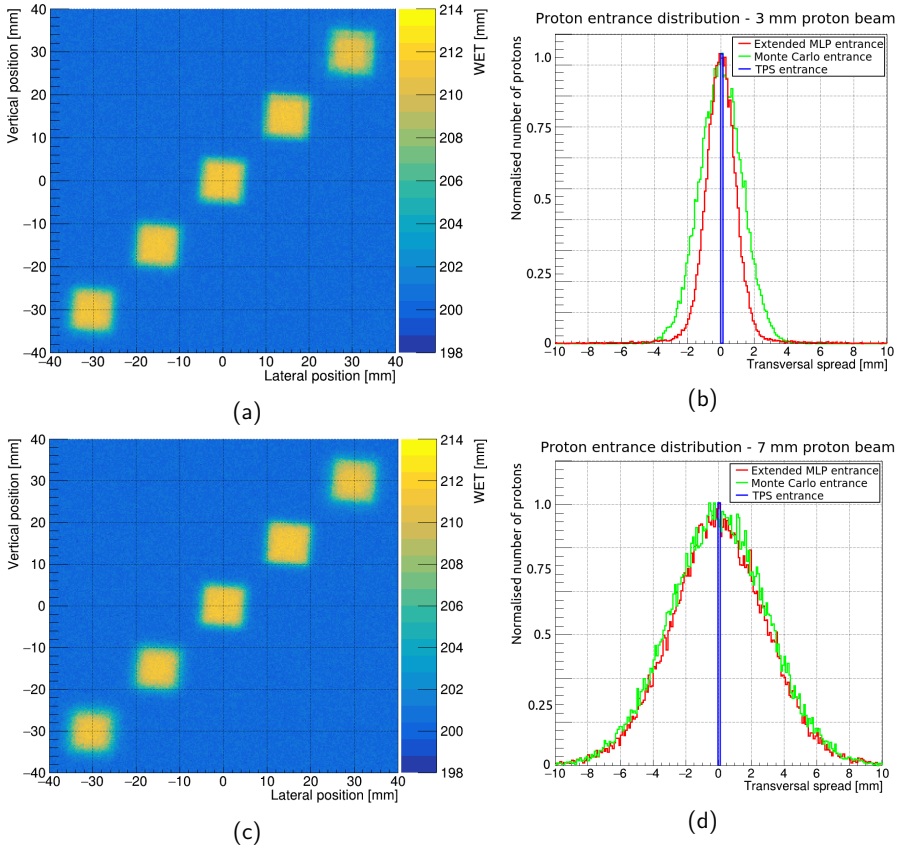

Figure 5.6: Reconstructed pRad of the step-phantom using 3 and 7 mm FWHM beams with 1 FWHM spot spacing in a) and c) respectively. The two pencil beam proton entrance distributions in (b) and (d) are normalised to the same height.

5.3 Proton Radiography

Using the pRad reconstruction code by Collins-Fekete et al. [71] described in section 2.4, the spatial resolution in ideal double- and single-sided imaging setups, as well as the DTC setup were evaluated via a pRad scan of the step-phantom. Reconstructed pRads of the paediatric head phantom were also reconstructed and compared to the ground truth in order to estimate the WEPL error in a clinical setting.

5.3.1 Spatial resolution

The step-phantom was irradiated with the 7 mm FWHM pencil beam and 1 FWHM spot spacing. The 3 mm FWHM pencil beam with 0.5 FWHM (1.5 mm) spot spacing, to limit the image artifacts observed in Figure 5.6, was also used for the sake of comparison. The reconstructed pRads of the step-phantom are presented in Figure 5.7, the $MTF_{10\%}$ from each of the five aluminium inserts together with their CNR are presented in Table 5.1. The average resolution of the of the five inserts are 5.0 lp/cm for the ideal double-sided setup, and 3.1 lp/cm and 3.4 lp/cm for the ideal single-sided setup using the 7 mm and 3 mm FWHM pencil beams respectively. For the DTC setup, the average resolution was 2.8 lp/cm using the 7 mm FWHM pencil beam. The spatial resolution in the double-sided setup is observed to continuously deteriorate with increasing depth in the water phantom, contradicting the MLP estimation quality from Figure 5.2 to be discussed later in subsection 5.5.3. The single-sided setups approach the same spatial resolution as the double-sided setup in the last part of the phantom where the MLP estimation quality and the amount of scattering between the two setups are equivalent.

Depth [mm]	Double-sided Ideal [lp/cm]	Single-sided Ideal (7 mm) [lp/cm]	Single-sided Ideal (3 mm) [lp/cm]	Single-sided DTC (7 mm) [lp/cm]
15	7.2 (15.2)	2.6 (13.6)	3.0 (15.9)	2.6 (12.8)
57.5	6.2 (13.3)	2.8 (12.0)	3.5 (13.6)	2.8 (12.5)
100	4.9 (14.4)	3.5 (11.6)	3.7 (13.4)	3.0 (10.3)
142.5	4.0 (14.8)	3.8 (12.0)	3.8 (12.8)	3.0 (12.6)
185	2.9 (14.6)	2.9 (12.5)	2.9 (12.4)	2.6 (11.2)

Table 5.1: $MTF_{10\%}$ of the five aluminium cubes inside the step-phantom for both ideal double- and single-sided imaging systems and the DTC. For each aluminium cube the corresponding CNR is given in parentheses.

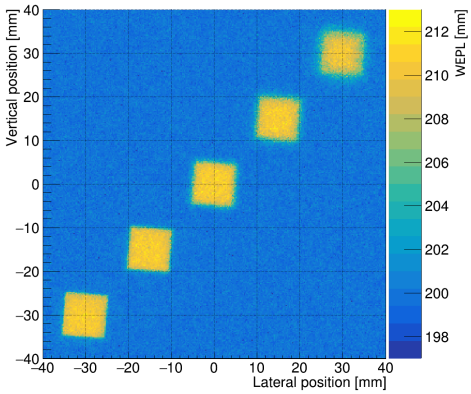

(a) Ideal double-sided system.

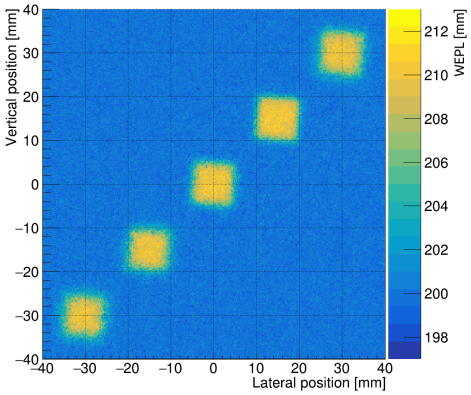

(b) Ideal single-sided system (7 mm FWHM pencil beam).

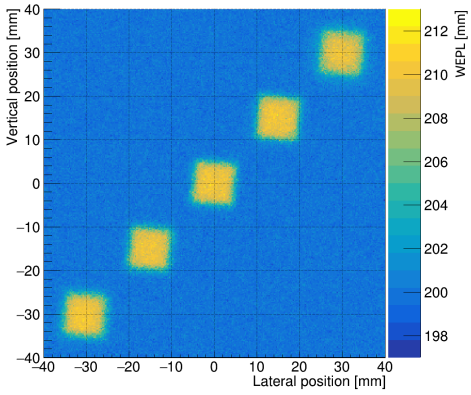

(c) Ideal single-sided system (3 mm FWHM pencil beam with 1.5 mm spot-spacing).

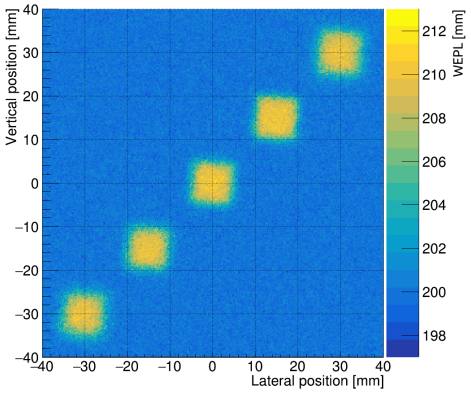

(d) Bergen DTC single-sided system (7 mm FWHM pencil beam).

Figure 5.7: pRad of the step-phantom from the ideal double-sided setup (a), ideal single-sided with 7 mm FWHM beam and 1 FWHM spot spacing (b) and 3 mm FWHM beam with 0.5 FWHM spot spacing (c), and the DTC (d) using the 7 mm FWHM beam and 1 FWHM spot spacing.

5.3.2 Clinical proton radiography

To investigate a clinically relevant scenario, the 3 mm with 0.5 FWHM spot spacing and 7 mm pencil beams with 1 FWHM spot spacing was used to image the anthropomorphic paediatric head phantom. The reconstructed WEPL from both the double- and single-sided pRad were compared to the ground truth integrated WEPL image and shown in terms of resulting WEPL error in Figure 5.8. WEPL error profiles through the brain, eyes, and mouth regions are shown in Figures 5.8c – 5.8e for easier comparison of

double- and single-sided setups. Figure 5.9 shows the equivalent investigation based on the DTC setup compared to the ideal pRad setups when applying the 7 mm FWHM pencil beam. The respective noise maps (given as the standard deviation of the WEPL values in each image pixel) are shown in Figure 5.10. The underlying reconstructed pRads are found in Appendix D.

The single pRad reconstruction of the head phantom took approximately 80 min to complete on a single Intel® Core™ i5-6300U CPU core. About one third of this time was spent on filtering, the rest on the MLP and image reconstruction. However, no optimization efforts are included and the reconstruction time can be reduced considerably if the code is translated and performed on a Graphical processing Unit (GPU).

5.4 Proton CT

Using the pCT reconstruction code DROP-TVS [77], the CTP528 (line-pair), CTP404 (sensitom), and paediatric head phantom underwent a full pCT scan in simulations and pCT images were reconstructed. The spatial resolution of ideal double- and single-sided imaging setups, as well as the DTC setup were evaluated using the line-pair phantom. Similarly, the RSP accuracy of seven different materials in the sensitom phantom were evaluated using the three imaging setups and compared. Lastly, pCT reconstructions of the paediatric head phantom were obtained and their RSP distributions compared between the different imaging setups.

5.4.1 Spatial resolution

Proton CT images of the Catphan® CTP528 line pair module in Figure 5.11a show the central slice reconstructed from the ideal double-sided, ideal single-sided, and the DTC setup. Figure 5.11b shows the MTF computed from the maximum-to-minimum contrast for each set of line pairs relative to the reference contrast and fitted with a sigmoid function. The exact $MTF_{10\%}$ and $MTF_{50\%}$ are listed in Table 5.2. With ideal trackers, the visual $MTF_{10\%}$ was 3.83 lp/cm for single-sided compared to 4.95 lp/cm for the double-sided pCT reconstruction, i.e. the removal of the front tracker pair in the single-sided setup reduced the spatial resolution by $\sim 23\,\%$. For the DTC trackers, the difference between the two single-sided setups was 8 %, with $MTF_{10\%}$ of 3.83 lp/cm

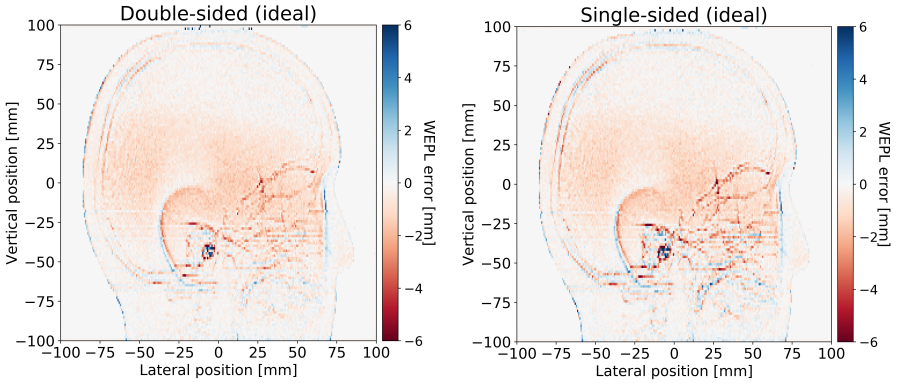

(a) Ideal double-sided set-up, WEPL error map.

(b) Ideal single-sided, WEPL error map (7 mm FWHM pencil beam.)

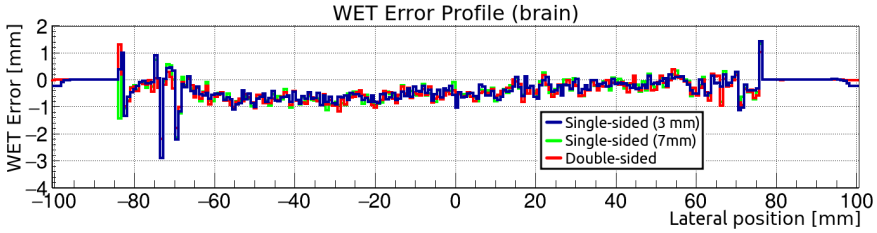

(c) WET error profile of the brain through vertical position 30 mm in (a) and (b).

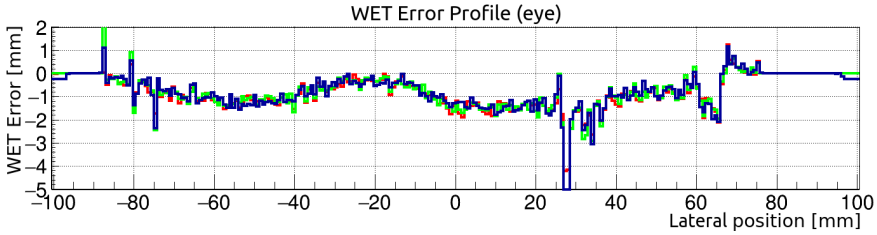

(d) WET error profile of the eye structures through vertical position 0 mm in (a) and (b).

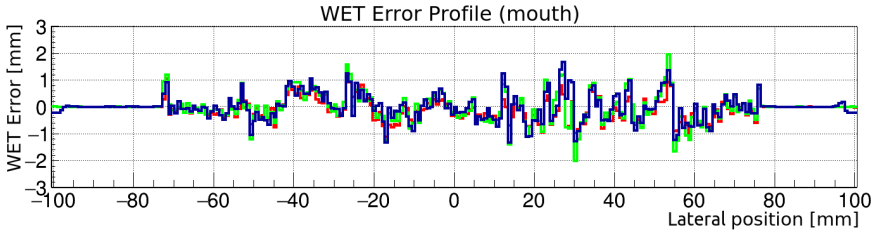

(e) WET error profile of the facial structures through vertical position -50 mm in (a) and (b).

Figure 5.8: Comparing double-sided and single-sided reconstructed WEPL error (a-b) with ideal trackers. Including three error profiles for detailed views of the brain, eye, and facial structures (c-e). Red curve is the double-sided image, blue curve is the single-sided image with the 7 mm FWHM beam, and green curve with the 3 mm FWHM beam.

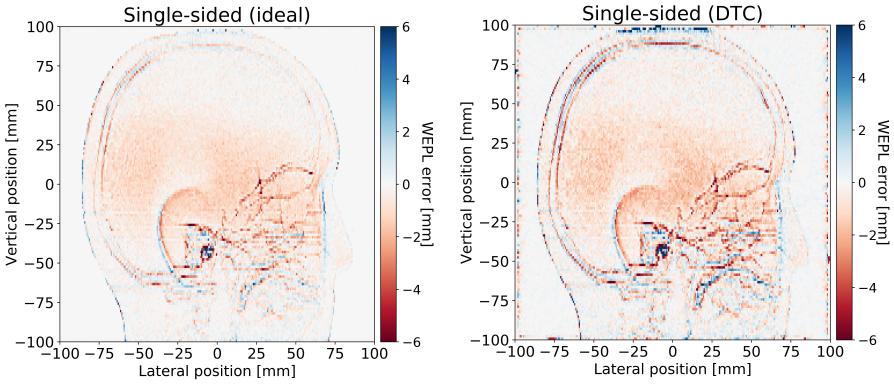

(a) Ideal single-sided WEPL error map (7 mm FWHM pencil beam).

(b) Bergen DTC single-sided WEPL error map (7 mm FWHM pencil beam).

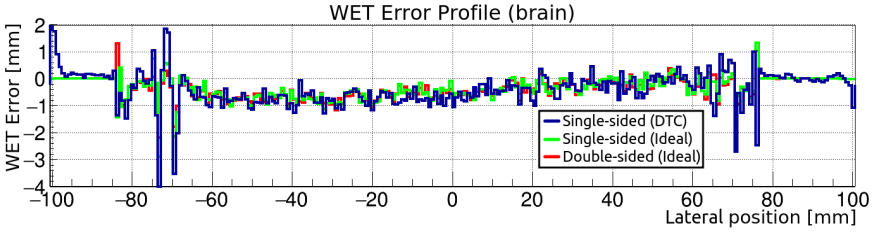

(c) WET error profile of the brain through vertical position 30 mm.

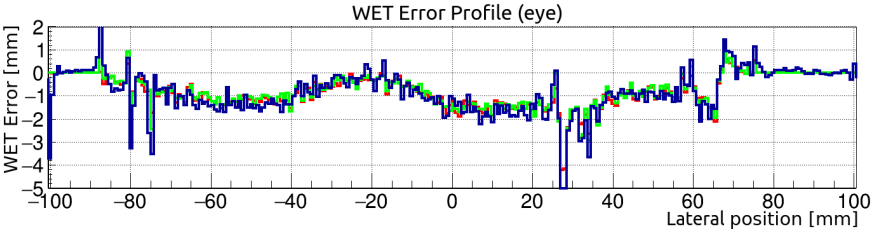

(d) WET error profile of the eye structures through vertical position 0 mm.

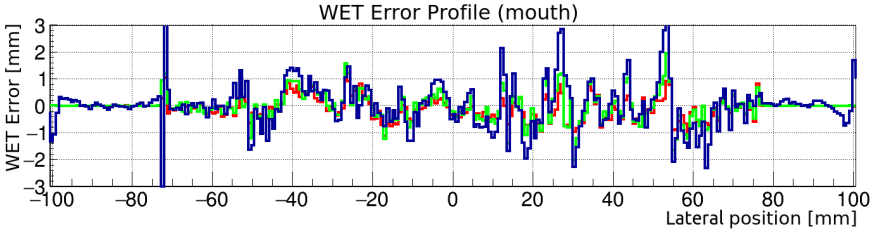

(e) WET error profile of the facial structures through vertical position -50 mm.

Figure 5.9: Comparing Ideal and DTC reconstructed WEPL error (a-b) with ideal trackers and the 7 mm FWHM pencil beam. Including three error profiles for detailed views of the brain, eye, and facial structures (c-e). Red curve is from the ideal double-sided image, green curve from the ideal single-sided image, and blue curve from the DTC image.

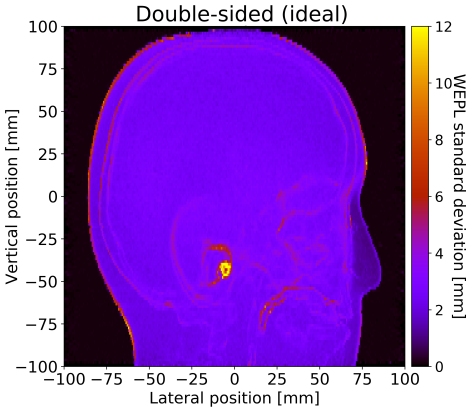

(a) Noise map of the ideal double-sided pRad.

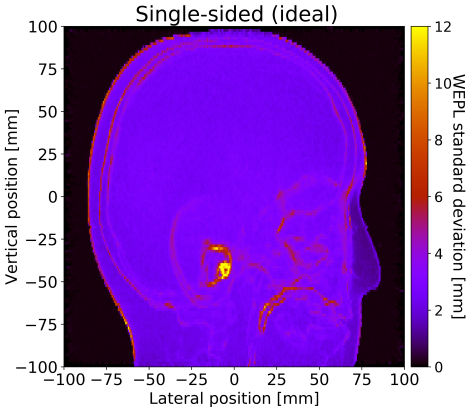

(b) Noise map of the ideal single-sided pRad (7 mm FWHM pencil beam)

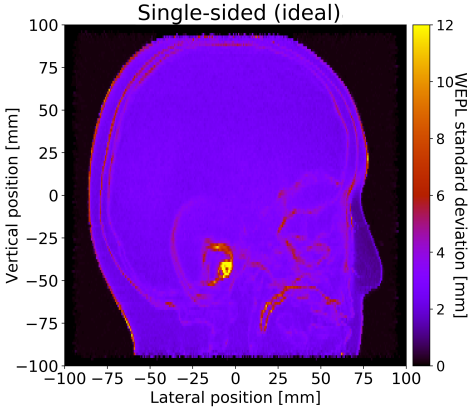

(c) Noise map of the ideal single-sided pRad (3 mm FWHM pencil beam)

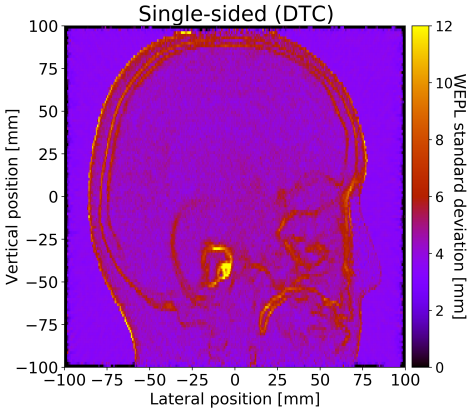

(d) Noise map of the DTC pRad (7 mm FWHM)

Figure 5.10: Noise maps showing the standard deviation of the proton WEPL in each reconstructed image pixel.

Table 5.2: $MTF_{10\%}$ and $MTF_{50\%}$ for the three pCT imaging setups, ideal double sided, ideal single-sided, and DTC.

Spatial resolution [lp/cm]		
	$MTF_{10\%}$	$MTF_{50\%}$
Ideal double-sided	4.95	3.03
Ideal single-sided	3.83	2.22
DTC	3.54	1.82

and 3.54 lp/cm for the ideal and the DTC single-sided setups respectively. In total, the DTC setup when compared to the gold-standard and ideal double-sided setup had the spatial resolution reduced by $\sim 28\,\%$.

5.4.2 RSP accuracy

The Catphan® CTP404 sensitom module was reconstructed and the central slice is shown in Figure 5.12a from the DTC setup. In Figure 5.12b a comparison of the average RSP errors in percent (calculated as the difference between the reconstructed value and the MC reference value, divided by the reference value) for each of the seven materials in the CTP404 phantom (excluding air) for the two ideal setups and the DTC setup is shown. The mean RSP values were measured in a small area in the center of each insert (shown by the small colored circles in Figure 5.12a) and averaged over 10 reconstructed slices. The error bars represent the standard deviation in percent of each RSP distribution. The magnitude of the error bars for the DTC setup indicate a relatively high level of noise. For all investigated double- and single-sided setups the mean RSP error for each material is below 0.5%.

5.4.3 Clinical proton CT

Lastly, a full pCT reconstructions of the paediatric head phantom approximating a clinically realistic patient setting was performed. The frequency distribution of reconstructed RSP values from every image-voxel was compared between the three investigated imaging setups, including the RSP reference values of the seven patient materials (listed in Table 3.3) from the ground truth CT image. Some selected slices from the DTC reconstructed head phantom is shown in Figure 5.13a and the relative RSP distributions overlaid in Figure 5.13b. Three profiles covering some objects of interest

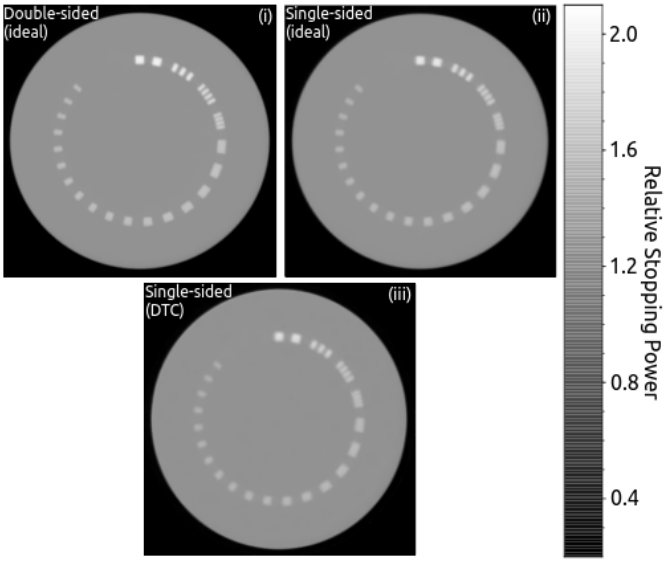

(a) pCT slice of the line-pair phantom (CTP528 phantom module). The ideal double-sided (i) and single-sided (ii), and the single-sided DTC (iii) setup.

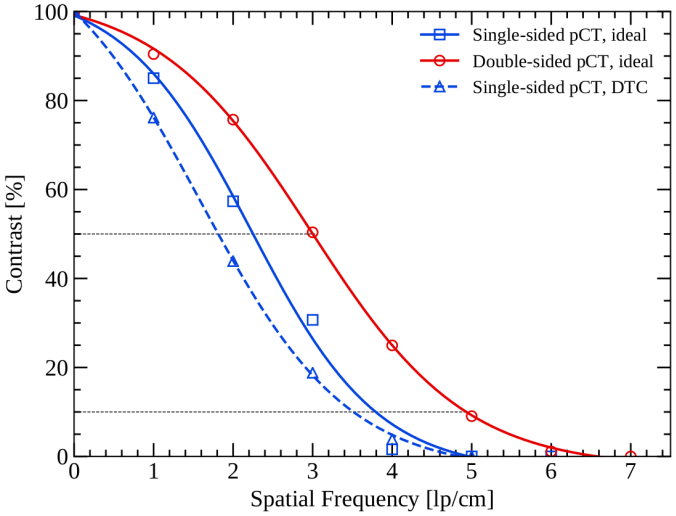

(b) MTF of the CTP528 line-pair module. A sigmoid fit to the data has been performed to extend the MTF over the whole frequency range. The MTF from the double-sided set-up is shown in red, the single-sided setups in blue. The solid lines depict the case of the ideal setups, dashed lines show the results for the DTC.

Figure 5.11: Spatial resolution results using the CTP528 phantom module.

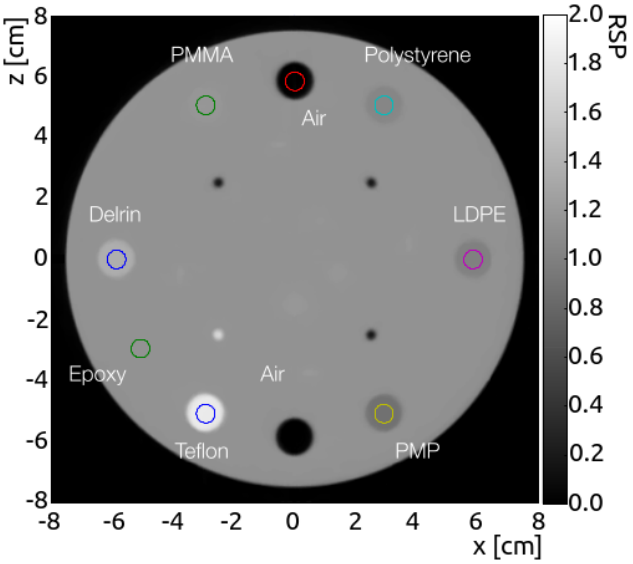

(a) Central slice of the reconstructed CTP404 phantom using the DTC setup.

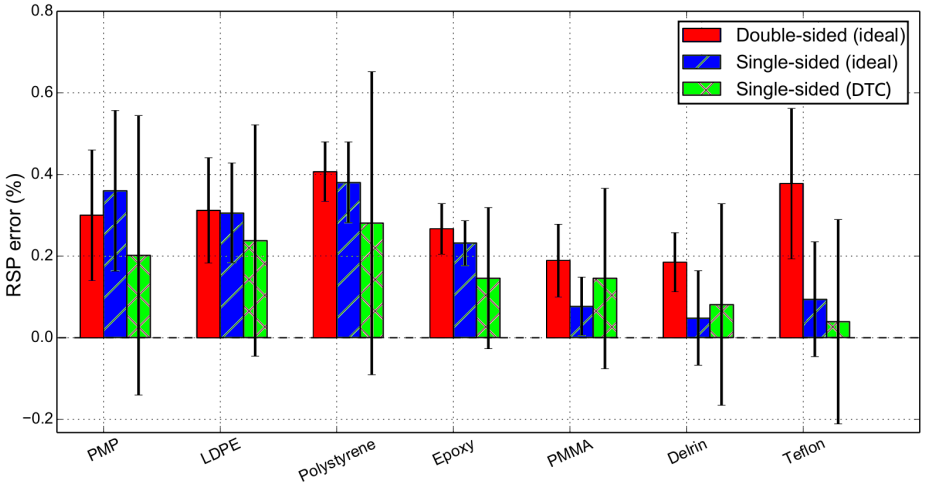

(b) Reconstructed RSP values from the marked areas in Figure (a) compared to reference values.

Figure 5.12: RSP error in percent comparing reconstructed and reference RSP values. All mean RSP errors are less than 0.5%.

(mouth, ear-canal, and brain) and illustrating some of the observed RSP distributions are shown in Figure E.1, Figure E.2, and Figure E.3.

The full pCT reconstruction of the head phantom took approximately 1.5 hours (4383.17 s) to complete using an Intel® Xeon® E5-2697 v2 CPU @ 2.70GHz with 48 cores, and an NVIDIA® GeForce GTX 650 GPU as a part of the Kodiak computer cluster at the Baylor University in Texas, USA.

5.5 Discussing the reconstruction precision in single-sided proton imaging

5.5.1 Most likely path in a single-sided setup

The MLP in a single-sided setup has the highest deviation from the actual path in the very beginning of the phantom and continually improves with decreasing distance to the rear trackers. This behaviour is seen for all investigated pencil beam sizes, while smaller pencil beam sizes offer reduced initial deviations due to the smaller width of the incoming pencil beam. If one does not take the pencil beam uncertainty and associated co-variance matrix into account in the MLP, and only use the TPS spot position and beam direction as initial proton parameter vector, the MLP deviations reach as high as 2.4 mm at the entrance of a 20 cm water phantom and using the 7 mm FWHM beam. This also results in systematic errors in the position of incoming protons that cause considerable image artifacts in reconstructed images, making the conventional MLP approach by Schulte et al. [60] unusable in single-sided imaging setups. Instead, the extended-MLP that take the proton position uncertainty inside the pencil beam into account via the co-variance matrix detailed in section 2.3 has to be used. With the extended-MLP the MLP deviation at the entrance is reduced by a factor 2 for the 7 mm FWHM pencil beam and systematic image artifacts attributed to the TPS entrance position are removed. A similar behaviour is seen for the more focused 3 mm FWHM beam, albeit with a smaller benefit from the extended-MLP formalism due to the already small size of the incoming pencil beam.

As the proton approaches the remaining tracker plane in a single-sided setup, where

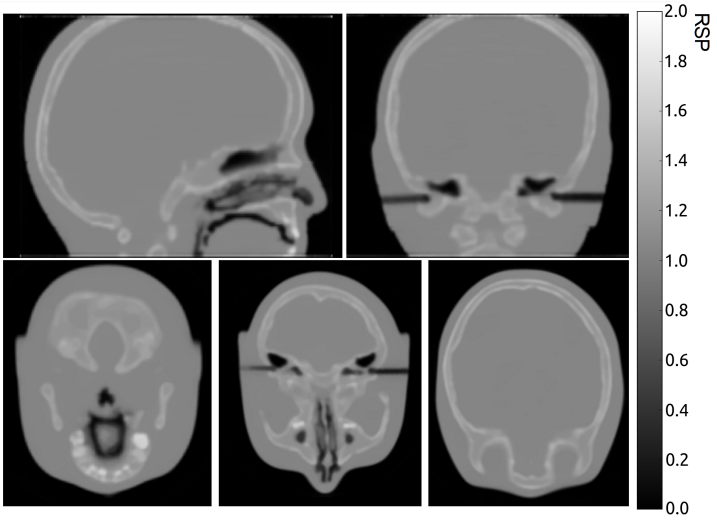

(a) Selected slices from the head phantom pCT reconstructed after using the DTC imaging setup.

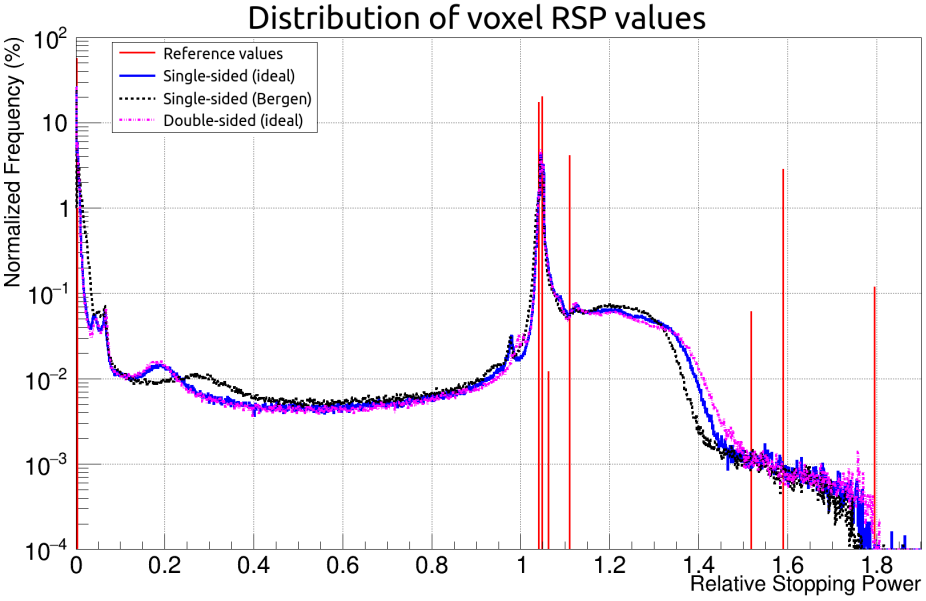

(b) Frequency distribution of RSP values from the pCT images of the head phantom reconstructed from proton data obtained from the three proton imaging setups. Red bars represent the relative frequency of the patient materials from the ground truth CT image. Results are normalized to the total number of voxels in each respective image ($240 \times 240 \times 112$). Note the logarithmic y-axis.

Figure 5.13

its position is accurately recorded, the accuracy of the MLP estimate will continuously improve and its MLP deviation will in the end approach the same amount of deviation as in an equivalent double-sided setup close to the rear inner tracker plane. This results in the spatial resolution of objects of interest close to the remaining rear tracker plane to be nearly identical in both single- and double-sided setups as seen for the last aluminium insert in Table 5.1 from pRad of the step-phantom.

However, due to the position resolution and scattering inside realistic tracker pairs determining the proton parameter vectors, the proton will potentially experience a change in the direction it originally had when exiting the phantom to be imaged. This becomes problematic when there is a large distance between the inner tracker pair and the phantom (D_p). Because the start and end position of the proton MLP is projected unto the contour of the phantom along the recorded angle (hull-finding), the proton position can be misplaced on the phantom contour and negatively affect the start and/or end position used in the MLP estimation. The severity of this effect is dependent on the amount of material budget in the trackers and distance between the inner tracker plane and the phantom, as reported by other studies [24, 56]. We see this impact when comparing the MLP in ideal and realistic imaging setups in Figure 5.2, but the effect is reduced considerably as the distance between phantom and inner tracker plane is reduced down to 1 mm in Figure 5.3 (while keeping the 5 cm D_t distance between the trackers). A single-sided imaging setup for use in pRad does have the potential to take advantage of a reduced distance between phantom and tracker plane by the relative ease of moving the tracker and energy detector close to the patient. This is however considered a mechanical problem and will be difficult to implement in a pCT setting where the detector must have enough space to rotate around the patient.

5.5.2 Pencil beam spot-size and spot-spacing role

While a smaller pencil beam is associated with increased MLP accuracy, and thus spatial resolution in images, the number of beam spots necessary to cover a volume such as the head is drastically increased for thinner pencil beams. E.g. the 3 mm FWHM beam with 1.5 mm spot spacing require more than 11000 beam spots to cover the head phantom area ($180 \times 180 mm^2$). This results in two consequences: One, the typical time of contemporary beam delivery (based on the Heidelberg Ion Therapy facility [92]) to

change from one raster position to the next is 0.5 ms, and each beam spot needs to be irradiated for at least 1 ms to achieve a valid position measurement for the beam delivery control system. This means that changing the beam positions 11000 times will need 5.5 s to complete, and spend at least 11 s to irradiate the entire head phantom in a single projection, if only 90 projections were to be taken in a full pCT scan (90 projections times 16.5 s), this will take 1485 s to complete and make pCT unfeasible due to the scan time. For a more contemporary pencil beam spot size of 7 mm FWHM and 7 mm spot spacing, only 620 beam spots is necessary to cover the head phantom, this amounts to roughly 1 s per projection and thus only require 90 s to complete a pCT scan. Second, the obligatory 1 ms scan time in each beam spot combined with a typical beam intensity of 10^7 protons per second, the amount of protons in each beam spot is at least 10000. If a 3 mm FWHM pencil beam with spot-spacing of 1.5 mm need 11000 spots to cover the head phantom, every projection will receive 110 M protons, increasing not only the scan time, but also the dose to the patient and a vast amount of data to be processed or discarded by the energy detector. For the 7 mm FWHM beam and 7 mm spot spacing, the amount of protons would amount to a more manageable 6.2 M protons per projection.

These two consequences are the main reasons why the pCT simulations in this work are assigned the 7 mm FWHM pencil beam size and 7 mm spot spacing only. Advances in beam delivery technology will be necessary for pCT to take advantage of thinner pencil beams. Luckily, as has been seen in the image quality of pRad of a clinical head phantom, a thinner pencil beam does not present a considerable improvement in image quality in a clinical scenario.

5.5.3 Spatial resolution limit of pRad

From the observed spatial resolution in pRad of the aluminium inserts inside the step-phantom (Table 5.1), particularly that of the last insert placed close to the end of the 20 cm water phantom, it became apparent that although the MLP does affect the spatial resolution of a pRad, the decreasing spatial resolution with respect to depth contradicts the increasing MLP accuracy in both double- and single-sided setups.

A separate study aiming to contribute to the understanding of the observed spatial resolution limitation of pRad was performed by Volz et al. [115]. It was shown in [115]

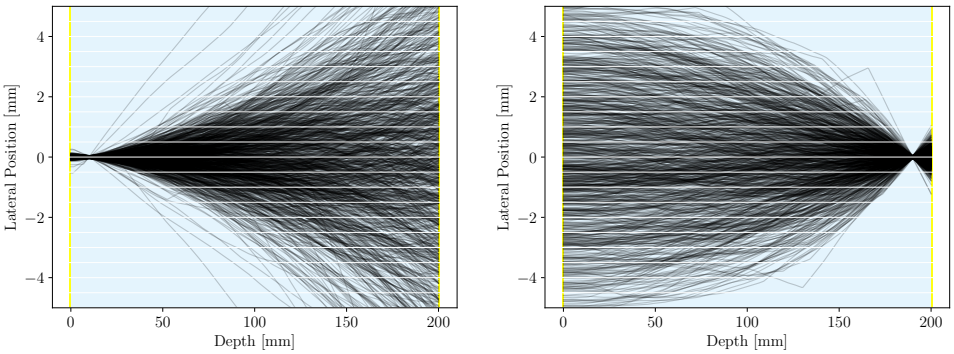

(a) $u_p = 10\,\text{mm}$ (b) $u_p = 190\,\text{mm}$

Figure 5.14: Monte Carlo generated trajectories for 200 MeV protons traversing a 200 mm thick water target. The incident beam was as a flat field with no divergence and only tracks that crossed a slit of 0.1 mm width in vertical direction located at a depth of (a) 10 mm and (b) 190 mm were plotted. The white lines depict pixel columns corresponding to a pixel width of $\Delta t = 0.5\,\text{mm}$ which was chosen for better visibility. Figure is re-drawn from Volz et al. [115].

that projecting the scattered particle paths onto a single 2-dimensional image would inevitably result in a limited spatial resolution lower than expected when based solely on the MLP uncertainty. The spatial resolution also decreased with increasing depth in the object even when the true particle path through the object was known via MC simulations. This can be explained by Figure 5.14 where scattered proton paths are projected onto a single image plane along parallel channels, similar to the pRad reconstruction algorithm by Collins-Fekete et al. [71] used in this thesis: Particles that cross a point-like object at the entrance region of the phantom (e.g. at depth position 10 mm in Figure 5.14a) will reach distant lateral pixel channels only towards the rear of the phantom. They are then more likely to just cross these pixel channels, rather than travel a greater length in them as their trajectory is deflected compared to the channel orientation. On the other hand, if the point-like object is located close to the exit of the phantom (e.g. at depth position 190 mm in Figure 5.14b), particles can traverse a larger part of their path length in distant pixel channels, before they scatter to the point-like object. Hence, when computing the image using the path length in a channel to weight the particle's WEPL, point-like objects located at the rear of the water tank will be spread out more compared to point-like objects located close to the phantom entrance — even if the GT particle trajectories were known. Only when the depth of a feature was known

and using a Plane of Interest Binning (PIB) reconstruction algorithm [74] was the spatial resolution of that exact feature in the plane of choice equal to the path estimation accuracy. A theoretical description of the depth-dependent point-spread function (PSF) for different pRad algorithms found in literature was derived in the work by Volz et al. [115] and the reader is refereed to this publication for the full details on the underlying MC simulations and reconstruction algorithms.

As there is no direct pRad algorithm that will produce a spatial resolution that is subject only to the MLP accuracy everywhere in the phantom in a single pRad, and since no prior knowledge of the imaged phantom is assumed, all pRad results presented in this thesis are obtained using the pRad reconstruction algorithm by Collins-Fekete et al. [71] that result in a generally high resolution pRad everywhere in the phantom.

5.5.4 Discussion of clinical pRad

The reconstructed pRads of the clinically relevant paediatric head phantom and detailed WEPL error maps comparing the reconstructed image with the ground truth image revealed that removing the front tracker pair reduced the spatial resolution. The lower spatial resolution can be seen in the high gradient facial structures in the form of increased WEPL error (Figure 5.8 and Figure 5.9) and increased noise (Figure 5.10) compared to the double-sided setup. These high gradient regions are naturally present in the facial structures and air cavities of the head phantom, and due to increased scattering in adjacent high density materials the WEPL error is inherently increased at high gradient edges. Based on profiles through areas of interest in the pRad (brain, eye, mouth), WEPL errors in the facial structures would fluctuate between 1% and up to 3% of the ground truth WEPL.

The difference between a double- and single-sided imaging setup come to light in WEPL error profiles covering the high gradient structures, particularly around the mouth, where the difference between the two imaging setups could reach over 1 mm. However, the average difference in reconstructed WEPL between double-sided and single-sided imaging in homogeneous areas such as the brain was less than 0.01 mm. This is expected since the MLP has little effect on the WEPL accuracy when all protons entering the image pixel in question have traversed approximately the same amount of material and experienced the same amount of energy-loss, meaning the difference be-

tween a double- and single-sided setup is negligible in homogeneous volumes. In more heterogeneous volumes, the shifting scattering power due to material differences and thus reduced MLP accuracy will combined increase the noise and deteriorate the spatial resolution and WEPL accuracy of affected regions. Improved MLP estimations based on prior information taking in-homogeneous materials and volumes into account can in principle improve this. Existing studies have however found little difference between the homogeneous water approximation and prior-knowledge on material composition in clinically relevant phantoms, given correct hull-finding for accurate start- and end-point for the water based MLP estimation [63–65].

Concerning the DTC setup with realistically modelled material budget in the trackers and WEPL smearing due to the energy resolution of the DTC (detailed in section 3.5), compared to the ideal single-sided setup in Figure 5.9, the WEPL error is seen to increase at the high gradient facial structures and reaching up to 5% WEPL error compared to the ground truth WEPL. While in the homogeneous areas such as the brain, the difference between the ideal and realistic single-sided setups are negligible.

Since the objective of taking a pRad for particle therapy would be pre-treatment patient alignment, as well as potentially pre-treatment optimization of the Hounsfield Unit to relative stopping power lookup table (HLUT) [14, 15], the impact of the lower spatial resolution in that context would need to be systematically evaluated before definitive conclusions can be drawn.

5.5.5 Discussion of pCT

Spatial resolution

For the simulated pCT of the CTP528 line pair module, the MTF was evaluated for both single-sided and double-sided setups acquired with the 7 mm FWHM scanned pencil beam. With ideal trackers, the visual $MTF_{10\%}$ was 3.83 lp/cm for single-sided compared to 4.95 lp/cm for the double-sided pCT reconstruction. For the single-sided setup and DTC trackers the $MTF_{10\%}$ was 3.54 lp/cm. It has been argued in the work of Krah et al. [56] that due to typical commercial TPS voxel size of 2 mm, the image resolution from pCT imaging should be no worse than 3 lp/cm to enable treatment planning. Following this argumentation, the single-sided setups all returned a spatial resolution just above the expected limit for clinical usefulness. Hence, future work should carefully

investigate whether treatment planning with a single-sided pCT system would indeed be feasible, potentially by creating optimized proton dose plans based on the pCT images reconstructed in this work and perform the treatment in MC simulations according to the dose plan.

It is noted that spatial resolution of pCT images will change depending on the amount of scattering induced, with increased scattering effectively degrading spatial resolution, meaning the amount of material and initial energy will affect the spatial resolution. The recorded spatial resolution in the line pair module is thus only true for this specific phantom, however, the size of the line-pair module is approximately equivalent to a paediatric head phantom. Parameter investigations of the spatial resolution in terms of phantom size and imaging setup can be planned and performed by using the MC simulation framework designed in this thesis work by increasing or decreasing the radius of the epoxy cylinder housing the line pairs.

RSP accuracy

As expected in simulated pCT of the CTP404 sensitom module, the RSP accuracy in all investigated imaging setups are comparable to one another with the mean RSP values being no worse than 0.5% from the reference RSP values of the material inserts in Figure 5.12. As homogeneous areas are not particularly affected by the MLP estimate, since the involved protons in the voxel of interest have all experienced the same mean energy-loss, the RSP/WEPL accuracy in double- and single-sided setups report similar results. The mean RSP from the DTC setup in Figure 5.12 appear at first glance to be better than the ideal setups, this is considered to be an averaging effect due to the increased noise. Small changes in RSP noise will also have an impact on the observable results in Figure 5.12 due to the already high precision of the RSP ($< 0.5\%$). The overestimation of the teflon RSP in double-sided is an example of this, and a profile through delrin and teflon is investigated in Figure 5.15. Likely due to the high density of teflon and thus increased scattering has increased the noise and affected the calculated mean. Nevertheless, the goal of less than 1% accuracy of the RSP in proton imaging is achieved across all investigated imaging setups.

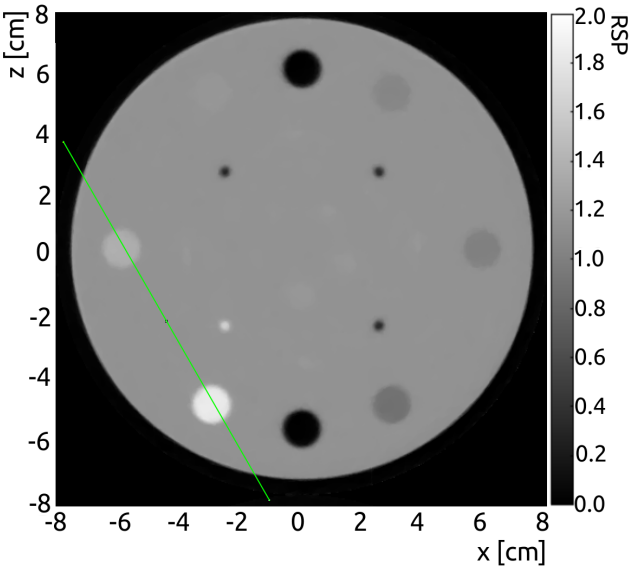

(a) Central slice of reconstructed CTP404 phantom using the DTC setup. A profile along the green line is taken in all three images from their respective imaging set-ups.

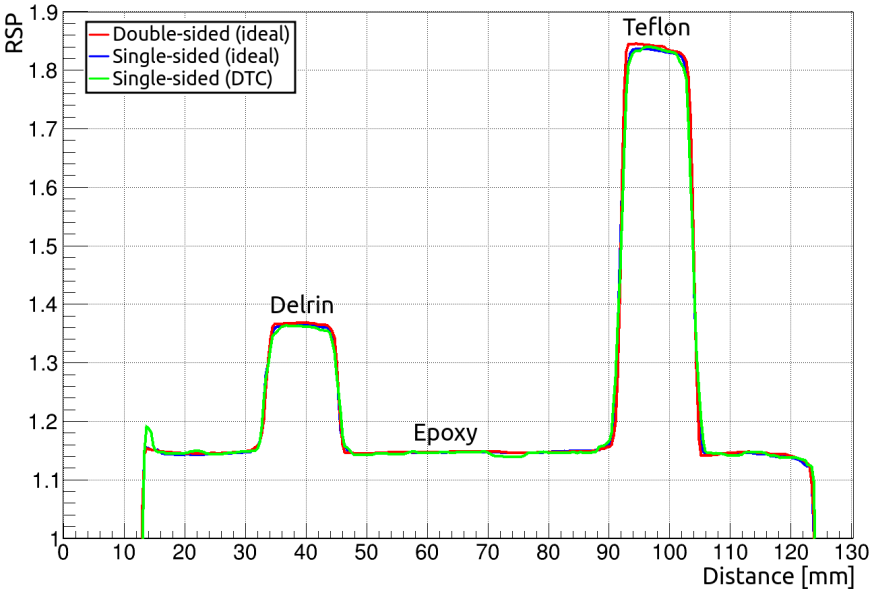

(b) Profiles from pCT reconstruction of the CTP404 phantom for the three imaging systems are overlaid. The reference RSP of involved materials are, 1.144 (epoxy), 1.364 (delrin), and 1.832 (teflon).

Figure 5.15

Clinical pCT of head phantom

The simulated pCT image of the paediatric head phantom reveals several important aspects in proton imaging. Visual inspection of the head phantom in Figure 5.13a shows several relatively nice image slices where many bone structures and objects of interest have been reconstructed and are clearly visible. When looking closer at the distribution of the RSP values belonging to the voxels of the full pCT images in Figure 5.13b it is seen that many of the ground truth RSP reference values are not clearly represented in the pCT images from any of the three proton imaging setups. This is in part due to the larger voxel dimensions of the reconstructed pCT images compared to the reference ground truth CT image. Each pCT image voxel will approach the average RSP value of the involved ground truth voxels and in this work the voxel dimension of the reconstructed pCT images were set to $0.75 \times 0.75 \times 1.25\, mm^3$, compared to the ground truth voxel size of $0.1875 \times 0.1875 \times 1.25\, mm^3$, i.e. 16 ground truth voxels are involved for every reconstructed voxel. The reconstructed RSP in a pCT voxel will therefore consist of multiple RSP values as dictated by the ground truth materials inside the pCT voxel, particularly when small high RSP materials like the teeth are surrounded by low RSP (high gradient regions) the overall RSP will become muddled if the reconstructed voxel size covers the edge in high gradient regions. The RSP is also further deteriorated by scattering out of high gradient regions, as can be seen in air cavities such as the ear canal where the average RSP is increased due to scattering from the surrounding high RSP objects. This is expected as protons are more likely to scatter out of high density structures and create reconstruction artifacts. This is the cause of reduced spatial resolution in proton imaging as the edges between high gradient regions are effectively deteriorated and the RSP there becomes muddled. In the homogeneous and abundant regions of the brain, the RSP values are relatively well represented (i.e. the brain and soft tissue RSP of 1.049 and 1.041 respectively) due to reduced impact of voxel size and scattering. While the high RSP values of the teeth dentin (1.52), teeth enamel (1.8), and cortical bone (1.6) are virtually lost due to voxel size and scattering. It is noted that the $0.75 \times 0.75 \times 1.25\, mm^3$ voxel size is smaller than the typically available voxel size of 2 mm in commercial TPS. If the voxel size would be bigger, the mean RSP value inside the voxel is expected to be closer to the overall mean of all the involved material RSP in that voxel, and further blend the underlying ground truth RSP of the materials that

are inside that voxel.

Some selected profiles through regions of interest in the mouth, ear, and brain are shown in Figure E.1, Figure E.2, and Figure E.3 respectively and illustrate the RSP distribution of these structures. Due to the improved MLP and spatial resolution in the double-sided imaging setup, the reference RSP is more accurately reproduced compared to the single-sided setups, but the double- and single-sided setup are nevertheless comparable. Future studies into applied treatment planning will have to be performed to answer the question of whether these single- and double-sided pCT images are sufficient for treatment planning purposes.

6. Summary and outlook

6.1 Monte Carlo simulation framework for proton imaging

The MC simulation based proton imaging analysis framework in this thesis was developed with the intention of investigating a single-sided proton imaging setup and creating proton data for use in image reconstruction allowing for evaluation of the expected image quality from proton imaging setups. Mainly two different imaging setups were considered in this work, one with both front and rear tracker pairs (double-sided) and one with only a rear tracker pair (single-sided) as detailed in section 2.1 and section 2.2 respectively. Protons can undergo a relatively significant amount of MCS depending on the material and thickness traversed, this requires protons used in proton imaging to be subjected to MLP estimations (section 2.3) to better the knowledge about the path of the proton through the imaged object and improve spatial resolution of reconstructed images. A single-sided proton imaging setup is expected to have a negative impact on the accuracy of the MLP estimations due to missing information from a front tracker pair and result in a reduced image quality. The removal of the front tracker pair is however considered a potentially important step in bringing pCT closer to a clinical reality by reducing scan times (to less than five minutes) and the complexity of the imaging setup. One of the main objectives of this thesis work was to design the MC simulation framework detailed in chapter 3 and use it to evaluate and compare the image quality in a single-sided imaging setup to the gold standard in proton imaging, the double-sided setup. Multiple phantoms detailed in section 3.3 were implemented in the MC simulations for this purpose and simulated proton imaging data was used to reconstruct both pRad and pCT images using the algorithms introduced in section 2.4 and section 2.5 respectively. Spatial resolution, RSP/WEPL accuracy, and a clinically relevant paediatric head scenario was used to investigate and quantify the impact on image quality obtained from a single-sided imaging setup. This work was motivated by the Bergen pCT collaboration that, at the time of writing, is building a prototype DTC for pCT pur-

poses. This DTC is to be built using ALPIDE chips and without a front tracker pair, as detailed in section 3.4. This type of MC simulation can aid in modifying and evaluating detector designs before construction and before experimental data becomes available.

In addition, a MC simulation based investigation into the radiation environment surrounding the DTC was developed in chapter 4. The FLUKA MC tool-kit (section 4.2) was used for this investigation due to its relative ease when scoring radiation damage relevant quantities such as dose, hadrons with energies larger than 20 MeV (HADGT20M) and 1 MeV neutron equivalent (SI1MEVNE) fluence. From the radiation environment induced during both proton CT (section 4.3) and proton therapy (section 4.4), radiation damage to sensitive electronics (FPGAs) and the ALPIDE chips were estimated in terms of SEU, cumulative TID and displacement (NIEL) effects. Due to the high radiation hardness of the involved electronics (Xilinx FPGA and ALPIDE), the DTC is expected to be operational for at least 30 years under the assumptions discussed in section 4.6.

Once all the MC simulation framework (phantoms, pencil beam scanning, and imaging setups) from chapter 3 were implemented, analysis of the proton data, MLP estimation, and image reconstruction was performed to evaluate the reconstruction precision in chapter 5. First, the expected deterioration of MLP estimations due to the removed front tracker was investigated in section 5.1, and as expected, an increased MLP deviation from the actual proton path is observed in a single-sided setup versus a double-sided setup. In particular, the deviation was more pronounced in the entrance region furthest away from the remaining rear tracker pair in the single-sided setup. The second investigation concerning the the single-sided setup was the pencil beam spot size and spot spacing impact on image quality in section 5.2. While several pencil beam and setup parameters were investigated to determine the impact on MLP and image quality in a single-sided setup, including spot spacing and pencil beam spot size as a function of the beam FWHM, the realistic and contemporary 7 mm FWHM pencil beam with 1 FWHM spot spacing was used as the primary beam in all full pCT scans and reconstructions. This was due to the observed results in a clinical scenario that the difference between a 7 mm and 3 mm FWHM pencil beam did not bring considerable improvement to image quality in the paediatric head phantom as observed in subsection 5.3.2, Figure 5.8, and reduced spatial resolution only became apparent in high gradient regions at the bound-

ary between high and low density regions like the facial structures, regions that are typically avoided in proton therapy.

The MC simulation framework can be used in future studies designed to perform parameter scans comparing the necessary proton intensity and beam delivery settings to ensure accurate coverage and optimal image quality both inside and outside the realm of contemporary clinical availability. Full modelling and implementation of a specific beam line, instead of the general TPS beam scanning source in GATE is also possible to further improve and specialize the MC simulation framework for use in a specific facility. As such, with future studies in mind, the overall MC simulation framework was made to be flexible and can readily be updated in terms of relevant detector geometry, pencil beam properties, proton energies and also particle species such as helium (helium CT). Exemplified by a preliminary helium radiography study performed in house by Pettersen et al. [103] using the analysis framework (MC simulations and reconstruction algorithms) detailed in this thesis work.

The image quality in pRad of a clinically relevant paediatric head phantom did not show a considerable difference in reconstructed WEPL outside of high gradient regions. Reconstructed WEPL in high gradient regions are typically affected negatively due to the inherent scattering of protons often scattering out of high density regions causing a higher variability of proton energy-loss (and thus WEPL) around high gradient regions. In homogeneous regions, the reconstructed WEPL is less affected by the scattering as the involved protons all experience approximately the same amount of energy-loss irrespective of scattering (assuming appropriate 3-sigma filtering of proton angles has been applied). The DTC pRad showed similar results as the ideal single-sided setup, albeit with increased noise due to less than ideal reconstruction of the proton WEPL detailed in section 3.5.

In pCT images of the CTP528 phantom (line-pair module) the ideal double-sided imaging setup had a spatial resolution (MTF10%) of 4.95 lp/cm, and the ideal single-sided had 3.83 lp/cm, effectively losing about 1.1 lp/cm when removing the front tracker pair. The DTC achieved a similar spatial resolution of 3.54 lp/cm. A spatial resolution more than 3.0 lp/cm has been argued to be sufficient for treatment planning purposes. The RSP accuracy of investigated materials in the CTP404 phantom (sensitom) was in all imaging setups below 0.5% and fulfill the intended design requirements for a pCT

imaging setup.

Overall, the objectives of this thesis as listed in section 1.4 were considered via the designed MC simulation framework applying pencil beam scanning, implementation of relevant phantoms, and tracker planes characterizing proton imaging setups. Both ideal (no material budget) and realistic tracker pairs (with material budget) were investigated and proton data was recorded as dictated by the properties of the trackers (position resolution, material budget and relative positions to the phantom). The quality of reconstructed images based on the simulated proton data and using the available pRad and pCT reconstruction algorithms were evaluated and quantified in terms of spatial resolution and RSP accuracy, illustrating the feasibility of a single-sided imaging setup and the DTC for proton imaging purposes.

6.2 Outlook - Towards clinical proton imaging

The image quality based on spatial resolution observed in the reconstructed CTP528 line pair module images revealed that the single-sided imaging setup can produce images expected to be suitable for treatment planning. The RSP accuracy from the CTP404 sensitom module also revealed excellent RSP accuracy better than the final goal of proton imaging for use in treatment planning intended to limit uncertainties in to the proton range and reduced treatment margins ($< 1\%$). However, the more clinically relevant paediatric head phantom pCT image is more difficult to estimate in terms of expected treatment planning benefit. While the double- and single-sided imaging setups are comparable to one another, the distribution and spread of mean RSP value in their respective voxels are a mix of different WEPL affecting the accuracy of the voxel mean RSP, particularly of those at high gradient regions. There is in other words an observed interplay effect between spatial resolution and RSP accuracy. How this will impact the treatment planning should be subject to future investigations aimed at performing and comparing treatment plans based on various imaging modalities and their resulting dose distributions. While beyond the scale of this thesis work, the MC framework and reconstructed pCT images from the simulations can be used to plan and also perform treatment plans made with treatment planning software (for instance by using the open source treatment planning tool, matRad [116]). The MC framework can also readily be updated with fu-

ture detector upgrades, e.g. the Bergen pCT collaboration plans in 2025 to replace the tracker pairs in the DTC with two ultra-thin sensors only 40 μm thick that will reduce the material budget and scattering in the trackers. Although the DTC is intended as a single-sided proton imaging setup, it is possible to include a front tracker pair and use the MC framework in this thesis investigate techniques for matching hits between front and rear tracker pairs that will effectively improve MLP estimations.

Iterative pCT reconstruction algorithms are often the preferred method for pCT, and in this thesis work we had remote access to the iterative DROP-TVS pCT reconstruction algorithm on the Kodiak computer cluster at Baylor university, and experienced users in house to run the code and reconstruct pCT images. The DROP-TVS reconstruction algorithm has been reported to accurately reconstruct high quality pCT images with the settings applied in this thesis work [21, 79, 106]. There are however optimization potential and ongoing efforts in terms of changing the DROP-TVS parameters (relaxation parameter and number of iterations) that could improve the image quality. There is also interest in fast FBP based reconstruction algorithms due to their reduced computational cost and shorter reconstruction times compared to iterative reconstruction algorithms. A recent comparison of some direct reconstruction algorithms is available in the work by Khellaf et al. [117] and report good RSP accuracy and spatial resolution for FBP based reconstructions. As the proton CT data outputted from the MC framework can easily be formatted, and the DROP-TVS can just as easily be exchanged with a different pCT reconstruction algorithm during the pCT reconstruction step, the MC framework calculated proton data can be applied to future pCT algorithms potentially showing reduced reconstruction time and/or improved image quality.

The investigations and insights obtained over the course of this thesis work have revolved around the scattering of protons. And it has been observed that the main limiting factor in pRad is not necessarily the MLP estimation, or experimental setups like energy detector or tracker technology, but rather the inherent scattering of protons in matter. While MLP estimation is necessary to improve image quality in pRad, it has been seen in this thesis work and the work by Volz et al. [115] that an improvement in MLP does not necessarily mean an equal improvement in image quality. The unavoidable effect of proton scattering will set a limit on the spatial resolution obtained by the detector and the applied techniques by spreading the energy-loss information over a rel-

atively wide lateral area depending on the amount of scattering. Since the amount of scattering depends on the energy and amount of material traversed, the image quality is dependent on the initial energy and phantom size, and reduced spatial resolution and increased noise is expected with increasing phantom size. Only standardized Catphan phantoms were implemented in pCT simulations since they are frequently used in studies to quantify image quality, but future studies can modify these phantoms to increase the amount of material and observe their impact on image quality and spatial resolution.

Multiple upcoming studies are comparing X-ray CT, Dual Energy CT (DECT), proton CT and also helium CT images intended for use in treatment planning. While DECT and pCT are comparable in terms of RSP accuracy, proton CT has the benefit of reduced dose to the patient, in the case of a pCT head scan it is reported that the dose is approximately 10 times less than a low-dose SECT of a head phantom [118], and approximately 20 times less than DECT [12].

While reduction of margins in treatment planning and more accurate localization of the Bragg peak is a worthwhile pursuit, it has been argued in the work by [119] that even though the Bragg peak and position of the Bragg peak is blurred out by the uncertainties involved (range uncertainty, positioning and anatomical changes in the patient), considerable clinical benefits when proton therapy is applicable will still remain. It can also be argued that even with perfect RSP information of the patient, the proton scattering and range is still an inherently stochastic process that will always affect the range and Bragg peak of the proton. More studies into the quality of proton imaging and the reconstructed image impact on treatment plans should be performed to better understand the benefit and shortcomings of proton imaging, or to develop new methods combining proton imaging with other imaging modalities such as SECT or DECT to improve treatment planning.

Bibliography

[1] Particle Therapy Co-Operative Group. Statistics of patients treated in particle therapy facilities worldwide. https://www.ptcog.ch/index.php/patient-statistics, May 2020 (accessed June 14, 2020). 1.1

[2] Particle Therapy Co-Operative Group. Particle therapy facilities in clinical operation. https://www.ptcog.ch/index.php/facilities-in-operation, May 2019 (accessed June 14, 2020). 1.1

[3] Francesco Dionisi and Edgar Ben-Josef. The use of proton therapy in the treatment of gastrointestinal cancers: Liver. *The Cancer Journal*, 20(6):371–377, 2014. ISSN 1528-9117. doi: 10.1097/PPO.0000000000000082. (i)

[4] Jonathan E Leeman, Paul B Romesser, Ying Zhou, Sean McBride, Nadeem Riaz, Eric Sherman, Marc A Cohen, Oren Cahlon, and Nancy Lee. Proton therapy for head and neck cancer: expanding the therapeutic window. *The Lancet Oncology*, 18(5):e254–e265, May 2017. ISSN 14702045. doi: 10.1016/S1470-2045(17)30179-1. (i), 1.1

[5] Jack Valentin, editor. *Relative biological effectiveness (RBE), quality factor (Q), and radiation weighting factor*. Number 33,4 in Annals of the ICRP. Pergamon Pr, Oxford, 2003. ISBN 978-0-08-044311-9. OCLC: 249368811. (ii)

[6] Harald Paganetti and Hanne Kooy. Proton radiation in the management of localized cancer. *Expert Review of Medical Devices*, 7(2):275–285, March 2010. ISSN 1743-4440, 1745-2422. doi: 10.1586/erd.10.2. (iii)

[7] Harald Paganetti. Range uncertainties in proton therapy and the role of Monte Carlo simulations. *Physics in Medicine and Biology*, 57(11):R99–R117, June 2012. ISSN 0031-9155, 1361-6560. doi: 10.1088/0031-9155/57/11/R99. 1.1, 1.2.2

[8] B Schaffner and E Pedroni. The precision of proton range calculations in proton radiotherapy treatment planning: experimental verification of the relation between CT-HU and proton stopping power. *Phys. Med. Biol.*, 43(6):1579–1592, June 1998. ISSN 0031-9155, 1361-6560. doi: 10.1088/0031-9155/43/6/016. 1.1

[9] Ming Yang, X Ronald Zhu, Peter C Park, Uwe Titt, Radhe Mohan, Gary Virshup, James E Clayton, and Lei Dong. Comprehensive analysis of proton range uncertainties related to patient stopping-power-ratio estimation using the stoichiometric calibration. *Phys. Med. Biol.*, 57(13):4095–4115, July 2012. ISSN 0031-9155, 1361-6560. doi: 10.1088/0031-9155/57/13/4095. 1.1

[10] G Poludniowski, N M Allinson, and P M Evans. Proton radiography and tomography with application to proton therapy. *The British Journal of Radiology*, 88(1053):20150134, September 2015. ISSN 0007-1285, 1748-880X. doi: 10.1259/bjr.20150134. 1.1, 2

[11] David C. Hansen, Joao Seco, Thomas Sangild Sørensen, Jørgen Breede Baltzer Petersen, Joachim E. Wildberger, Frank Verhaegen, and Guillaume Landry. A simulation study on proton computed tomography (CT) stopping power accuracy using dual energy CT scans as benchmark. *Acta Oncologica*, 54(9):1638–1642, October 2015. ISSN 0284-186X, 1651-226X. doi: 10.3109/0284186X.2015.1061212. 1.1

[12] George Dedes, Jannis Dickmann, Katharina Niepel, Philipp Wesp, Robert P Johnson, Mark Pankuch, Vladimir Bashkirov, Simon Rit, Lennart Volz, Reinhard W Schulte, Guillaume Landry, and Katia Parodi. Experimental comparison of proton CT and dual energy x-ray CT for relative stopping power estimation in proton therapy. *Phys. Med. Biol.*, 64(16):165002, August 2019. ISSN 1361-6560. doi: 10.1088/1361-6560/ab2b72. 1.1, 6.2

[13] Uwe Schneider, Peter Pemler, Jürgen Besserer, Eros Pedroni, Antony Lomax, and Barbara Kaser-Hotz. Patient specific optimization of the relation between CT-Hounsfield units and proton stopping power with proton radiography: Patient specific CT calibration with proton radiography. *Medical Physics*, 32(1):195–199, December 2004. ISSN 00942405. doi: 10.1118/1.1833041. 1.1

[14] Charles-Antoine Collins-Fekete, Sébastien Brousmiche, David C Hansen, Luc Beaulieu, and Joao Seco. Pre-treatment patient-specific stopping power by combining list-mode proton radiography and x-ray CT. *Physics in Medicine & Biology*, 62(17):6836–6852, August 2017. ISSN 1361-6560. doi: 10.1088/1361-6560/aa7c42. 1.1, 5.5.4

[15] N Krah, V Patera, S Rit, A Schiavi, and I Rinaldi. Regularised patient-specific stopping power calibration for proton therapy planning based on proton radiographic images. *Phys. Med. Biol.*, 64(6):065008, March 2019. ISSN 1361-6560. doi: 10.1088/1361-6560/ab03db. 1.1, 5.5.4

[16] Uwe Schneider, Eros Pedroni, and Antony Lomax. The calibration of CT Hounsfield units for radiotherapy treatment planning. *Physics in Medicine and Biology*, 41(1):111–124, January 1996. ISSN 0031-9155, 1361-6560. doi: 10.1088/0031-9155/41/1/009. 1.1

[17] Vicki Trier Taasti, Ludvig Paul Muren, Kenneth Jensen, Jørgen Breede Baltzer Petersen, Jesper Thygesen, Anna Tietze, Cai Grau, and David Christoffer Hansen. Comparison of single and dual energy CT for stopping power determination in proton therapy of head and neck cancer. *Physics and Imaging in Radiation Oncology*, 6:14–19, April 2018. ISSN 24056316. doi: 10.1016/j.phro.2018.04.002. 1.1

[18] Robert P Johnson. Review of medical radiography and tomography with proton beams. *Reports on Progress in Physics*, 81(1):016701, November 2017. ISSN 0034-4885, 1361-6633. doi: 10.1088/1361-6633/aa8b1d. 1.1, 2

[19] Johan Alme, Gábor Barnaföldi Gergely, Rene Barthel, Vyacheslav Borshchov, and et al. A high-granularity digital tracking calorimeter optimized for proton ct. *Frontiers in Physics, section Medical Physics and Imaging*, 2020. Manuscript accepted for publication. 1.1, 1.1, 2.2, 2.7, 3.4

[20] Michela Esposito, Chris Waltham, Jonathan T. Taylor, Sam Manger, Ben Phoenix, and et al. PRaVDA: The first solid-state system for proton computed tomography. *Physica Medica*, 55:149–154, November 2018. ISSN 11201797. doi: 10.1016/j.ejmp.2018.10.020. 1.1, 1.1

[21] Valentina Giacometti, Vladimir A. Bashkirov, Pierluigi Piersimoni, Susanna Guatelli, Tia E. Plautz, and et al. Software platform for simulation of a prototype proton CT scanner. *Medical Physics*, 44(3):1002–1016, March 2017. ISSN 00942405. doi: 10.1002/mp.12107. 1.1, 2.5, 6.2

[22] P. Piersimoni, J. Ramos-Méndez, T. Geoghegan, V. A. Bashkirov, R. W. Schulte, and B. A. Faddegon. The effect of beam purity and scanner complexity on proton CT accuracy. *Medical Physics*, 44(1):284–298, January 2017. ISSN 00942405. doi: 10.1002/mp.12013. 1.1

[23] Tia E. Plautz, V. Bashkirov, V. Giacometti, R. F. Hurley, R. P. Johnson, P. Piersimoni, H. F.-W. Sadrozinski, R. W. Schulte, and A. Zatserklyaniy. An evaluation of spatial resolution of a prototype proton CT scanner: Spatial resolution of a prototype proton CT scanner. *Med. Phys.*, 43(12):6291–6300, November 2016. ISSN 00942405. doi: 10.1118/1.4966028. 1.1

[24] C Bopp, R Rescigno, M Rousseau, and D Brasse. The impact of tracking system properties on the most likely path estimation in proton CT. *Physics in Medicine and Biology*, 59(23):N197–N210, December 2014. ISSN 0031-9155, 1361-6560. doi: 10.1088/0031-9155/59/23/N197. 1, 2.1, 5.5.1

[25] M. Bucciantonio, U. Amaldi, R. Kieffer, F. Sauli, and D. Watts. Development of a fast proton range radiography system for quality assurance in hadrontherapy. *Nuclear Instruments and Methods in Physics Research Section A: Accelerators, Spectrometers, Detectors and Associated Equipment*, 732:564–567, December 2013. ISSN 01689002. doi: 10.1016/j.nima.2013.05.110. 1.1

[26] M. Scaringella, M. Brianzi, M. Bruzzi, M. Bucciolini, M. Carpinelli, and et al. The PRIMA (PRoton IMAging) collaboration: Development of a proton Computed Tomography apparatus. *Nuclear Instruments and Methods in Physics Research Section A: Accelerators, Spectrometers, Detectors and Associated Equipment*, 730:178–183, December 2013. ISSN 01689002. doi: 10.1016/j.nima.2013.05.181. 1.1

[27] S.N. Penfold, A.B. Rosenfeld, R.W. Schulte, and H.-F.W. Sadrozinksi. Geometrical optimization of a particle tracking system for proton computed tomography. *Radiation Measurements*, 46(12):2069–2072, December 2011. ISSN 13504487. doi: 10.1016/j.radmeas.2011.04.032. 1.1

[28] M. Tanabashi, K. Hagiwara, K. Hikasa, K. Nakamura, Y. Sumino, and et al. Review of Particle Physics. *Phys. Rev. D*, 98(3):1898, August 2018. ISSN 2470-0010, 2470-0029. doi: 10.1103/PhysRevD.98.030001. 1.2, 1.2.1

[29] Wayne D Newhauser and Rui Zhang. The physics of proton therapy. *Physics in Medicine and Biology*, 60(8):R155–R209, April 2015. ISSN 0031-9155, 1361-6560. doi: 10.1088/0031-9155/60/8/R155. 1.2.1, 1.2.2

[30] Alfredo Ferrari, Paola R. Sala, Alberto Fasso, and Johannes Ranft. Fluka: a multi-particle transport code. *CERN 2005-10, INFN/TC_05/11, SLAC-R-773*, 55 (99):100, 2005. 1.2, 4.2

[31] Giuseppe Battistoni, Till Boehlen, Francesco Cerutti, Pik Wai Chin, Luigi Salvatore Esposito, and et al. Overview of the FLUKA code. *Annals of Nuclear Energy*, 82:10–18, August 2015. ISSN 03064549. doi: 10.1016/j.anucene.2014.11.007. 1.2, 1.3, 4.2

[32] Vasilis Vlachoudis. FLAIR: a powerful but user friendly graphical interface for FLUKA. volume 1, page 3, 2009. 1.2, 1.3, 4.2

[33] K M Hanson, J N Bradbury, T M Cannon, R L Hutson, D B Laubacher, R J Macek, M A Paciotti, and C A Taylor. Computed tomography using proton energy loss. *Physics in Medicine and Biology*, 26(6):965–983, November 1981. ISSN 0031-9155, 1361-6560. doi: 10.1088/0031-9155/26/6/001. 1.2.2

[34] N Arbor, D Dauvergne, G Dedes, J M Létang, K Parodi, C T Quiñones, E Testa, and S Rit. Monte Carlo comparison of x-ray and proton CT for range calculations of proton therapy beams. *Phys. Med. Biol.*, 60(19):7585–7599, October 2015. ISSN 0031-9155, 1361-6560. doi: 10.1088/0031-9155/60/19/7585. 1.2.2, 1.2.2

[35] R. F. Hurley, R. W. Schulte, V. A. Bashkirov, A. J. Wroe, A. Ghebremedhin, H. F.-W. Sadrozinski, V. Rykalin, G. Coutrakon, P. Koss, and B. Patyal. Water-equivalent path length calibration of a prototype proton CT scanner: Water-equivalent path length calibration for proton CT. *Med. Phys.*, 39(5):2438–2446, April 2012. ISSN 00942405. doi: 10.1118/1.3700173. 1.2.2

[36] W. H. Bragg and R. Kleeman. XXXIX. on the α particles of radium, and their loss of range in passing through various atoms and molecules. *The London, Edinburgh, and Dublin Philosophical Magazine and Journal of Science*, 10 (57):318–340, September 1905. ISSN 1941-5982, 1941-5990. doi: 10.1080/14786440509463378. 1.2.2

[37] Rui Zhang, Phillip J Taddei, Markus M Fitzek, and Wayne D Newhauser. Water equivalent thickness values of materials used in beams of protons, helium, carbon and iron ions. *Physics in Medicine and Biology*, 55(9):2481–2493, May 2010. ISSN 0031-9155, 1361-6560. doi: 10.1088/0031-9155/55/9/004. 1.2.2, 4.4

[38] Y. Kumazaki, T. Akagi, T. Yanou, D. Suga, Y. Hishikawa, and T. Teshima. Determination of the mean excitation energy of water from proton beam ranges. *Radiation Measurements*, 42(10):1683–1691, November 2007. ISSN 13504487. doi: 10.1016/j.radmeas.2007.10.019. 1.2.2

[39] S Jan, G Santin, D Strul, S Staelens, K Assié, and et al. GATE: a simulation toolkit for PET and SPECT. *Physics in Medicine and Biology*, 49(19):4543–4561, October 2004. ISSN 0031-9155, 1361-6560. doi: 10.1088/0031-9155/49/19/007. 1.2.3, 1.3, 3.1

[40] S Jan, D Benoit, E Becheva, T Carlier, F Cassol, and et al. GATE V6: a major enhancement of the GATE simulation platform enabling modelling of CT and

radiotherapy. *Phys. Med. Biol.*, 56(4):881–901, February 2011. ISSN 0031-9155, 1361-6560. doi: 10.1088/0031-9155/56/4/001. 1.2.3, 1.3, 3.1

[41] Gert Moliere. Theorie der Streuung schneller geladener Teilchen I. Einzelstreuung am abgeschirmten Coulomb-Feld. *Zeitschrift für Naturforschung A*, 2(3):133–145, March 1947. ISSN 1865-7109, 0932-0784. doi: 10.1515/zna-1947-0302. 1.2.3

[42] Gert Moliere. Theorie der Streuung schneller geladener Teilchen II Mehrfach- und Vielfachstreuung. *Zeitschrift für Naturforschung A*, 3(2):78–97, February 1948. ISSN 1865-7109, 0932-0784. doi: 10.1515/zna-1948-0203. 1.2.3

[43] Bernard Gottschalk. Techniques of proton radiotherapy: transport theory. *arXiv preprint arXiv:1204.4470*, 2012. 1.2.3, 1.2.3, 2.4

[44] Bruno Rossi and Kenneth Greisen. Cosmic-Ray Theory. *Rev. Mod. Phys.*, 13(4):240–309, October 1941. ISSN 0034-6861. doi: 10.1103/RevModPhys.13.240. 1.2.3

[45] Leonard Eyges. Multiple Scattering with Energy Loss. *Physical Review*, 74(10):1534–1535, November 1948. ISSN 0031-899X. doi: 10.1103/PhysRev.74.1534. 1.2.3

[46] Bernard Gottschalk. On the scattering power of radiotherapy protons: Scattering power of radiotherapy protons. *Medical Physics*, 37(1):352–367, December 2009. ISSN 00942405. doi: 10.1118/1.3264177. 1.2.3, 1.2.3

[47] Nobuyuki Kanematsu. Alternative scattering power for Gaussian beam model of heavy charged particles. *Nuclear Instruments and Methods in Physics Research Section B: Beam Interactions with Materials and Atoms*, 266(23):5056–5062, December 2008. ISSN 0168583X. doi: 10.1016/j.nimb.2008.09.004. 1.2.3

[48] H Paganetti. Nuclear interactions in proton therapy: dose and relative biological effect distributions originating from primary and secondary particles. *Phys. Med. Biol.*, 47(5):747–764, March 2002. ISSN 0031-9155, 1361-6560. doi: 10.1088/0031-9155/47/5/305. 1.2.4

[49] Alex F Bielajew. Fundamentals of the Monte Carlo method for neutral and charged particle transport. *The University of Michigan*, 2001. 1.3

[50] George Dedes, Jannis Dickmann, Valentina Giacometti, Simon Rit, Nils Krah, Sebastian Meyer, Vladimir Bashkirov, Reinhard Schulte, Robert P. Johnson, Katia Parodi, and Guillaume Landry. The role of Monte Carlo simulation in understanding the performance of proton computed tomography. *Zeitschrift für Medizinische Physik*, page S0939388920300659, August 2020. ISSN 09393889. doi: 10.1016/j.zemedi.2020.06.006. 1.3

[51] S. Agostinelli, J. Allison, K. Amako, J. Apostolakis, H. Araujo, and et al. Geant4—a simulation toolkit. *Nuclear Instruments and Methods in Physics Research Section A: Accelerators, Spectrometers, Detectors and Associated Equipment*, 506(3):250–303, July 2003. ISSN 01689002. doi: 10.1016/S0168-9002(03)01368-8. 1.3, 3.1

[52] J. Allison, K. Amako, J. Apostolakis, H. Araujo, P. Arce Dubois, and et al. Geant4 developments and applications. *IEEE Trans. Nucl. Sci.*, 53(1):270–278, February 2006. ISSN 0018-9499. doi: 10.1109/TNS.2006.869826. 1.3, 3.1

[53] T.T. Böhlen, F. Cerutti, M.P.W. Chin, A. Fassò, A. Ferrari, P.G. Ortega, A. Mairani, P.R. Sala, G. Smirnov, and V. Vlachoudis. The FLUKA Code: Developments and Challenges for High Energy and Medical Applications. *Nuclear Data Sheets*, 120:211–214, June 2014. ISSN 00903752. doi: 10.1016/j.nds.2014.07.049. 1.3

[54] A. M. Cormack. Representation of a Function by Its Line Integrals, with Some Radiological Applications. *Journal of Applied Physics*, 34(9):2722–2727, September 1963. ISSN 0021-8979, 1089-7550. doi: 10.1063/1.1729798. 2

[55] Tianfang Li, Zhengrong Liang, Jayalakshmi V. Singanallur, Todd J. Satogata, David C. Williams, and Reinhard W. Schulte. Reconstruction for proton computed tomography by tracing proton trajectories: A Monte Carlo study: Proton CT reconstruction by tracing internal paths. *Medical Physics*, 33(3):699–706, February 2006. ISSN 00942405. doi: 10.1118/1.2171507. 2, 2.3, 2.3.2, 2.5

[56] N Krah, F Khellaf, J M Létang, S Rit, and I Rinaldi. A comprehensive theoretical comparison of proton imaging set-ups in terms of spatial resolution. *Physics in Medicine & Biology*, 63(13):135013, July 2018. ISSN 1361-6560. doi: 10.1088/1361-6560/aaca1f. 2.1, 2.2, 2.3, 2.3, 2.3.1, 2.6, 3.2, 5.1, 5.5.1, 5.5.5, C

[57] J. Krimmer, D. Dauvergne, J.M. Létang, and É. Testa. Prompt-gamma monitoring in hadrontherapy: A review. *Nuclear Instruments and Methods in Physics Research Section A: Accelerators, Spectrometers, Detectors and Associated Equipment*, 878:58–73, January 2018. ISSN 01689002. doi: 10.1016/j.nima.2017.07.063. 2.2

[58] Uwe Schneider and Eros Pedroni. Multiple Coulomb scattering and spatial resolution in proton radiography. *Medical Physics*, 21(11):1657–1663, November 1994. ISSN 00942405. doi: 10.1118/1.597212. 2.3

[59] D. C. Williams. The most likely path of an energetic charged particle through a uniform medium. *Physics in Medicine and Biology*, 49(13):2899–2911, July 2004. ISSN 0031-9155, 1361-6560. doi: 10.1088/0031-9155/49/13/010. 2.3, 2.3

[60] R. W. Schulte, S. N. Penfold, J. T. Tafas, and K. E. Schubert. A maximum likelihood proton path formalism for application in proton computed tomography: Maximum likelihood path formalism for proton CT. *Medical Physics*, 35(11):4849–4856, October 2008. ISSN 00942405. doi: 10.1118/1.2986139. 2.3, 2.3, 2.3.2, 2.4, 5.1, 5.2, 5.4, 5.5.1

[61] B Erdelyi. A comprehensive study of the most likely path formalism for proton-computed tomography. *Physics in Medicine and Biology*, 54(20):6095–6122, October 2009. ISSN 0031-9155, 1361-6560. doi: 10.1088/0031-9155/54/20/005. 2.3

[62] Charles-Antoine Collins-Fekete, Lennart Volz, Stephen K N Portillo, Luc Beaulieu, and Joao Seco. A theoretical framework to predict the most likely ion path in particle imaging. *Physics in Medicine and Biology*, 62(5):1777–1790, March 2017. ISSN 0031-9155, 1361-6560. doi: 10.1088/1361-6560/aa58ce. 2.3

[63] K. Wong and B. Erdelyi. Accuracy of the Most Likely Path Formalism in Inhomogeneous Phantoms. *Nuclear Technology*, 175(1):40–47, July 2011. ISSN 0029-5450, 1943-7471. doi: 10.13182/NT11-A12267. 2.3, 5.5.4

[64] Charles-Antoine Collins-Fekete, Esther Bär, Lennart Volz, Hugo Bouchard, Luc Beaulieu, and Joao Seco. Extension of the Fermi–Eyges most-likely path in heterogeneous medium with prior knowledge information. *Physics in Medicine & Biology*, 62(24):9207–9219, November 2017. ISSN 1361-6560. doi: 10.1088/1361-6560/aa955d. 2.3, 5.5.4

[65] Mark Brooke and Scott Penfold. An inhomogeneous most likely path formalism for proton computed tomography. *arXiv:1808.00122 [physics]*, July 2018. arXiv: 1808.00122. 2.3, 5.5.4

[66] Blake Schultze, Micah Witt, Yair Censor, Reinhard Schulte, and Keith Evan Schubert. Performance of hull-detection algorithms for proton computed tomography reconstruction. *Contemporary Mathematics*, 636:211–224, 2015. 2.3

[67] The Particle Data Group (PDG). Atomic and nuclear properties of materials for more than 300 materials. https://pdg.lbl.gov/2009/AtomicNuclearProperties/, September 2020 (accessed September 10, 2020). 2.3

[68] Gerald R. Lynch and Orin I. Dahl. Approximations to multiple Coulomb scattering. *Nuclear Instruments and Methods in Physics Research Section B: Beam Interactions with Materials and Atoms*, 58(1):6–10, May 1991. ISSN 0168583X. doi: 10.1016/0168-583X(91)95671-Y. 2.3.1

[69] Charles-Antoine Collins-Fekete, Paul Doolan, Marta F Dias, Luc Beaulieu, and Joao Seco. Developing a phenomenological model of the proton trajectory within a heterogeneous medium required for proton imaging. *Phys. Med. Biol.*, 60(13): 5071–5082, July 2015. ISSN 0031-9155, 1361-6560. doi: 10.1088/0031-9155/60/13/5071. 2.3.2, 2.3.2, 2.5

[70] David C. Hansen, Jørgen Breede Baltzer Petersen, Niels Bassler, and Thomas Sangild Sørensen. Improved proton computed tomography by dual modality image reconstruction: Improved proton computed tomography by dual modality reconstruction. *Medical Physics*, 41(3):031904, February 2014. ISSN 00942405. doi: 10.1118/1.4864239. URL http://doi.wiley.com/10.1118/1.4864239. 2.3.2

[71] Charles-Antoine Collins-Fekete, Sébastien Brousmiche, Stephen K N Portillo, Luc Beaulieu, and Joao Seco. A maximum likelihood method for high resolution proton radiography/proton CT. *Physics in Medicine and Biology*, 61(23):8232–8248, December 2016. ISSN 0031-9155, 1361-6560. doi: 10.1088/0031-9155/61/23/8232. 2.4, 2.3, 2.6, 3.2, 5.3, 5.5.3, 5.5.3, C, D.1

[72] Reinhard W. Schulte, Vladimir Bashkirov, Márgio C. Loss Klock, Tianfang Li, Andrew J. Wroe, Ivan Evseev, David C. Williams, and Todd Satogata. Density resolution of proton computed tomography. *Med. Phys.*, 32(4):1035–1046, March 2005. ISSN 00942405. doi: 10.1118/1.1884906. 2.4

[73] Lennart Volz, Pierluigi Piersimoni, Robert P Johnson, Vladimir A Bashkirov, Reinhard W Schulte, and Joao Seco. Improving single-event proton CT by removing nuclear interaction events within the energy/range detector. *Phys. Med. Biol.*, 64(15):15NT01, August 2019. ISSN 1361-6560. doi: 10.1088/1361-6560/ab2671. 2.4

[74] Simon Rit, George Dedes, Nicolas Freud, David Sarrut, and Jean Michel Létang. Filtered backprojection proton CT reconstruction along most likely paths: FBP proton CT reconstruction along most likely paths. *Med. Phys.*, 40(3):031103, February 2013. ISSN 00942405. doi: 10.1118/1.4789589. 2.5, 5.5.3

[75] G Poludniowski, N M Allinson, and P M Evans. Proton computed tomography reconstruction using a backprojection-then-filtering approach. *Phys. Med. Biol.*, 59(24):7905–7918, December 2014. ISSN 0031-9155, 1361-6560. doi: 10.1088/0031-9155/59/24/7905. 2.5

[76] Scott Penfold and Yair Censor. Techniques in Iterative Proton CT Image Reconstruction. *Sensing and Imaging*, 16(1), December 2015. ISSN 1557-2064, 1557-2072. doi: 10.1007/s11220-015-0122-3. 2.5

[77] S. N. Penfold, R. W. Schulte, Y. Censor, and A. B. Rosenfeld. Total variation superiorization schemes in proton computed tomography image reconstruction: Total variation superiorization in proton CT. *Medical Physics*, 37(11):5887–5895, October 2010. ISSN 00942405. doi: 10.1118/1.3504603. 2.5, 5.4

[78] Blake Schultze, Yair Censor, Paniz Karbasi, Keith E. Schubert, and Reinhard W. Schulte. An Improved Method of Total Variation Superiorization Applied to Reconstruction in Proton Computed Tomography. *IEEE Trans. Med. Imaging*, 39(2):294–307, February 2020. ISSN 0278-0062, 1558-254X. doi: 10.1109/TMI.2019.2911482. 2.5

[79] Pierluigi Piersimoni, Bruce A. Faddegon, José Ramos Méndez, Reinhard W. Schulte, Lennart Volz, and Joao Seco. Helium CT: Monte Carlo simulation results for an ideal source and detector with comparison to proton CT. *Med. Phys.*, 45(7):3264–3274, July 2018. ISSN 0094-2405, 2473-4209. doi: 10.1002/mp.12942. 2.5, 2.6, 3.2, 6.2

[80] Joao Seco, Michael Oumano, Nicolas Depauw, Marta F. Dias, Rui P. Teixeira, and Maria F. Spadea. Characterizing the modulation transfer function (MTF) of proton/carbon radiography using Monte Carlo simulations: Characterizing MTF for proton/carbon radiography. *Med. Phys.*, 40(9):091717, September 2013. ISSN 00942405. doi: 10.1118/1.4819816. 2.6

[81] H.E.S. Pettersen, J. Alme, A. Biegun, A. van den Brink, M. Chaar, and et al. Proton tracking in a high-granularity Digital Tracking Calorimeter for proton CT

purposes. *Nuclear Instruments and Methods in Physics Research Section A: Accelerators, Spectrometers, Detectors and Associated Equipment*, 860:51–61, July 2017. ISSN 0168-9002. doi: 10.1016/j.nima.2017.02.007. 2.7

[82] M. Mager. ALPIDE, the Monolithic Active Pixel Sensor for the ALICE ITS upgrade. *Nuclear Instruments and Methods in Physics Research Section A: Accelerators, Spectrometers, Detectors and Associated Equipment*, 824:434–438, July 2016. ISSN 01689002. doi: 10.1016/j.nima.2015.09.057. 2.7, 4.5.2, 4.6, 4.6

[83] Gianluca Aglieri Rinella. The ALPIDE pixel sensor chip for the upgrade of the ALICE Inner Tracking System. *Nuclear Instruments and Methods in Physics Research Section A: Accelerators, Spectrometers, Detectors and Associated Equipment*, May 2016. ISSN 01689002. doi: 10.1016/j.nima.2016.05.016. 2.7

[84] Helge Egil Seime Pettersen, Johan Alme, Gergely Gábor Barnaföldi, Rene Barthel, Anthony van den Brink, and et al. Design optimization of a pixel-based range telescope for proton computed tomography. *Physica Medica*, 63:87–97, July 2019. ISSN 11201797. doi: 10.1016/j.ejmp.2019.05.026. 2.7, 3.5.2, 3.6

[85] Rene Brun and Fons Rademakers. ROOT — An object oriented data analysis framework. *Nuclear Instruments and Methods in Physics Research Section A: Accelerators, Spectrometers, Detectors and Associated Equipment*, 389(1-2):81–86, April 1997. ISSN 01689002. doi: 10.1016/S0168-9002(97)00048-X. 3

[86] Anton V. Ivantchenko, Vladimir N. Ivanchenko, Jose-Manuel Quesada Molina, and Sebastien L. Incerti. Geant4 hadronic physics for space radiation environment. *International Journal of Radiation Biology*, 88(1-2):171–175, January 2012. ISSN 0955-3002, 1362-3095. doi: 10.3109/09553002.2011.610865. 3.1, 3.1

[87] Vladimir Ivanchenko, Paolo Dondero, Valentina Fioretti, Anton Ivantchenko, Fan Lei, Simone Lotti, Alfonso Mantero, and Teresa Mineo. Validation of geant4 10.3 simulation of proton interaction for space radiation effects. *Exp Astron*, 44(3):437–450, December 2017. ISSN 0922-6435, 1572-9508. doi: 10.1007/s10686-017-9556-z. 3.1

[88] GEANT4 collaboration. *Physics List Guide*, 2020 (accessed July 5, 2020). URL http://geant4-userdoc.web.cern.ch/geant4-userdoc/UsersGuides/PhysicsListGuide/html/physicslistguide.html. 3.1

[89] GEANT4 collaboration. *Step-size Limit*, 2020 (accessed July 5, 2020). URL http://geant4-userdoc.web.cern.ch/geant4-userdoc/UsersGuides/PhysicsReferenceManual/html/electromagnetic/energy_loss/enloss.html#drover-range. 3.1, 3.1

[90] GEANT4 collaboration. *Electromagnetic standard - option 4 (EMZ)*, 2020 (accessed August 10, 2020). URL http://geant4-userdoc.web.cern.ch/geant4-userdoc/UsersGuides/PhysicsListGuide/html/electromagnetic/tables_by_constructor/opt4.html. 3.1

[91] GEANT4 collaboration. *Physics Reference Manual*, 2020 (accessed July 5, 2020). URL http://geant4-userdoc.web.cern.ch/geant4-userdoc/UsersGuides/PhysicsReferenceManual/html/index.html. 3.1

[92] Christian Schoemers, Eike Feldmeier, Jakob Naumann, Ralf Panse, Andreas Peters, and Thomas Haberer. The intensity feedback system at Heidelberg Ion-Beam Therapy Centre. *Nuclear Instruments and Methods in Physics Research Section A: Accelerators, Spectrometers, Detectors and Associated Equipment*, 795:92–99, September 2015. ISSN 01689002. doi: 10.1016/j.nima.2015.05.054. 3.2, 5.5.2

[93] L Grevillot, D Bertrand, F Dessy, N Freud, and D Sarrut. A Monte Carlo pencil beam scanning model for proton treatment plan simulation using GATE/GEANT4. *Physics in Medicine and Biology*, 56(16):5203–5219, August 2011. ISSN 0031-9155, 1361-6560. doi: 10.1088/0031-9155/56/16/008. 3.2, 3.6, A.1

[94] R.P. Johnson, V.A. Bashkirov, G. Coutrakon, V. Giacometti, P. Karbasi, N.T. Karonis, C.E. Ordoñez, M. Pankuch, H.F.-W. Sadrozinski, K.E. Schubert, and R.W. Schulte. Results from a Prototype Proton-CT Head Scanner. *Physics Procedia*, 90:209–214, 2017. ISSN 18753892. doi: 10.1016/j.phpro.2017.09.060. 3.2

[95] Incorporated The Phantom Laboratory. *Catphan® 412-424 Manual*. The Phantom Laboratory, Incorporated, The Phantom Laboratory, P.O. Box 511, Salem, NY, 12865-0511 USA, 1 edition, 4 2005. 3.2

[96] Incorporated The Phantom Laboratory. *Catphan® 500-600 Manual*. The Phantom Laboratory, Incorporated, The Phantom Laboratory, P.O. Box 511, Salem, NY, 12865-0511 USA, 1 edition, 12 2015. 3.3

[97] V. Giacometti, S. Guatelli, M. Bazalova-Carter, A.B. Rosenfeld, and R.W. Schulte. Development of a high resolution voxelised head phantom for medical physics applications. *Physica Medica*, 33:182–188, January 2017. ISSN 11201797. doi: 10.1016/j.ejmp.2017.01.007. 3.3.4, 3.3

[98] OpenGATE collaboration. Official public repository of gate, 2017. URL https://github.com/OpenGATE/Gate. GateMaterials.db. 3.3

[99] Stephen Seltzer. Stopping-Powers and Range Tables for Electrons, Protons, and Helium Ions, NIST Standard Reference Database 124, 1993. URL http://www.nist.gov/pml/data/star/index.cfm. type: dataset. 3.3

[100] V.M. et.al. Borshchov. Innovative microelectronic technologies for high-energy physics experiments. *Funct.Mater.*, 23(4):143–153, March 2017. ISSN 10275495, 22182993. doi: 10.15407/fm24.01.143. 3.4, 3.5a

[101] H.E.S. Pettersen. *A Digital Tracking Calorimeter for Proton Computed Tomography*. Doctoral thesis, The University of Bergen, February 2018. URL hdl.handle.net/1956/17757. 3.6

[102] Thomas Tessonnier, Tiago Marcelos, Andrea Mairani, Stephan Brons, and Katia Parodi. Phase space generation for proton and carbon ion beams for external users' applications at the heidelberg ion therapy center. *Front. Oncol.*, 5, January 2016. ISSN 2234-943X. doi: 10.3389/fonc.2015.00297. 3.6

[103] Helge Egil Seime Pettersen, Lennart Volz, Jarle Rambo Sølie, Johan Alme, Gergely Gábor, and et al. Helium radiography with a digital tracking calorimeter – a monte carlo study for secondary track rejection. *Submitted to PMB*, page 27, 2020. Manuscript submitted. 3.6, 6.1

[104] Ketil Røed. *Single Event Upsets in SRAM FPGA based readout electronics for the Time Projection Chamber in the ALICE experiment*. Doctoral thesis, The University of Bergen, February 2010. URL http://hdl.handle.net/1956/3793. 4, 4.1

[105] Charles C. Foster. Total Ionizing Dose and Displacement-Damage Effects in Microelectronics. *MRS Bull.*, 28(2):136–140, February 2003. ISSN 0883-7694, 1938-1425. doi: 10.1557/mrs2003.42. 4, 4.1

[106] Robert P. Johnson, Vladimir Bashkirov, Langley DeWitt, Valentina Giacometti, Robert F. Hurley, Pierluigi Piersimoni, and et al. A Fast Experimental Scanner for Proton CT: Technical Performance and First Experience With Phantom Scans. *IEEE Transactions on Nuclear Science*, 63(1):52–60, February 2016. ISSN 0018-9499, 1558-1578. doi: 10.1109/TNS.2015.2491918. 4, 5.1, 5.2, 6.2

[107] Marta Bagatin and Simone Gerardin. *Ionizing radiation effects in electronics,: from memories to imagers*. CRC press, 2018. ISBN 9781498722636. 4.1

[108] F. Faccio and G. Cervelli. Radiation-induced edge effects in deep submicron CMOS transistors. *IEEE Trans. Nucl. Sci.*, 52(6):2413–2420, December 2005. ISSN 0018-9499. doi: 10.1109/TNS.2005.860698. 4.1

[109] CERN. *FLUKA2011.3 MANUAL - DEFAULTS*, 2020 (accessed July 6, 2020). URL https://flukafiles.web.cern.ch/flukafiles/manual/DEFAULTS.html. 4.2

[110] CERN. *FLUKA2011.3 MANUAL - USRBIN*, 2020 (accessed July 6, 2020). URL https://flukafiles.web.cern.ch/flukafiles/manual/USRBIN.html. 4.2

[111] Kine Johnsen. Simulations of a Therapeutic Proton Beam with FLUKA Monte Carlo Code and Varian Eclipse Proton Planning Software. Master's thesis, University of Bergen, November 2013. 4.4, 4.4

[112] Matteo Lupi, G. Aglieri Rinella, M. Bonora, H. Hillemanns, D. Kim, T. Kugathasan, A. Lattuca, G. Mazza, K. M. Sielewicz, and W. Snoeys. Design and Test with Proton Beam of a 1.2 Gb/s Semi-custom Serialiser Implemented in 180 nm CMOS with SEU Mitigation by TMR. In *2017 17th European Conference on Radiation and Its Effects on Components and Systems (RADECS)*, pages 1–5, Geneva, Switzerland, October 2017. IEEE. ISBN 978-1-5386-1261-3. doi: 10.1109/RADECS.2017.8696110. 4.5.1

[113] David M. Hiemstra, Valeri Kirischian, and Jakub Brelski. Single Event Upset Characterization of the Kintex UltraScale Field Programmable Gate Array Using Proton Irradiation. In *2016 IEEE Radiation Effects Data Workshop (REDW)*, pages 1–5, Portland, OR, USA, 2016. IEEE. ISBN 978-1-5090-5114-4. doi: 10.1109/NSREC.2016.7891743. 4.6

[114] S. Kushpil, F. Krizek, and A. Isakov. Recent Results From Beam Tests of the ALPIDE Pixel Chip for the Upgrade of the ALICE Inner Tracker. *IEEE Trans. Nucl. Sci.*, 66(11):2319–2323, November 2019. ISSN 0018-9499, 1558-1578. doi: 10.1109/TNS.2019.2945234. 4.6

[115] Lennart Volz, Charles-Antoine Collins-Fekete, Jarle Rambo Sølie, and Joao Seco. Theoretical considerations on the spatial resolution limit of single-event particle radiography. *Biomed. Phys. Eng. Express*, 6(5):055002, July 2020. ISSN 2057-1976. doi: 10.1088/2057-1976/ab9c3f. 5.5.3, 5.14, 5.5.3, 6.2

[116] German Cancer research center (DKFZ). Matrad - an open source multi-modality radiation treatment planning system. https://e0404.github.io/matRad/, May 2015 (accessed August 05, 2020). 6.2

[117] Feriel Khellaf, Nils Krah, Jean Michel Létang, Charles-Antoine Collins-Fekete, and Simon Rit. A comparison of direct reconstruction algorithms in proton computed tomography. *Phys. Med. Biol.*, 65(10):105010, June 2020. ISSN 1361-6560. doi: 10.1088/1361-6560/ab7d53. 6.2

[118] Valentina Giacometti. *Modelling and improvement of proton computed tomography*. PhD thesis, University of Wollongong, 2016. 6.2

[119] Antony John Lomax. Myths and realities of range uncertainty. *BJR*, 93(1107): 20190582, March 2020. ISSN 0007-1285, 1748-880X. doi: 10.1259/bjr.20190582. 6.2

List of Publications

- Pettersen HES, Chaar M, Meric I, Odland OH, **Sølie JR**, Röhrich D. *Accuracy of parameterized proton range models: a comparison*, Radiation Physics and Chemistry, 2018.

- Pettersen HES, Alme J, Barnafoldi GG, Barthel R, Brink A, Borshchov V,Chaar M, Eikeland V, Garcia-Santos A, Genov G, Grimstad S, Grøttvik O, Helstrup H, Hetland KF, Mehendale S, Meric I, Odland OH, Papp G, Peitzmann T, Piersimoni P, Rehman AU, Richter M, Samnøy AT, Tefre A, Seco J, Shafiee H, Skjæveland EV, **Sølie JR**, Tambave G, Ullaland K, Varga-Kofarago M, Volz L, Wagner B, Shiming Y, Röhrich D. *Design optimization of a pixel-based range telescope for proton computed tomography*, Physica Medica, 2019.

- **Sølie JR**, Volz L, Pettersen HES, Piersimoni P, Odland OH, Röhrich D, Helstrup H, Peitzmann T, Ullaland K, Varga-Kofarago M, Mehendale S, Grøttvik OS, Eikeland VN, Meric I and Seco J. *Image quality of list-mode proton imaging without front trackers*, Phys. Med. Biol., 2020.

- Volz L, Collins-Fekete CA, **Sølie JR**. *Theoretical considerations on the spatial resolution limit of single-event particle radiography*, Biomed. Phys. Eng. Express, 2020

- Alme J, Barnafoldi GG, Barthel R, Brink A, Borshchov V, Bodova T, Brons S, Chaar M, Eikeland V, Genov G, Grimstad S, Grøttvik O, Helstrup H, Herland A, Hilde AE, Keidel R, Kobdaj C, Kolk N, Listratenko O, Malik Q, Mehendale S, Meric I, Nesbø SV, Odland OH, Papp G, Peitzmann T, Pettersen HES, Piersimoni P, Protsenko M, Rehman AU, Richter M, Röhrich D, Samnøy AT, Seco J, Setterdahl L, Shafiee H, Skjolddal ØJ, Solheim E, Songmoolnak A, Sudár A, **Sølie JR**, Tambave G, Tymchuk I, Ullaland K, Underdal HA, Varga-Kofarago M, Volz L, Wagner B, Weigold T, Widerøe FM, Xiao R, Yang S, Yokoyama H. *A High-Granularity Digital Tracking Calorimeter Optimized for Proton CT*, Frontiers in Physics, section Medical Physics and Imaging (paper in review), 2020.

- Pettersen HES, Volz L, **Sølie JR**, Piersimoni P, Alme J, Barnafoldi GG, Barthel R, Brink A, Borshchov V,Chaar M, Eikeland V, Genov G, Grøttvik O, Helstrup H, Keidel R, Kobdaj C, Kolk N, Mehendale S, Meric I, Odland OH, Papp G, Peitzmann T, Piersimoni P, Protsenko M, Rehman AU, Richter M, Samnøy AT, Seco J, Shafiee H, Songmoolnak A, Tambave G, Tymchuk I, Ullaland K, Varga-Kofarago M, Wagner B, Xiao R, Yang S, Yokoyama H, Röhrich D. *Helium Radiography with a Digital Tracking Calorimeter – A Monte Carlo Study for Secondary Track Rejection*, Phys. Med. Biol., 2020.

Conference presentations

- **Sølie JR.** *Monte Carlo simulations of secondary neutron and proton fluence in proton CT*. Proton CT workshop, November 2016, Bergen, Norway (Oral presentation).
- **Sølie JR**, Pettersen HES, Meric I, Odland OH, Röhrich D. *A comparison of proton ranges in complex media using GATE, MCNP6 and FLUKA*. IRRMA X, July 2017, Chicago, USA (Poster).
- **Sølie JR.** *Radiation Environment in Proton Therapy and Proton CT*. Fysikermøte, August 2017, Tromsø, Norway (Oral presentation).
- **Sølie JR.** *Most Likely Path of Protons – Towards proton CT*. Faggruppemøte, September 2018, Bergen, Norway (Oral presentation).
- **Sølie JR**, Volz L. *Optimizing Single-Tracker List Mode Proton CT*. PTCOG, June 2019, Manchester, United Kingdom (Poster presentation).
- **Sølie JR.** *Removing the front tracker pair in proton CT; investigations and observations (Monte Carlo)*. 6th Annual Loma Linda Workshop, July 2020, Digital conference call (Oral presentation).

A. MC simulation settings

This appendix show some of the MC simulation commands and code snippets used to build, control, and modify the GATE and FLUKA simulations. Note that all code snippets are simplified and so not all functions are defined. For the full functional code, see the respective GitHub repositories listed in each section.

A.1 GATE simulations

The full GATE MC environment with all mentioned geometry and phantom descriptions, source descriptions, physics, and modified source files are made available at GitHub:

`https://github.com/JarleSoelie/gate_pCT`

Beam scanning

The source file `GateSourceTPSPencilBeam.cc` located in the official GATE 8.2 downloadable source folder `/gate_v8.2/source/physics/src` and the header file called `GateSourceTPSPencilBeam.hh` located in `/gate_v8.2/source/physics/include` were modified before compilation of GATE 8.2 to allow the user to control the number of protons in each beam spot using the TPS based beam scanning model by Grevillot et al. [93]. Most important is the `GateSourceTPSPencilBeam.cc` source file where lines 261-273 was exchanged with the following code:

```
mDistriGeneral=new RandGeneral(engine,mPDF,mTotalNumberOfSpots,0);
int bin=0;
if (mSortedSpotGenerationFlag){
  //number of ions to generate to be placed in each spot
  mNbIonsToGenerate.resize(mTotalNumberOfSpots,0);
  long int ntotal=GateApplicationMgr::GetInstance()->
   GetTotalNumberOfPrimaries();
  //number of protons in each spot from plan_file.txt
  int counter=mSpotWeight[0];
  for (long int i=0;i<ntotal;i++){ //for every primary
    if (!mRealisticSpotFlag){ // This is set to true above
      if(i>=counter){ //Counter is the number of protons in each spot bin
   ++;
        counter+=mSpotWeight[bin];
      }
    }
    else{
      //Chooses which spot to fire at
      bin=mTotalNumberOfSpots*mDistriGeneral->fire();
    }
```

```
    //adds up the number of ions to be simulated in each bin/spot
    ++mNbIonsToGenerate[bin];
  }
  for (int i=0;i<mTotalNumberOfSpots;i++) {
    GateMessage("Beam", 3, "[TPSPencilBeam] bin " << std::setw(5) << i <<
    ": spotweight=" << std::setw(8) << mPDF[i] << ", Ngen=" <<
    mNbIonsToGenerate[i] << Gateendl );
  }
mCurrentSpot=0;
}
```

This allows the use of an exact number of protons per beam spot (spot Weight) as listed in the `PlanDescriptionToGate.txt` file located in the same folder as the GATE main macro (`main.mac`). The beam spots are filled sequentially from the plan description file. An abbreviated example of a plan description file is shown below:

```
#TREATMENT-PLAN-DESCRIPTION
#=============PlanName and number of fields===========#
IMPT
#-----NumberOfFractions ***NOT USED***
1
#-----FractionID ***NOT USED***
1
#NumberOfFields
1
#FieldsID
1
#-----TotalMetersetWeightOfAllFields ***NOT USED***
662421

#============FIELD-DESCRIPTION=============#
#FieldID
1
#-----FinalCumulativeMeterSetWeight ***NOT USED***
336732
#GantryAngle (in degrees)
0
#-----PatientSupportAngle ***NOT USED***
0
#-----IsocenterPosition   ***NOT USED***
0 0 0
###NumberOfControlPoints
1

#===========SPOTS-DESCRIPTION===========#
####ControlPointIndex
0
####SpotTunnedID ***NOT USED***
1
####CumulativeMetersetWeight ***NOT USED***
0
###Energy (MeV)
230.0
####NbOfScannedSpots
621
####X Y WEIGHT
-91.00 77.00 15000
-84.00 77.00 15000
...
91.00 77.00 15000
91.00 70.00 15000
84.00 70.00 15000
...
-91.00 70.00 15000
-91.00 63.00 15000
-84.00 63.00 15000
```

```
    ...
    84.00 -77.00 15000
    91.00 -77.00 15000
```

To activate the TPS source and the appropriate settings for spot scanning in a single pCT projection, the main GATE simulation macro must contain the following flags and commands:

```
/gate/source/addSource protonScanning TPSPencilBeam
/gate/source/protonScanning/setParticleType proton
/gate/source/protonScanning/setPlan PlanDescriptionToGate.txt
/gate/source/protonScanning/setBeamConvergence false
/gate/source/protonScanning/setSpotIntensityAsNbIons true
/gate/source/protonScanning/setSortedSpotGenerationFlag true
/gate/source/protonScanning/setFlatGenerationFlag true
/gate/source/protonScanning/setSigmaEnergyInMeVFlag false
/gate/source/protonScanning/setSourceDescriptionFile Source-Properties.txt
```

Besides the mentioned `PlanDescriptionToGate.txt` file, the `Source-Properties.txt` is the second and final file needed for the TPS source to function as intended. The pencil beam properties used to irradiate each spot is defined inside this file. An example based on the mono-energetic 230 MeV 7 mm FWHM pencil beam is presented below:

```
# MA beam line test
# Nozzle exit to Isocenter distance
500
# SMX to Isocenter distance
6600
# SMY to Isocenter distance
6600
#========ENERGY=========#
# mean energy
# polynomial order
0
# polynomial parameters (highest to lowest)
230.0
# energy spread
# polynomial order
percent
0
# polynomial parameters (highest to lowest)
0.0
#========SPOT SIZE x y theta phi==========#
# Spot Size x [mm]
# polynomial order
0
# polynomial parameters
2.0
# Spot Divergence Theta [rad]
# polynomial order
0
# polynomial parameters
0.0025
# Spot Size y [mm]
# polynomial order
0
# polynomial parameters
2.0
# Spot Divergence Phi [rad]
# polynomial order
0
# polynomial parameters
0.0025
```

```
# SPOT emmittances
# x-theta emmittance
# polynomial order
0
# polynomial parameters
0.003
# y-phi emmittance
# polynomial order
0
# polynomial parameters
0.003
```

A.2 FLUKA simulations

The full FLUKA MC environment with all mentioned geometry and phantom descriptions, source descriptions, physics, and modified source files are made available at GitHub:

`https://github.com/JarleSoelie/fluka_pCT`

Fortran source files

The FLUKA source file (`pCT.f`) used to perform pencil beam spot scanning with a 7 mm FWHM pencil beam covering the area -8.4 cm to 8.4 cm in the longitudinal direction and -6 cm to 6 cm in the height direction with 450 spot coordinates was made by adding the following modification to the initial proton beam angle (TXFLK, TYFLK, and TZFLK) and starting positions (XFLK, YFLK, and ZFLK). The protons start from the imagined beam window located 50 cm downstream from the iso-centre and based on scanning magnets (point-source) located 660 cm downstream.

```
*Start making spot indexes and spot properties
    if(NCASE.gt.(2500*WHASOU (3))) then
    WHASOU (3)=WHASOU (3)+1
      WHASOU (1)=WHASOU (1)+1
    end if
    if(WHASOU (1).ge.(26)) then
      WHASOU (1)=1
      WHASOU (2)=WHASOU (2)+1
    end if
*  Cosines (tx,ty,tz)
    CALL FLNRR2(RGAUS1, RGAUS2)
    TXFLK  (NPFLKA) = ((-9.1 +(WHASOU (1)*0.7))/(SQRT (
      &          (-9.1 +(WHASOU (1)*0.7))**2
      &          + (-6.7 +(WHASOU (2)*0.7))**2 + 637.0**2 )))
      &          + (0.0025*RGAUS1)
    TYFLK  (NPFLKA) = ((-7.7 +(WHASOU (2)*0.7))/(SQRT (
      &          (-9.1 +(WHASOU (1)*0.7))**2
      &          + (-6.7 +(WHASOU (2)*0.7))**2 + 637.0**2 )))
      &          + (0.0025*RGAUS2)
    TZFLK  (NPFLKA) = SQRT ( ONEONE - TXFLK (NPFLKA)**2
      &          - TYFLK (NPFLKA)**2 )
*  Particle coordinates of beam start
```

```
    XFLK    (NPFLKA) = -9.1+(0.297*RGAUS1)+
      &           (WHASOU (1)*0.7)-(TXFLK (NPFLKA)*50.0)
    YFLK    (NPFLKA) = -6.7+(0.297*RGAUS2)+
      &           (WHASOU (2)*0.7)-(TYFLK (NPFLKA)*50.0)
    ZFLK    (NPFLKA) = ZBEAM
```

The FLUKA source.f file used to perform proton therapy covering a 5 cm × 5 cm × 5 cm TV at depth 6 cm to 11 cm centered inside a water phantom. The ENEDGE lists the 50 proton energies (in GeV) and, CUMPR the corresponding weights to form a SOBP. The proton positions are modified to cover a 5 cm×5 cm area in the lateral positions around the iso-centre.

```
      DIMENSION CUMPR(0:51), ENEDGE(52)
*these corresponds to 50 entries (Bragg peaks) in both CUMPR and ENEDGE
*   Proton energy group boundaries
      DATA ENEDGE /
     & 77.1182773886851E-03,
     & 78.0085858944591E-03,
     & 78.8915291193969E-03,
     & 79.7673079123845E-03,
     & 80.6361139727838E-03,
     & 81.4981304283696E-03,
     & 82.3535323669501E-03,
     & 83.2024873261408E-03,
     & 84.0451557452616E-03,
     & 84.8816913828841E-03,
     & 85.7122417031796E-03,
     & 86.5369482338763E-03,
     & 87.3559468983426E-03,
     & 88.1693683240534E-03,
     & 88.9773381294647E-03,
     & 89.7799771911226E-03,
     & 90.577401892649E-03,
     & 91.36972435709E-03,
     & 92.1570526639697E-03,
     & 92.9394910522649E-03,
     & 93.7171401104059E-03,
     & 94.4900969543033E-03,
     & 95.2584553943155E-03,
     & 96.0223060919857E-03,
     & 96.7817367073076E-03,
     & 97.5368320372116E-03,
     & 98.2876741459047E-03,
     & 99.0343424876438E-03,
     & 99.7769140224747E-03,
     & 100.515463325424E-03,
     & 101.250062689592E-03,
     & 101.98078222356E-03,
     & 102.70768994349E-03,
     & 103.430851860271E-03,
     & 104.150332062029E-03,
     & 104.866192792303E-03,
     & 105.578494524163E-03,
     & 106.287296030525E-03,
     & 106.992654450899E-03,
     & 107.694625354784E-03,
     & 108.393262801931E-03,
     & 109.088619399638E-03,
     & 109.780746357275E-03,
     & 110.469693538187E-03,
     & 111.155509509138E-03,
     & 111.838241587432E-03,
     & 112.517935885843E-03,
     & 113.194637355482E-03,
```

```
     & 113.868389826706E-03,
     & 114.539236048197E-03,
     & 115.207217724285E-03,
     & 115.872375550633E-03/

*   Cumulative spectrum
      DATA CUMPR / 0.D0,
*...+....1....+....2....+....3....+....4....+....5....+....6....+
     & 0.003761782646171,
     & 0.011357217110222,
     & 0.019051173490196,
     & 0.026847045044525,
     & 0.034748417919131,
     & 0.042759086624975,
     & 0.050883071136116,
     & 0.059124635819418,
     & 0.067488310440235,
     & 0.075978913527693,
     & 0.084601578430005,
     & 0.093361782446104,
     & 0.10226537948698,
     & 0.111318636800872,
     & 0.120528276394369,
     & 0.129901521900501,
     & 0.139446151790596,
     & 0.149170560005786,
     & 0.159083825305684,
     & 0.169195790907599,
     & 0.179517156335242,
     & 0.19005958383185,
     & 0.200835822246695,
     & 0.211859852013537,
     & 0.223147055756059,
     & 0.234714420249635,
     & 0.246580777040109,
     & 0.258767091109207,
     & 0.271296809784166,
     & 0.284196287909703,
     & 0.297495310566906,
     & 0.311227741987737,
     & 0.325432339773053,
     & 0.340153788634234,
     & 0.355444030131292,
     & 0.371363998344268,
     & 0.387985922934853,
     & 0.405396442498639,
     & 0.423700903771731,
     & 0.443029445886872,
     & 0.463545861089213,
     & 0.485460943860131,
     & 0.509053439075702,
     & 0.534704602057566,
     & 0.56295892381017,
     & 0.59463995355789,
     & 0.631097358471131,
     & 0.674827543687882,
     & 0.731514725871152,
     & 0.822172058996108,
     & 1/

* Particle coordinates
* cover the volume in X and Y direction
* Gaussian sigma 0.297(=0.7FWHM) to account for lateral spread of beam
      CALL FLNRR2(RGAUS1, RGAUS2)
      XFLK (NPFLKA) = (-2.7 + 0.297*RGAUS1)+ FLRNDM(DUMMY)*5.4
      YFLK (NPFLKA) = (-2.7 + 0.297*RGAUS2)+ FLRNDM(DUMMY)*5.4
      ZFLK (NPFLKA) = ZBEAM
```

B. FLUKA HADGT20M and SI1MEVNE fluence

HADGT20M

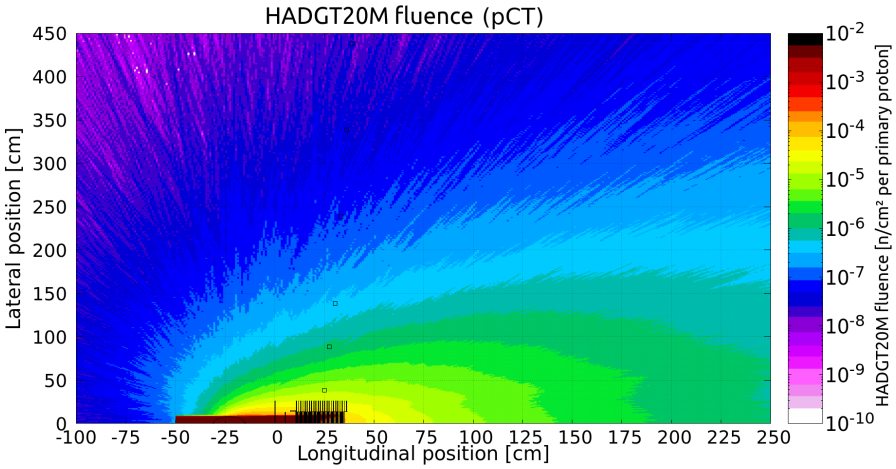

(a) The HADGT20M fluence per primary proton in proton CT. The primary protons pass through the cylindrical water phantom and come to a full stop inside the DTC.

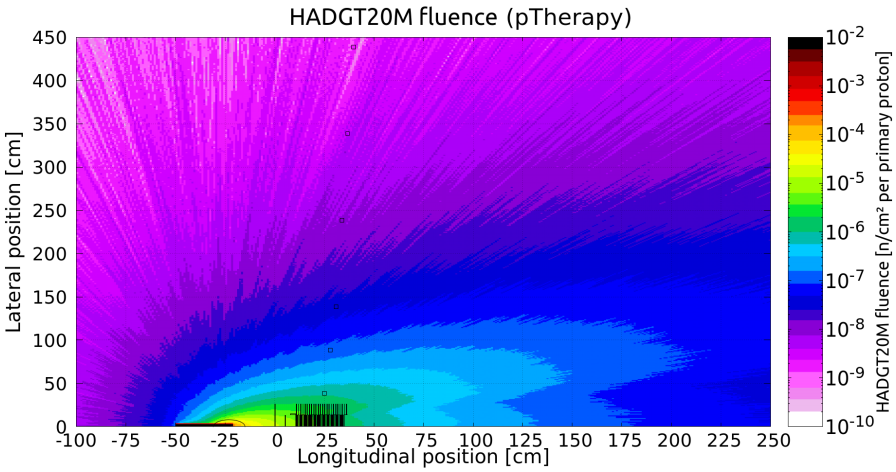

(b) The HADGT20M fluence per primary proton in proton Therapy. The primary protons come to a full stop inside the cylindrical water phantom.

Figure B.1: Overview of the HADGT20M fluence in pCT (a) and proton therapy (b) surrounding the DTC and potential lateral placements of FPGA and readout systems. The colour scheme and range is identical in both (a) and (b) to identify the difference in amount of HADGT20M between proton CT and proton therapy. The six square black outlines the FPGA placements.

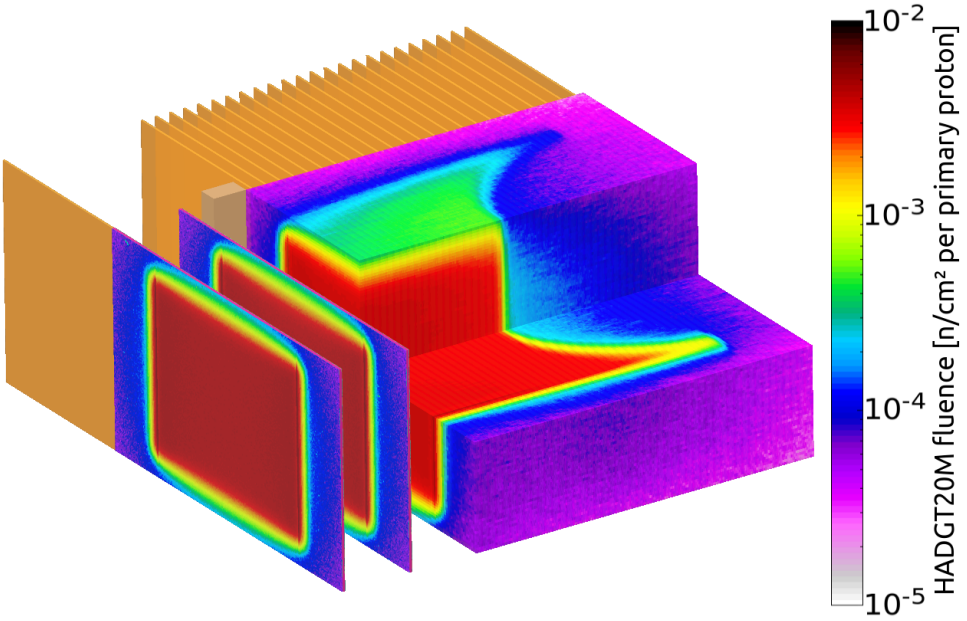

(a) HADGT20M fluence inside the DTC during proton CT. Most HADGT20M come to a full stop inside the DTC.

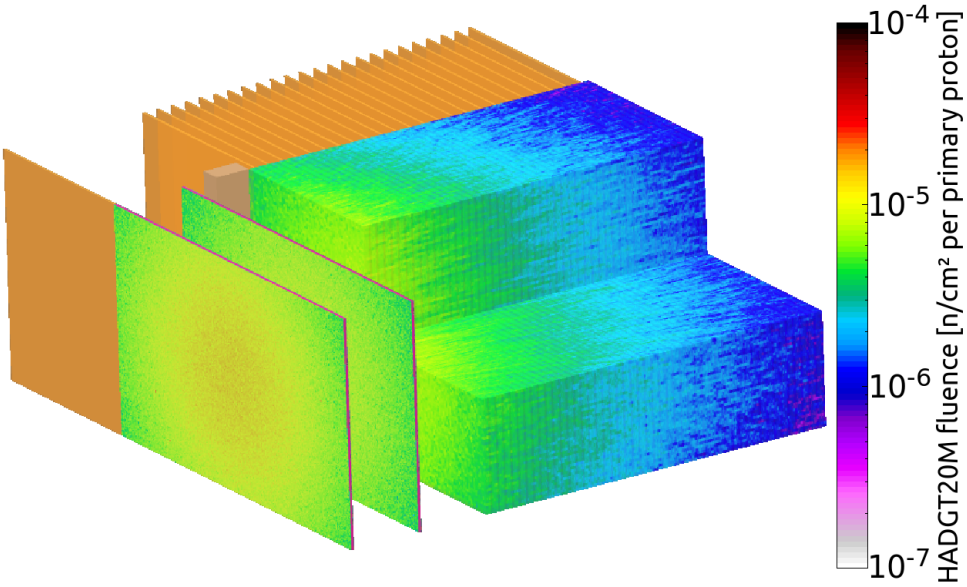

(b) HADGT20M fluence inside the DTC during proton therapy.

Figure B.2: Three dimensional representation of the DTC with the top right quadrant removed and overlaid with HADGT20M fluence per primary proton. Note the difference in fluence magnitude between pCT (a) and pTherapy (b).

SI1MEVNE

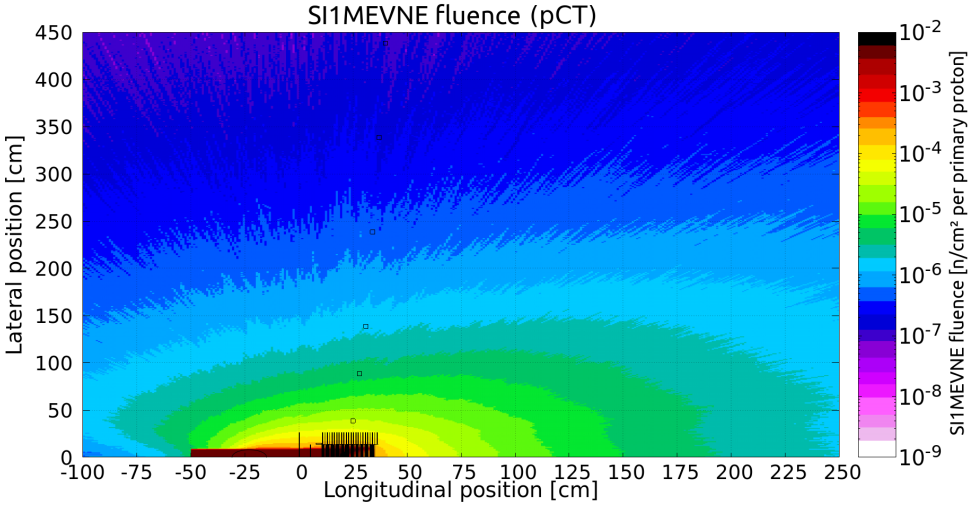

(a) The SI1MEVNE fluence per primary proton in proton CT. The primary protons pass through the cylindrical water phantom and come to a stop inside the DTC.

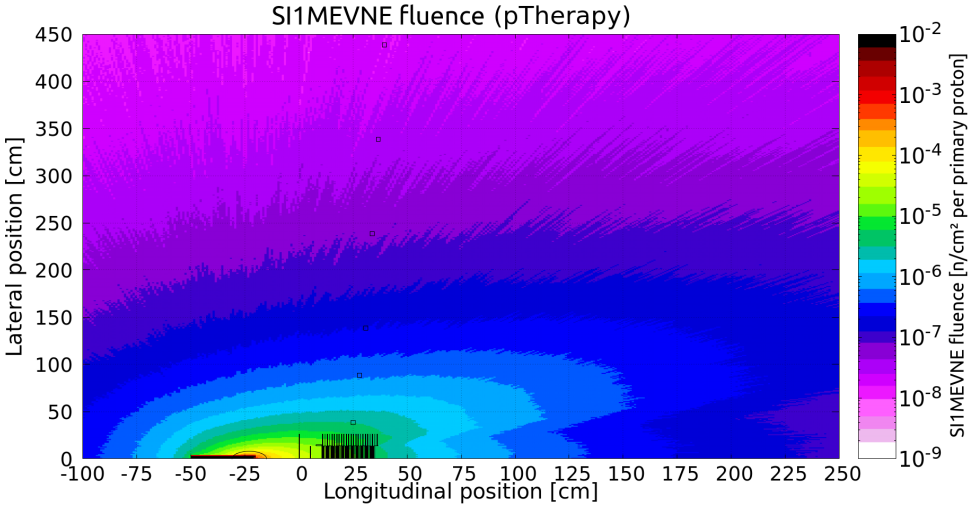

(b) The SI1MEVNE fluence per primary proton in proton Therapy. The primary protons come to a full stop inside the cylindrical water phantom.

Figure B.3: Overview of the SI1MEVNE fluence in pCT (a) and proton therapy (b) surrounding the DTC and potential lateral placements of FPGA and readout systems. The colour scheme and range is identical in both (a) and (b) to identify the difference in amount of SI1MEVNE between proton CT and proton therapy. The six square black outlines the FPGA placements.

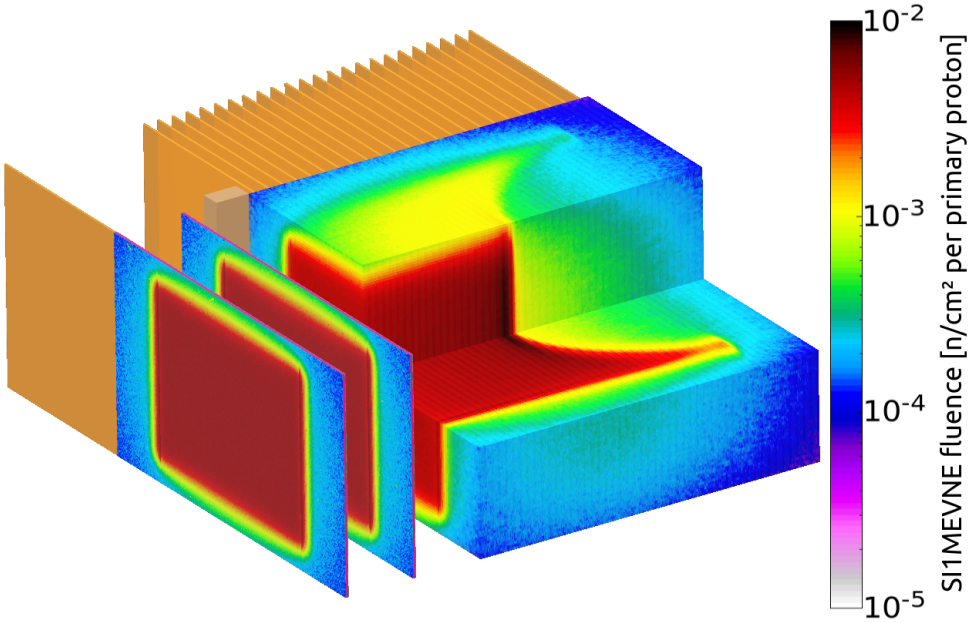

(a) SI1MEVNE fluence inside the DTC during proton CT. An increased fluence of SI1MEVNE particles is observed around the range of protons.

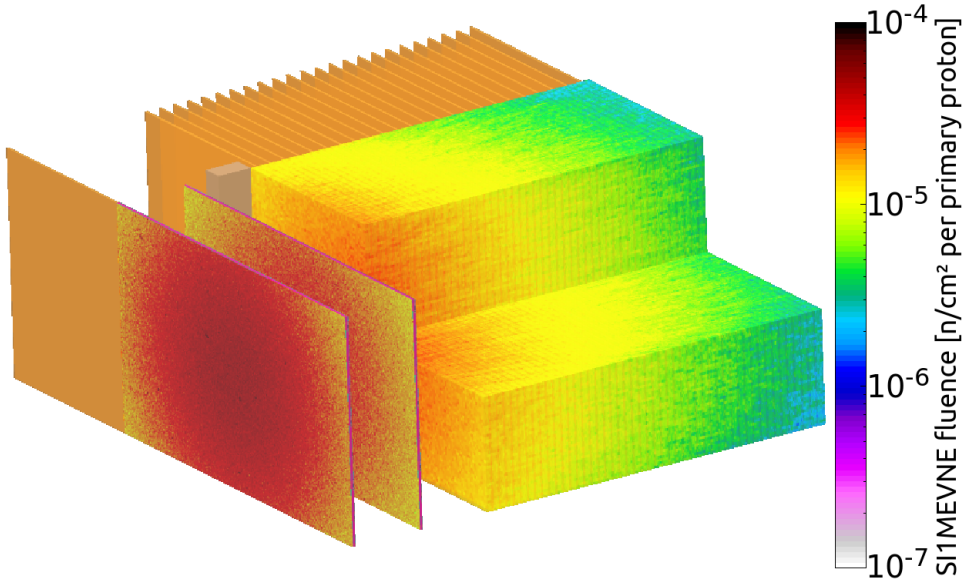

(b) SI1MEVNE fluence inside the DTC during proton therapy. The first tracker experience the largest amount of SI1MEVNE.

Figure B.4: Three dimensional representation of the DTC with the top right quadrant removed and overlaid with SI1MEVNE fluence per primary proton. Note the difference in fluence magnitude between pCT (a) and proton therapy (b).

C. Most likely path and proton radiography reconstruction

A relatively shortened code snippet detailing the MLP implementation from Krah et al. [56] in the single-sided setup and the subsequent pRad reconstruction from Collins-Fekete et al. [71] is presented here. The full code written to prepare and use the proton data obtained from the GATE MC simulations for MLP estimations and image reconstruction is available at GitHub:
`https://github.com/JarleSoelie/pRad` for full pRad reconstruction, and
`https://github.com/JarleSoelie/pCT` for preparing the MC data for pCT reconstruction.

Single-sided Most Likely Path and pRad implementation

```
//Proton positions from trackers/hull
TVector3 m0(Point->x12,Point->y12,Point->z12);
TVector3 p0(Point->p1x, Point->p1y, Point->p1z);

TVector3 m1(Point->x21, Point->y21, Point->z21);
TVector3 p1(Point->p2x, Point->p2y, Point->p2z);

//Initialization of the MLP
float X_mlp,Z_mlp, theta_X_mlp,theta_Z_mlp, X_mlp_sigma,Z_mlp_sigma;
TVector3 p;
TVector3 p_old = m0;

//Iterator for the matrix operations (needed later)
int a;
//Matrices
double T_beam[4];
  T_beam[0] = 1;
  T_beam[1] = 0;
  T_beam[2] = 1/d_source;
  T_beam[3] = 1;
double T_beam_transpose[4];
  T_beam_transpose[0] = 1;
  T_beam_transpose[1] = 1/d_source;
  T_beam_transpose[2] = 0;
  T_beam_transpose[3] = 1;

double T_out[4];
  T_out[0] = 1; //Eq. 26 in Krah
  T_out[1] = 0;
  T_out[2] = -1/(d_T);
  T_out[3] = 1/(d_T);
double T_out_transpose[4];
  T_out_transpose[0] = T_out[0];
  T_out_transpose[1] = T_out[2];
  T_out_transpose[2] = T_out[1];
  T_out_transpose[3] = T_out[3];

```

```
38 double beam_uncert[4]; //sigma spot-size
39   beam_uncert[0] = s_pos*s_pos;
40   beam_uncert[1] = 0;
41   beam_uncert[2] = 0;
42   beam_uncert[3] = 0;
43 double beam_1[4]; //T_beam*beam_uncert1
44   beam_1[0] = ((T_beam[0]*beam_uncert[0])+(T_beam[1]*beam_uncert[2]));
45   beam_1[1] = ((T_beam[0]*beam_uncert[1])+(T_beam[1]*beam_uncert[3]));
46   beam_1[2] = ((T_beam[2]*beam_uncert[0])+(T_beam[3]*beam_uncert[2]));
47   beam_1[3] = ((T_beam[2]*beam_uncert[1])+(T_beam[3]*beam_uncert[3]));
48
49 double Sigma_in[4]={0}; //Eq.29 in Krah
50   Sigma_in[0] = ((beam_1[0]*T_beam_transpose[0])+(beam_1[1]*
       T_beam_transpose[2]));
51   Sigma_in[1] = ((beam_1[0]*T_beam_transpose[1])+(beam_1[1]*
       T_beam_transpose[3]));
52   Sigma_in[2] = ((beam_1[2]*T_beam_transpose[0])+(beam_1[3]*
       T_beam_transpose[2]));
53   Sigma_in[3] = (((beam_1[2]*T_beam_transpose[1])+(beam_1[3]*
       T_beam_transpose[3])))+pow(s_angle, 2);
54
55 double Sigma_out[4];
56   Sigma_out[0] = pow(s_pos_out,2)*((T_out[0]*T_out_transpose[0])+(T_out
       [1]*T_out_transpose[2]));
57   Sigma_out[1] = pow(s_pos_out,2)*((T_out[0]*T_out_transpose[1])+(T_out
       [1]*T_out_transpose[3]));
58   Sigma_out[2] = pow(s_pos_out,2)*((T_out[2]*T_out_transpose[0])+(T_out
       [3]*T_out_transpose[2]));
59   Sigma_out[3] = (pow(s_pos_out,2)*((T_out[2]*T_out_transpose[1])+(T_out
       [3]*T_out_transpose[3])))+pow(Point->scatter_out,2);
60
61 double S_in[4]; /Eq. 14 in Krah
62   S_in[0] = 1;
63   S_in[1] = d_entry;
64   S_in[2] = 0;
65   S_in[3] = 1;
66 double S_in_transpose[4];
67   S_in_transpose[0] = S_in[0];
68   S_in_transpose[1] = S_in[2];
69   S_in_transpose[2] = S_in[1];
70   S_in_transpose[3] = S_in[3];
71
72 double S_out_inverse[4]; //inverse of a two by two matrix ((a b),(c d)):
       1/determinant ((d,-b),(-c,a))
73   S_out_inverse[0] = 1;
74   S_out_inverse[1] = -d_exit;
75   S_out_inverse[2] = 0;
76   S_out_inverse[3] = 1;
77 double S_out_inverse_transpose[4];
78   S_out_inverse_transpose[0] = 1;
79   S_out_inverse_transpose[1] = 0;
80   S_out_inverse_transpose[2] = -d_exit;
81   S_out_inverse_transpose[3] = 1;
82
83   //Can calculate parts of the C1 and C2 terms for later use
84 double SS_in[4]; //S_in*Sigma_in
85   SS_in[0] = (S_in[0]*Sigma_in[0])+(S_in[1]*Sigma_in[2]);
86   SS_in[1] = (S_in[0]*Sigma_in[1])+(S_in[1]*Sigma_in[3]);
87   SS_in[2] = (S_in[2]*Sigma_in[0])+(S_in[3]*Sigma_in[2]);
88   SS_in[3] = (S_in[2]*Sigma_in[1])+(S_in[3]*Sigma_in[3]);
89 double SSS_in[4]; //S_in*Sigma_in*S_in_transpose (to be multiplied with
       R_0 and R_0_transpose later)
90   SSS_in[0] = (SS_in[0]*S_in_transpose[0])+(SS_in[1]*S_in_transpose[2]);
91   SSS_in[1] = (SS_in[0]*S_in_transpose[1])+(SS_in[1]*S_in_transpose[3]);
92   SSS_in[2] = (SS_in[2]*S_in_transpose[0])+(SS_in[3]*S_in_transpose[2]);
93   SSS_in[3] = (SS_in[2]*S_in_transpose[1])+(SS_in[3]*S_in_transpose[3]);
94
95 double SS_out[4]; //S_out_inverse*Sigma_out
96   SS_out[0] = (S_out_inverse[0]*Sigma_out[0])+(S_out_inverse[1]*Sigma_out
```

```
    [2]);
  SS_out[1] = (S_out_inverse[0]*Sigma_out[1])+(S_out_inverse[1]*Sigma_out
    [3]);
  SS_out[2] = (S_out_inverse[2]*Sigma_out[0])+(S_out_inverse[3]*Sigma_out
    [2]);
  SS_out[3] = (S_out_inverse[2]*Sigma_out[1])+(S_out_inverse[3]*Sigma_out
    [3]);
double SSS_out[4]; //S_out_inverse*Sigma_out*S_out_inverse_transpose (to
    be multiplied with R_1_inverse and R_1_inverse_transpose later)
  SSS_out[0] = (SS_out[0]*S_out_inverse_transpose[0])+(SS_out[1]*
    S_out_inverse_transpose[2]);
  SSS_out[1] = (SS_out[0]*S_out_inverse_transpose[1])+(SS_out[1]*
    S_out_inverse_transpose[3]);
  SSS_out[2] = (SS_out[2]*S_out_inverse_transpose[0])+(SS_out[3]*
    S_out_inverse_transpose[2]);
  SSS_out[3] = (SS_out[2]*S_out_inverse_transpose[1])+(SS_out[3]*
    S_out_inverse_transpose[3]);

double R_0[4]={0};
double R_0_transpose[4]={0};
double RSSS_0[4]={0};
double RS_0[4]={0};
double R_1_inverse[4]={0};
double R_1_inverse_transpose[4]={0};
double RSSS_1[4]={0};
double RS_1[4]={0};
double RS_2[4]={0};

double Sigma_1[4]={0};
double Sigma_2[4]={0};

double y_0[2]={0};
double y_2[2]={0};

double C1_1[4]={0};
double C1[4]={0};

double C2_1[4]={0};
double C2_2[4]={0};
double C2[4]={0};

double C12[4]={0};
double C12_inverse[4]={0};

double first_first[4]={0};
double second_first[4]={0};
double first_second[2]={0};
double second_second[2]={0};
double first[2] = {0};
double second[2]={0};

//Initialize the image reconstruction variables
std::map<pair<int,int>,double> Lengthmap; // Image grid that will contain
    all path information (length spent in each image column)
std::pair<std::map<std::pair<int,int>,double>::iterator,bool> ret;
int binx,biny,binz;
double TotL = 0;

//Parameter initialization
double sy1, sy2, st1, st2, sty1, sty2;
double determinant_1, determinant_2, determinant_C12;

//Initialize the MLP iterators
double step_length = (m1.y()-m0.y())/Nsteps;
double posy=m0.y()+step_length; //skip the first track value since not
    defined here
//int k=1;

// Step through until reach the exit depth
```

```
while(posy<m1.y()){  //y is in beam direction

  //Transvection matrices, eq.8 in Krah
  R_0[0] = 1;
  R_0[1] = posy-m0.y();
  R_0[2] = 0;
  R_0[3] = 1;
  R_0_transpose[0] = 1;
  R_0_transpose[1] = 0;
  R_0_transpose[2] = posy-m0.y();
  R_0_transpose[3] = 1;

  R_1_inverse[0] = 1;
  R_1_inverse[1] = -(m1.y()-posy);
  R_1_inverse[2] = 0;
  R_1_inverse[3] = 1;
  R_1_inverse_transpose[0] = 1;
  R_1_inverse_transpose[1] = 0;
  R_1_inverse_transpose[2] = -(m1.y()-posy);
  R_1_inverse_transpose[3] = 1;

  //need these for later:R_0*S_in, R_0*SSS_in, and R_1_inverse*SSS_out
  RS_0[0] = (R_0[0]*S_in[0]) + (R_0[1]*S_in[2]);
  RS_0[1] = (R_0[0]*S_in[1]) + (R_0[1]*S_in[3]);
  RS_0[2] = (R_0[2]*S_in[0]) + (R_0[3]*S_in[2]);
  RS_0[3] = (R_0[2]*S_in[1]) + (R_0[3]*S_in[3]);

  RSSS_0[0]= (R_0[0]*SSS_in[0]) + (R_0[1]*SSS_in[2]);
  RSSS_0[1]= (R_0[0]*SSS_in[1]) + (R_0[1]*SSS_in[3]);
  RSSS_0[2]= (R_0[2]*SSS_in[0]) + (R_0[3]*SSS_in[2]);
  RSSS_0[3]= (R_0[2]*SSS_in[1]) + (R_0[3]*SSS_in[3]);

  RS_1[0]= (R_1_inverse[0]*S_out_inverse[0])+(R_1_inverse[1]*S_out_inverse
    [2]);
  RS_1[1]= (R_1_inverse[0]*S_out_inverse[1])+(R_1_inverse[1]*S_out_inverse
    [3]);
  RS_1[2]= (R_1_inverse[2]*S_out_inverse[0])+(R_1_inverse[3]*S_out_inverse
    [2]);
  RS_1[3]= (R_1_inverse[2]*S_out_inverse[1])+(R_1_inverse[3]*S_out_inverse
    [3]);

  RSSS_1[0]= (R_1_inverse[0]*SSS_out[0])+(R_1_inverse[1]*SSS_out[2]);
  RSSS_1[1]= (R_1_inverse[0]*SSS_out[1])+(R_1_inverse[1]*SSS_out[3]);
  RSSS_1[2]= (R_1_inverse[2]*SSS_out[0])+(R_1_inverse[3]*SSS_out[2]);
  RSSS_1[3]= (R_1_inverse[2]*SSS_out[1])+(R_1_inverse[3]*SSS_out[3]);

  // First do everything not depending on the direction of interest (
    either X_mlp or Z_mlp)
  //scattering sigma matrices
  sy1 = Sigmay1(posy-m0.y());
  st1 = Sigmat1(posy-m0.y());
  sty1 = Sigmaty1(posy-m0.y());

  sy2 = Sigmay2(m1.y()-m0.y(),posy-m0.y());
  sty2 = Sigmaty2(m1.y()-m0.y(),posy-m0.y());
  st2 = Sigmat2(m1.y()-m0.y(),posy-m0.y());

  // Scattering sigma matrices
  Sigma_1[0] = sy1;
  Sigma_1[1] = sty1;
  Sigma_1[2] = sty1;
  Sigma_1[3] = st1;

  Sigma_2[0] = sy2;
  Sigma_2[1] = sty2;
  Sigma_2[2] = sty2;
  Sigma_2[3] = st2;

  // Calculate the pre factors C1 and C2 as in Krah et al. (2018): C2*(C1+
```

```
  C2)^-1 R0*S0*Y0 + C1*(C1+C2)^1 R1^-1*S1^-1*Y2
// First start with the C1 = ((R_0*S_in*Sigma_in*S_in_transpose)*(
  R_0_transpose))+Sigma_1
C1_1[0]=(RSSS_0[0]*R_0_transpose[0])+(RSSS_0[1]*R_0_transpose[2]);
C1_1[1]=(RSSS_0[0]*R_0_transpose[1])+(RSSS_0[1]*R_0_transpose[3]);
C1_1[2]=(RSSS_0[2]*R_0_transpose[0])+(RSSS_0[3]*R_0_transpose[2]);
C1_1[3]=(RSSS_0[2]*R_0_transpose[1])+(RSSS_0[3]*R_0_transpose[3]);

for (a=0;a<4;a++){
  C1[a] = C1_1[a]+Sigma_1[a];
}

//Now calculate C2 = (R_1_inverse*S_out_inverse*Sigma_out*
  S_out_inverse_transpose*R_1_inverse_transpose) + (R_1_inverse*Sigma_2*
  R_1_inverse_transpose)
C2_1[0] = (RSSS_1[0]*R_1_inverse_transpose[0])+(RSSS_1[1]*
  R_1_inverse_transpose[2]);
C2_1[1] = (RSSS_1[0]*R_1_inverse_transpose[1])+(RSSS_1[1]*
  R_1_inverse_transpose[3]);
C2_1[2] = (RSSS_1[2]*R_1_inverse_transpose[0])+(RSSS_1[3]*
  R_1_inverse_transpose[2]);
C2_1[3] = (RSSS_1[2]*R_1_inverse_transpose[1])+(RSSS_1[3]*
  R_1_inverse_transpose[3]);

RS_2[0] = (R_1_inverse[0]*Sigma_2[0])+(R_1_inverse[1]*Sigma_2[2]);
RS_2[1] = (R_1_inverse[0]*Sigma_2[1])+(R_1_inverse[1]*Sigma_2[3]);
RS_2[2] = (R_1_inverse[2]*Sigma_2[0])+(R_1_inverse[3]*Sigma_2[2]);
RS_2[3] = (R_1_inverse[2]*Sigma_2[1])+(R_1_inverse[3]*Sigma_2[3]);

C2_2[0] = (RS_2[0]*R_1_inverse_transpose[0])+(RS_2[1]*
  R_1_inverse_transpose[2]);
C2_2[1] = (RS_2[0]*R_1_inverse_transpose[1])+(RS_2[1]*
  R_1_inverse_transpose[3]);
C2_2[2] = (RS_2[2]*R_1_inverse_transpose[0])+(RS_2[3]*
  R_1_inverse_transpose[2]);
C2_2[3] = (RS_2[2]*R_1_inverse_transpose[1])+(RS_2[3]*
  R_1_inverse_transpose[3]);

C2[0] = C2_1[0]+C2_2[0];
C2[1] = C2_1[1]+C2_2[1];
C2[2] = C2_1[2]+C2_2[2];
C2[3] = C2_1[3]+C2_2[3];

//Add the second factor to the first to yield C1+C2
for(a=0;a<4;a++){
  C12[a]=C1[a]+C2[a];
}

//invert so to get the prefactor (C1+C2)^-1
determinant_C12=(C12[0]*C12[3])-(C12[1]*C12[2]);
C12_inverse[0]=C12[3]/determinant_C12;
C12_inverse[1]=-C12[1]/determinant_C12;
C12_inverse[2]=-C12[2]/determinant_C12;
C12_inverse[3]=C12[0]/determinant_C12;

//Multiply C2 to yield the first prefactor C2*(C1+C2)^-1
first_first[0]=(C2[0]*C12_inverse[0])+(C2[1]*C12_inverse[2]);
first_first[1]=(C2[0]*C12_inverse[1])+(C2[1]*C12_inverse[3]);
first_first[2]=(C2[2]*C12_inverse[0])+(C2[3]*C12_inverse[2]);
first_first[3]=(C2[2]*C12_inverse[1])+(C2[3]*C12_inverse[3]);

//Same with C1 to yield the second prefactor C1*(C1+C2)^-1
second_first[0]=(C1[0]*C12_inverse[0])+(C1[1]*C12_inverse[2]);
second_first[1]=(C1[0]*C12_inverse[1])+(C1[1]*C12_inverse[3]);
second_first[2]=(C1[2]*C12_inverse[0])+(C1[3]*C12_inverse[2]);
second_first[3]=(C1[2]*C12_inverse[1])+(C1[3]*C12_inverse[3]);

//Now the second part of each factor (start with X drection)
y_0[0] = m0.x();
```

```
276   y_0[1] = tan(p0.x());
277
278   y_2[0] = m1.x();
279   y_2[1] = tan(p1.x());
280
281   // Start with R_0*S_in*Y0
282   first_second[0] = (RS_0[0]*y_0[0])+(RS_0[1]*y_0[1]);
283   first_second[1] = (RS_0[2]*y_0[0])+(RS_0[3]*y_0[1]);
284
285   // Now R1_inverse*S_out_inverse*Y2
286   second_second[0]=(RS_1[0]*y_2[0])+(RS_1[1]*y_2[1]);
287   second_second[1]=(RS_1[2]*y_2[0])+(RS_1[3]*y_2[1]);
288
289   //Put Everything together: (C2*(C1+C2)^-1)*(R_0*S_in*Y0)
290   first[0]=(first_first[0]*first_second[0])+(first_first[1]*first_second
        [1]);
291   first[1]=(first_first[2]*first_second[0])+(first_first[3]*first_second
        [1]);
292   //+(C1*(C1+C2)^-1)*(R_1_inverse*S_out_inverse*Y2)
293   second[0]=(second_first[0]*second_second[0])+(second_first[1]*
        second_second[1]);
294   second[1]=(second_first[2]*second_second[0])+(second_first[3]*
        second_second[1]);
295
296   X_mlp=(first[0]+second[0]); //=C2*(C1+C2)^-1 R0*S0*Y0+C1*(C1+C2)^1 R1
        ^-1*S1^-1*Y2
297   theta_X_mlp=(first[1]+second[1]);
298   X_mlp_sigma = second_first[2]*C2[1]+second_first[3]*C2[3];
299
300   //Now do the other direction
301   y_0[0] = m0.z();
302   y_0[1] = tan(p0.z());
303
304   y_2[0] = m1.z();
305   y_2[1] = tan(p1.z());
306
307   //Again with respect to the other direction
308   first_second[0] = (RS_0[0]*y_0[0])+(RS_0[1]*y_0[1]);
309   first_second[1] = (RS_0[2]*y_0[0])+(RS_0[3]*y_0[1]);
310
311   second_second[0]=(RS_1[0]*y_2[0])+(RS_1[1]*y_2[1]);
312   second_second[1]=(RS_1[2]*y_2[0])+(RS_1[3]*y_2[1]);
313
314   //Put Everything together again
315   first[0]=(first_first[0]*first_second[0])+(first_first[1]*first_second
        [1]);
316   first[1]=(first_first[2]*first_second[0])+(first_first[3]*first_second
        [1]);
317
318   second[0]=(second_first[0]*second_second[0])+(second_first[1]*
        second_second[1]);
319   second[1]=(second_first[2]*second_second[0])+(second_first[3]*
        second_second[1]);
320
321   Z_mlp=(first[0]+second[0]);
322   theta_Z_mlp=(first[1]+second[1]);
323   Z_mlp_sigma = second_first[2] * C2[1] + second_first[3] * C2[3];
324
325   p = TVector3(X_mlp, posy, Z_mlp);
326
327   //find the image bin we are in in the two traverse directions z and x
328   binx = project2D->GetXaxis()->FindBin(p.x()*10.0);
329   binz = project2D->GetYaxis()->FindBin(p.z()*10.0);
330
331   double L = TVector3(p-p_old).Mag(); // This is the length (magnitude) of
        the proton path inside the step  (/10 -> mm-cm  conversion)
332   pair<int,int> bin2dID = pair<int,int>(binx,binz); //find the key to the
        bin positions the proton is in (bin2dID)
333
```

```
334   ret = Lengthmap.insert(pair<pair<int,int>,double>(bin2dID,L)); //checks
        using insert whether the bin2dID key (column) has changed (proton has
        crossed it) and only connects L to the bin pos if it has
335   if ( ret.second==false ) Lengthmap[bin2dID] += L; //if (false=bin2dID is
        the same), column corresponding to bin2dID has not been crossed by the
        proton investigated, L is added to the length traversed so far
336
337   TotL+=L; //total length, sum up
338   p_old = p;
339   posy+=step_length;
340 }
341
342 std::map<std::pair<int,int>,double>::iterator it;
343
344 //Reconstruct the pRad
345 for(it = Lengthmap.begin(); it != Lengthmap.end(); it++) { //Goes through
      the Lengthmap
346   int BinX = it->first.first;
347   int BinZ = it->first.second;
348   double L = it->second;
349   double x = project2D->GetXaxis()->GetBinCenter(BinX);
350   double z = project2D->GetYaxis()->GetBinCenter(BinZ);
351   project2D->Fill(x,z,Point->weplReal, pow((L/TotL),2));
352 }
```

D. Reconstructed proton radiographs of paediatric head phantom

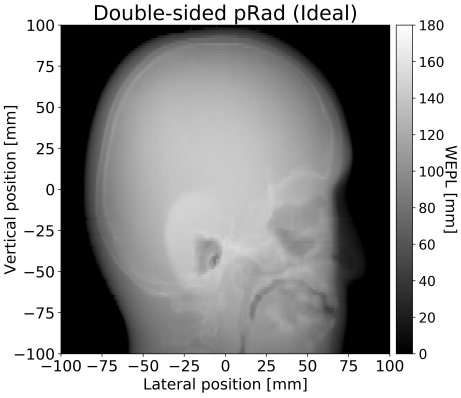

(a) Ideal double-sided pRad.

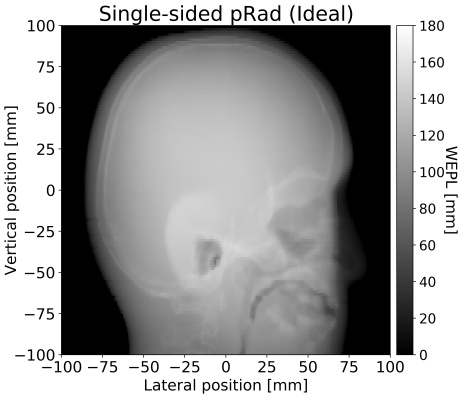

(b) Ideal single-sided pRad (7 mm FWHM pencil beam).

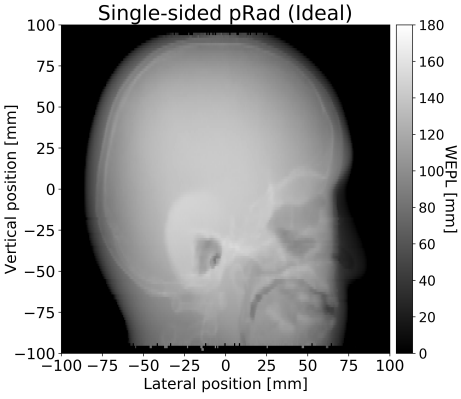

(c) Ideal single-sided pRad (3 mm FWHM pencil beam).

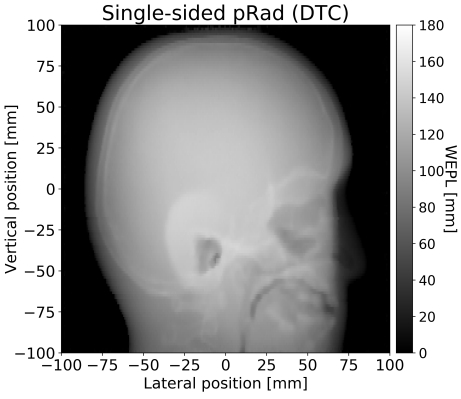

(d) Bergen DTC single-sided pRad (7 mm FWHM).

Figure D.1: Reconstructed pRad using the maximum likelihood image reconstruction method developed by Collins-Fekete et al. [71] on the data obtained from the MC framework as described in chapter 3.

E. Profiles of reconstructed proton CT of paediatric head phantom

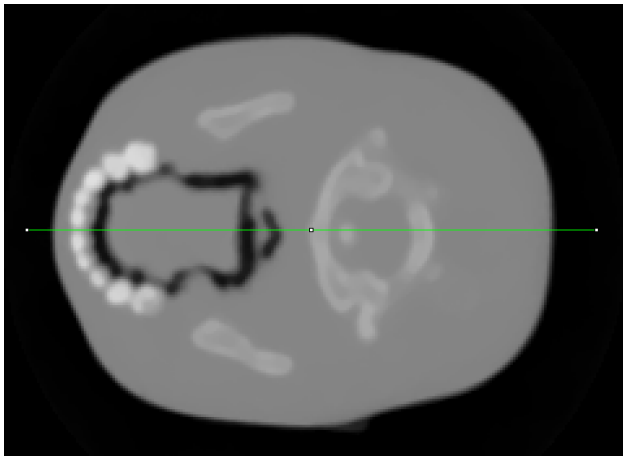

(a) Slice from the single-sided Bergen DTC pCT of the paediatric head phantom. A profile (focused on mouth structures) along the green line is taken in all three reconstructed images.

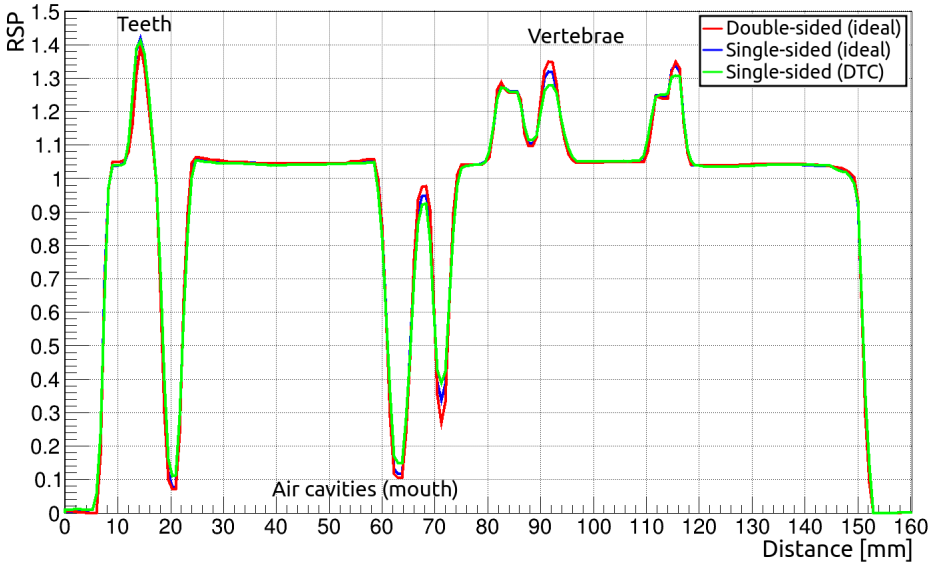

(b) Marked profile from the pCT reconstructions of the head phantom from the three investigated imaging systems (focused on mouth structures).

Figure E.1

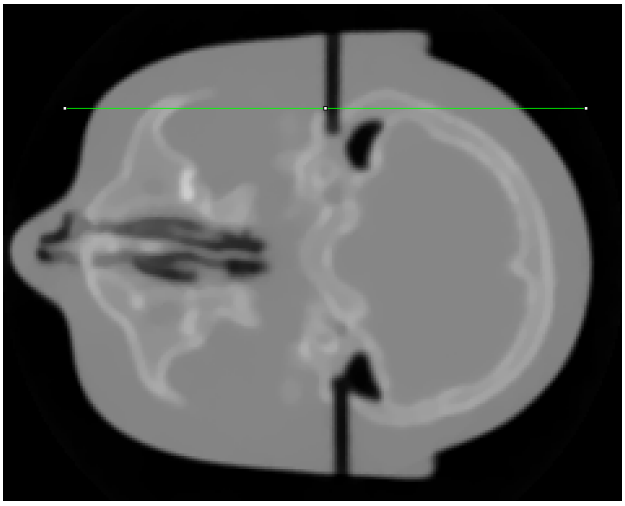

(a) Slice from the single-sided Bergen DTC pCT of the paediatric head phantom. A profile (focused on ear structures) along the green line is taken in all three images.

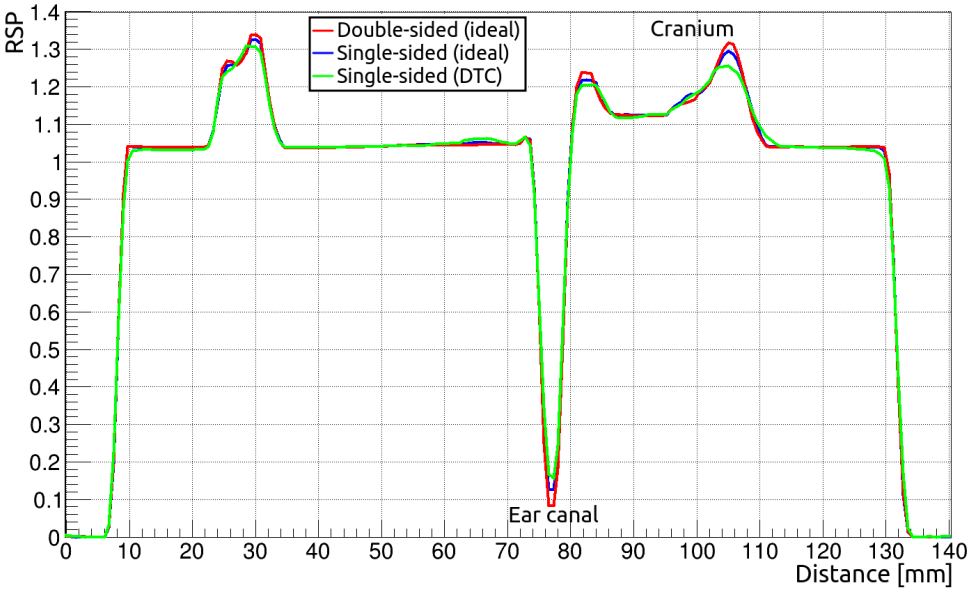

(b) Marked profile from the pCT reconstructions of the head phantom from the three investigated imaging systems (focused on ear structures).

Figure E.2

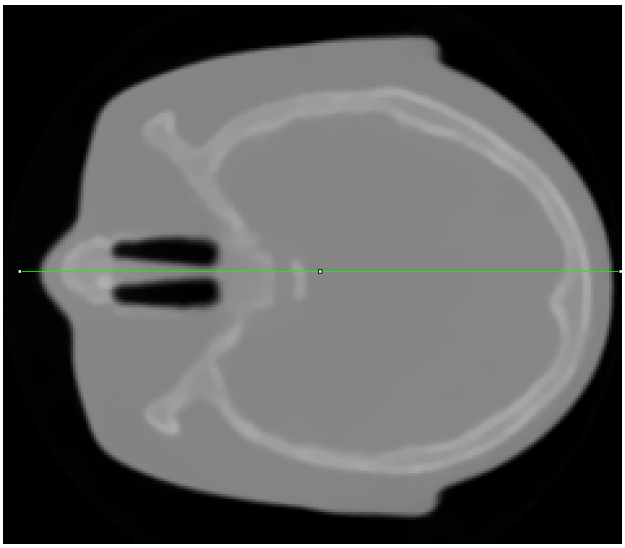

(a) Slice from the single-sided Bergen DTC pCT of the paediatric head phantom. A profile (focused on brain structures) along the green line is taken in all three images.

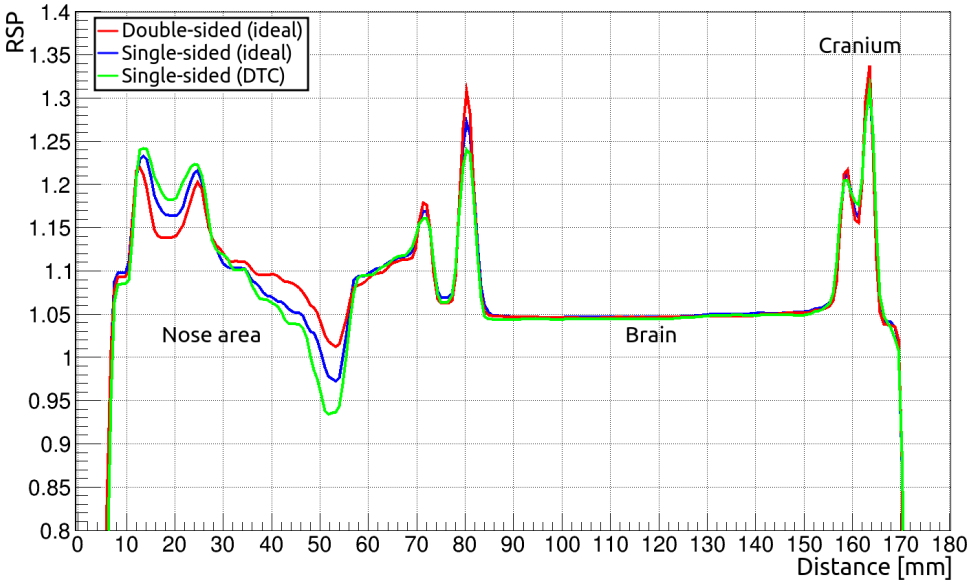

(b) Marked profile from the pCT reconstructions of the head phantom from the three investigated imaging systems (focused on nose and brain structures).

Figure E.3

Graphic design: Communication Division, UiB / Print: Skipnes Kommunikasjon AS

uib.no

ISBN: 9788230845028 (print)
9788230847701 (PDF)